MAX PLANCK INSTITUTE
für molekulare Physiologie

UNIVERSITY OF CRETE
Department of Biology

Master Thesis

Single particle analysis of the peroxisomal protein importing machinery

---

Submitted by

Dimitrios Vismpas

In fulfilment of the requirements for the degree of

Master of Science in Protein Biotechnology

University of Crete

Department of Biology

Prepared at the

Max Planck Institute of Molecular Physiology Dortmund

Department of Structural Biochemistry

October 2020

Reviewers

Supervisor:	Prof. Dr. Christos Gatsogiannis Max Planck Institute for Molecular Physiology, Dortmund Department of Structural Biochemistry
First reviewer:	Prof. Dr. Michael Kokkinidis University of Crete – IMBB FORTH Department of Biology – Crystallography, Heraklion
Second reviewer:	Prof. Dr. Kyriakos Petratos University of Crete – IMBB FORTH Department of Biology – Crystallography, Heraklion
Third reviewer:	Prof. Dr. Irene Athanasaki University of Crete Department of Biology – Immunobiology, Heraklion

Acknowledgements

First, I would like to thank Prof. Dr. Christos Gatsogiannis for offering me the opportunity to fulfill my Master Thesis in his group and specifically for giving me the possibility of working on such an interesting project.

Further on, I would like to thank Prof. Dr. Michael Kokkinidis for allowing my transfer to the MPI of Molecular Physiology.

Special thanks to my supervisor Pascal Lill for his constant support, help and advice regarding my work and career.

Consequently, I would like to thank the whole group of Prof. Dr. Stephan Raunser for their everyday help and advice. Additionally, I would like to thank Dr. Oliver Hofnagel and Dr. Daniel Prumbaum for training and constantly supporting me with the electron microscopes.

Thanks to Michelle and Lena for the nice moments in the lab. I really enjoyed my time working with you!

Finally, I would like to thank my family for giving me a chance to study and for supporting my decision moving abroad. Also, I would like to thank my friends for always supporting me and specifically Alexandros Kanakis.

Abstract

Pex14p, Pex17p and Pex5p peroxins, are the key components of the protein import machinery of *Saccharomyces cerevisiae* from the cytosol to the peroxisomal lumen. It is suggested that these peroxins are sufficient for the assembly of a functional importomer complex. However, the importing mechanism still remains unclear. The field is lacking structural insights into higher order membrane assemblies and markedly, into the pore formation mechanism. In the framework of this thesis, the yeast (Pex14p, Pex14p/Pex17p) and human (PEX14) docking complex components were reconstituted into lipid nanodiscs and further optimized for electron microscopy (EM) analysis, in order to elucidate the Pex17p contribution to the docking complex and reveal differences between the yeast and human homologues. Additionally, reconstitution of the yeast docking complex Pex14p/Pex17p in liposomes and subsequent addition of Pex5p was performed in order to clarify the structure and topology of the importomer. Initially, negative stain EM comparative studies between the Pex14p/Pex17p complex and Pex14p in absence of Pex17p suggest that Pex17p provides stability to the docking complex. Following, the human homologue PEX14 was expressed, purified and successfully reconstituted into lipid nanodiscs. Characterization with negative stain EM was performed but extensive optimization of the vitrification conditions is required in order to proceed with cryo-EM studies and observe substantial differences between the two homologues. Finally, liposomes containing the yeast docking complex (Pex14p.Pex17p) were assembled successfully. However, negative stain analysis after addition of Pex5p did not reveal any structural changes on the liposome surface. A close to native environment analysis, using cryo-EM, will be required for a more detailed data acquisition. Overall, the results of this thesis, set the stage for future pore-formation *in vitro* studies, using cargo proteins.

Table of contents

Table of Figures

List of Tables

List of Abbreviations

°C	Temperature in Celsius
µm	Micrometer
2D	Two-dimensional
3D	Three-dimensional
Å	Angström
ATP	Adenosine triphosphate
CCD	Charge coupled device
cMSP	Circularized membrane scaffold protein
CryoTEM	Cryo transmission electron microscopy
CTD	C-terminal domain
CTF	Contrast transfer function
DDC	Direct detection camera
DDD	Direct detection device
DNA	Deoxyribonucleic acid
DTM	Docking/translocation module
DUB	De-ubiquitinase
E.coli	*Escherichia coli*
EDTA	Ethylenediaminetetraacetic acid
EM	Electron microscope
et al.	Et alia
FEG	Field emission gun
ISAC	Iterative stable alignment and clustering
JA	Jasmonate
kDa	Kilodalton
kV	Kilovolt
Lab_6	Lanthanum hexaborite
mA	Milliampere
mDa	Megadalton
mg	Milligram
min	Minutes

ml	Milliliter
mM	Millimolar
MPI	Max-Planck-Institute
MSP	Membrane scaffold protein
ND	Nanodisc
nm	Nanometer
nM	Nanomolar
NTD	N-terminal domain
pH	Power of hydrogen
PFP	Pore forming protein
POPC	1-palmitoyl-2-oleoyl-sn-glycero-3-phosphocholine
PTM	Post translational modification
PTS	Peroxisome targeting sequence
REM	Receptor export module
RT	Room temperature
s	Seconds
SEC	Size exclusion chromatography
SPA	Single particle analysis
TEM	Transmission electron microscopy
TPR	Tetratricopeptide repeats
Tris	Tris(hydroxylmethyl)aminomethane
Ub	Ubiquitination
UF	Uranyl-formate
VIPER	Validation of Individual Parameter Reproducibility

1.Introduction

1.1 Pore forming proteins (PFPs)

Pore forming proteins possess the ability to form channels through lipid membranes and are characterized by their capability to transform from a water-soluble molecule and spontaneously insert into a membrane (Fradin et al. 2009). The general function of PFPs requires attachment to the membrane, usually mediated by other membrane proteins, or even lipids serving as receptors (Ros and García-Sáez 2015). Moreover, oligomerization of the PFP usually involves a dramatic conformational change and exposure of hydrophobic surfaces for subsequent membrane insertion and pore formation. (Iacovache et al. 2010) (Fradin et al. 2009). The aforementioned exposure results in an amphipathic layer that incites spontaneous pore formation (Anderluh and Lakey 2008) (Parker and Feil 2005). Therefore, membrane penetration and channel formation with the purpose of allowing the passage of ions, proteins and additional components is achieved (Cosentino et al. 2016).

Proposed by Gouaux, PFPs are distinguished into two categories, which are divided regarding the structural conformation of the pore-forming transmembrane domain, namely α-helix-PFPs and β-barrel-PFPs (Gouaux 1997). The common feature of α-helix-PFPs is the presence of α-helices in order to perforate and pierce the lipid bilayer, resulting in pore formation. The pore forming domains of α-PFPs include a significant amount of hydrophobic residues, which forces these proteins to embrace an inside out configuration to 'bury' these residues, resulting in stabilization by intra-chain hydrogen bonds, in their core (α-helix hairpin) (Lesieur et al. 1997) (Cosentino et al. 2016). β-barrel-PFPs are considered to be soluble proteins due to their hydrophobic amino acid content. Therefore, the oligomerization is imperative for membrane insertion (Schulz 1996). After the oligomerization, each protein molecule contributes 1-2 β-sheets, assembling a barrel-like pore which is connected by hydrogen bonds formed between the β-strand residues (Cosentino et al. 2016).

Peroxisomes, described in section (**1.2**), are lacking nucleic acids, ribosomes, chaperons and therefore, these cell organelles have to import their matrix enzymes in the peroxisomal lumen in order to fulfill their cellular tasks. Therefore, it is suggested that a pore is formed at the peroxisomal membrane, whereas the import process is not yet well characterized (Walton et al. 1995). The PTS_1-receptor Pex5p is the main peroxisomal component which is considered to play a crucial part in the assembly of a transient pore (Erdmann and Schliebs 2005). Also this

scenario is corroborated by the fact that Pex5p is proven to bind to lipids and similarly to pore forming toxins, is capable to spontaneously insert into a membrane (Kerssen et al. 2006) (Gouveia et al. 2000) (Gouveia et al. 2003). This theory was supported by electrophysiological studies suggesting a transient and dynamic pore induced by the peroxins Pex14p and Pex5p, respectively (Meinecke et al. 2010).

1.2 Peroxisomes

1.2.1 Peroxisomal importing process

Peroxisomes are small, eukaryotic cell organelles with a size from 0.1 to 1 μm, first observed by Rhodin in 1954 (discovered in mice kidney cells with electron microscopy) (van den Bosch et al. 1992). Twelve years later, in 1966, Christian de Duve and Pierre Baudhuin biochemically characterized them for the first time in rat liver cells (De Duve and Baudhuin 1966). (Nobel Prize in Physiology or Medicine in 1974).

Peroxisomes contain up to fifty enzymes linking them to a plethora of biochemical pathways (Platta et al. 2016). These cell organelles are mainly known as key metabolic organelles, specializing in oxidative metabolic reactions (Kaur et al. 2009). Peroxisomes are involved in a multitude of vital processes. The most known and well characterized tasks, are the breakdown of fatty acids via α-, β-oxidation (Wanders et al. 2001) (Lodhi and Semenkovich 2014) as well as the detoxification of cells (Fransen et al. 2012). Moreover, oxidative metabolism of lipids, carbohydrates and amino acids takes place in these cell compartments (Gabaldón 2010) (Lodhi and Semenkovich 2014). The main part of the peroxisomal metabolism is the catalase-oxidative reaction. Catalase is gathering hydrogen peroxide (H_2O_2) from the cytosol into the peroxisomal lumen (Tel-or et al. 1986) where detoxification of O_2/N_2 species takes place (Fransen et al. 2012).

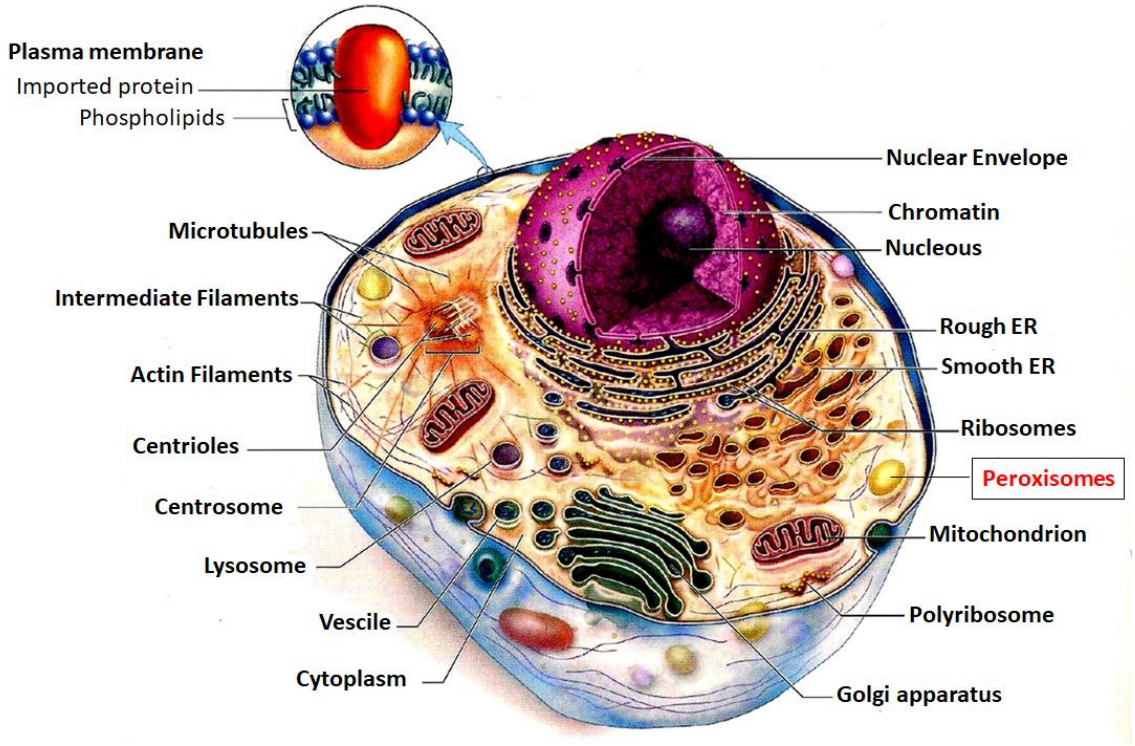

Figure (1): **Schematic illustration of the internal structure of a eukaryotic cell.**

Figure taken from 'Parts of a Cell - Arizona State University'.Chapter 3: Cell Structure and Function

http://4z7y.tk/chapter-3-cell-structure-and-function/

However, peroxisomes are also involved in other metabolic functions, such as Jasmonate (JA) biosynthesis (plant peroxisomes) (Corpas and Barroso 2018), photorespiration (plant peroxisomes) (Reumann and Weber 2006), indole-3-butyric acid (IBA) metabolism (plant peroxisomes) (Zolman et al. 2007) and sulfite oxidation (plant peroxisomes) (Hänsch and Mendel 2005). Peroxisomes are also responsible for the synthesis of signaling molecules, like reactive nitrogen species in plants and *C.elegans*. In mammals, the biosynthesis of steroid acid (bile acid) and plasmogens takes place in peroxisomes as well. In filamentous fungi the biosynthesis of penicillin and cephalosporin is taken over by these organelles (Platta et al. 2016).

The previous described tasks are taken over by peroxisomal matrix proteins, which are encoded by nuclear genes, synthesized on free-cytosolic ribosomes, folded and thereafter imported through the membrane (Walton et al. 1995) (El Magraoui et al. 2019) (Wang et al. 2019).

Peroxisomal protein transport is a selective procedure, that can be described as a 'recycling' multi-step mechanism, taking place between the cytosol and the peroxisomal lumen. Based on the type of targeting sequences, that are attached to the peroxisomal membrane proteins, import can be classified as PTS_1 or PTS_2 (Peroxisomal Targeting Sequences) (Gould et al. 1989) (Hoop et al. 1992). Moreover, an import independent from the aforementioned signaling is

suggested, referred to as PTS_3-import (Subramani 2002) (Klein et al. 2002). Adding to that, proteins not containing any of these targeting sequences, can be imported via 'piggy-back' by binding to a PTS_1 (Yang et al. 2001) (Islinger et al. 2009) or PTS_2-cotaining protein (Glover et al. 1994) (Effelsberg et al. 2015) (Flynn et al. 1998).

In this thesis the main focus is set on the PTS_1-import, which is based on five successive steps, as shown in **Figure (2)**. The PTS_1-import is mediated by a highly conserved sequence of three amino acids (SKL) located in the extreme C-termini of target proteins, which are recognized by the TPR domain of the peroxisomal receptor protein Pex5p (Meinecke et al. 2010). Subsequently, the receptor-cargo complex is directed to the peroxisomal membrane, where it binds to the docking complex, Pex14p/Pex17p/Pex13p (yeast) / PEX14/PEX13 (human). The docking event induces the formation of a transient pore, and the cargo dissociates from Pex5p and translocates through the pore into the matrix. While Pex5 is being located in the membrane, its fate is determined by ubiquitination.

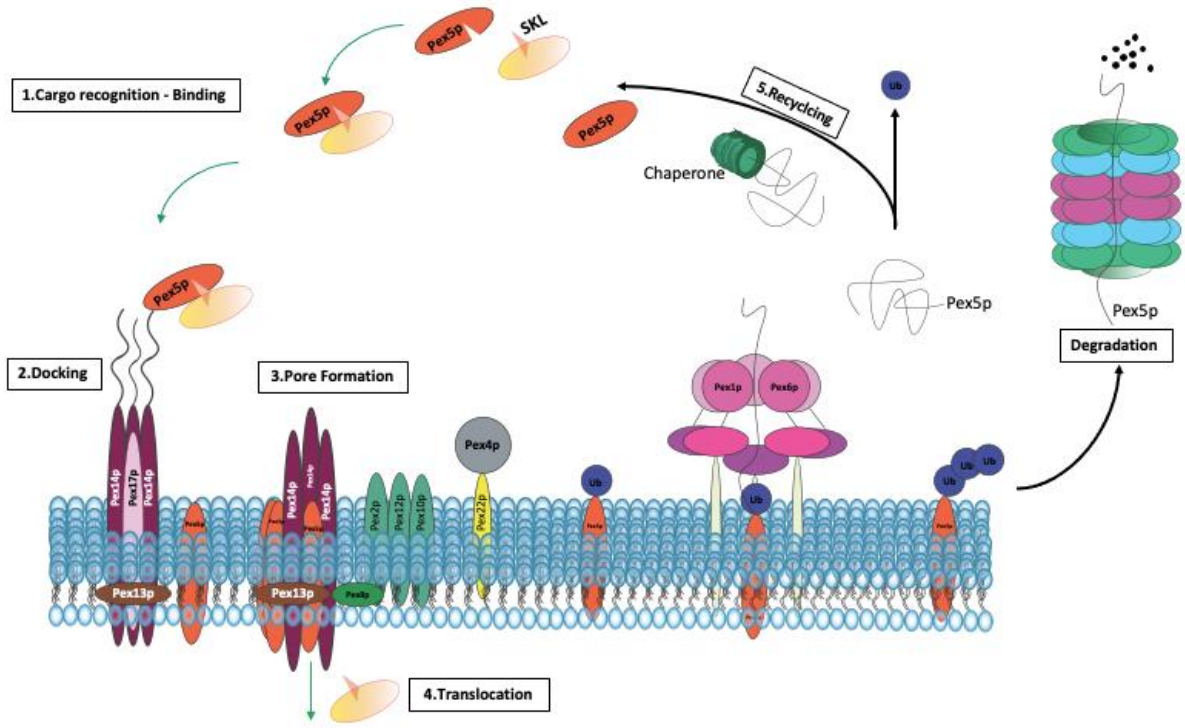

Figure (2): Schematic illustration of a PTS_1-import cycle. The import cycle is divided into 5 cycles.

(1): Cargo recognition and binding (Cytosol).

(2): Docking of the cargo-receptor complex to the docking complex (Peroxisomal membrane).

(3): Pore formation.

(4): Cargo translocation through the membrane and release in the peroxisomal lumen.

(5): Receptor ubiquitination and export (Recycling of Pex5).

Mono-ubiquitination takes place at the conserved Cys_{11}. As a result, Pex5p is recycled through the AAA^+ ATPase complex (Pex1p/Pex6p), back to cytosol, and can undergo new rounds of import after deubiquitination. Contrastively, poly-ubiquitination directs Pex5p to the proteasome for degradation (El Magraoui et al. 2019) (Hagen et al. 2015) (Platta et al. 2016) (Romano et al. 2019).

1.2.2 PTS_1-receptor peroxin, Pex5p

The yeast PTS_1 receptor protein Pex5p is a peroxin that appears well conserved among species (Baker et al. 2016) and is basically composed of two distinct domains. The N-terminal domain contains the highly conserved multiple pentapeptide *WXXXF/Y* repeats. These repeats are responsible for the PTS_1-receptor binding to Pex14p, included in the Docking/Translocon Module (DTM). The number of *WXXXF/Y* pentapeptide motifs varies among different species. In particular, the yeast N-terminal domain contains two motifs whereas the human homologue has seven such motifs **Figure (3)**. Concerning the C-terminal domain, it is highly conserved and it comprises seven tetratricopeptide repeat motifs (TPRs). The TPR region of the PTS_1 receptor is responsible for the recognition and the subsequent binding of the cargo (Watanabe et al. 2016).

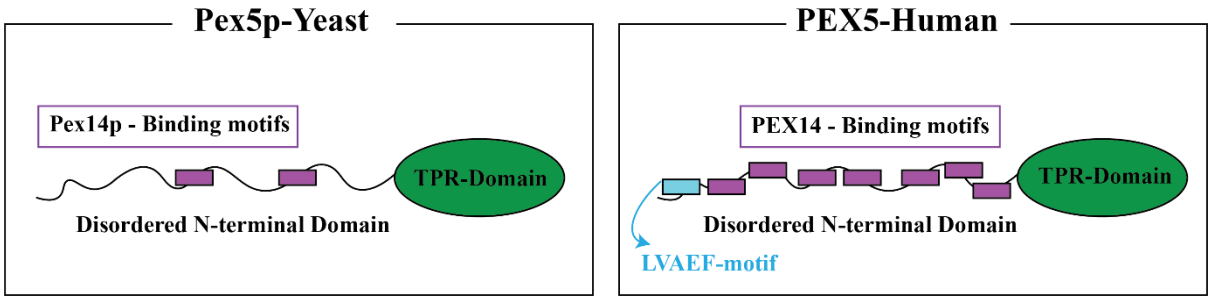

Figure (3): Schematic illustration of the PTS_1receptor comparing Yeast and Human homologs.
In both cases, the globular C-terminal domain accommodating the TPR motifs is quite similar. Differences are observed between the disordered N-terminal domains, where different numbers of *WXXXY/F* motifs exist in each homologue (Watanabe et al. 2016). An additional PEX14 binding motif (*LVAEF*) is located in human PEX5 (Neuhaus et al. 2014). Image was taken and modified from (Emmanouilidis et al. 2016).

The oligomeric state of Pex5p varies among species and moreover different physiochemical conditions can affect the states as well. Pex5p forms a monomer at a pH of ≃6.0 while it has been observed to dimerise at a pH of ≃7.2 (*Hansenula Polymorpha*) (Boteva et al. 2003). Furthermore, under non-reducing conditions, Pex5p has been found to form a tetramer of two dimers (Ma et al. 2013). In yeast (*Saccharomyces cerevisiae*) the PTS_1 receptor is a monomer with a natively unfolded N-terminus**.** The 3D model of the TPR domain (of the cargo receptor)

has been published and the highest resolution structure was determined by crystallography (Gatto et al. 2000).

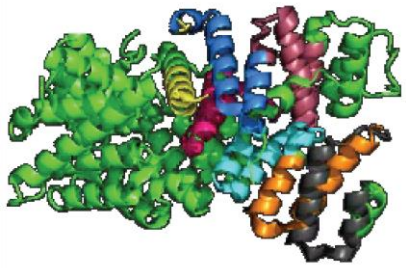

Figure (4): TPR domain of the cargo receptor.
The seven TPR domains can be distinguished by different colors in the schematic depiction of the cargo receptor.
TPR_1:335-368 (Yellow) TPR_2:369-402 (Hot-pink)
TPR_3:403-436 (Blue) TPR_4:452-486 (Orange)
TPR_5:488-521 (Cyan) TPR_6:522-589 (Red)
TPR_7:556-589 (Black)
Figure was made with Pymol, using PDB (1FCH)
DOI:(10.2210/pdb1FCH/pdb).

1.2.3 Pex5p - Cargo binding

The primary binding site of peroxisomal matrix proteins to the Pex5p-receptor, is a highly conserved PTS_1-target motif. The motif is located at the extreme C-terminus of the respective cargo proteins and is a three amino acid signal with the consensus sequence -[**S**/A/C]-[**K**/H/R]-[**L**/M]-$CO2^-$ (Lametschwandtner et al. 1998) that is recognized by the TPR-domain of the cargo receptor (Terlecky et al. 1995) (Stanley et al. 2006). The TPR is composed of seven repeats, each consisting of 34 amino acids, forming a pair of helices resulting in a helix-turn-helix motif, binding the signal-peptide (D'Andrea and Regan 2003). TPR_4 provides thereby conformational plasticity. By serving as a flexible scaffold it links the C-terminal part of the receptor (known as 7C-loop) with the two TPR motifs (TPR_1 - TPR_3 and TPR_5 - TPR_7). Upon cargo binding, the 7C loop undergoes substantial conformational changes, leading to a ring-like structure. Inside the ring, a pocket-like cavity allows binding of the PTS_1 cargo-protein anchors. Thus, a pseudo-circular formation, like a barrel (open from both sides), is generated (**Figure (5)**). (Hagen et al. 2015) (Stanley et al. 2006).

Other than PTS_1, additional contact sites reside amidst the cargo protein and the receptor. These sites are characterized as 'extended PTS_1' and are essential but not sufficient for peroxisomal protein import. The role of the extended PTS_1, is the enhancement of the binding affinity to Pex5p. This contact site is a dodecameric sequence of the last twelve residues located on the C-terminus of a cargo substrate, involved in the PTS_1 signal recognition. These twelve amino acids will interact with Pex5p regardless of the presence/absence of the SKL sequence (Hagen et al. 2015).

Apart from sequence recognition, hydrogen bonds form between highly conserved asparagine residues of the TPR motifs and the backbone of the PTS_1-targets, contributing to cargo binding. Nonetheless, these connections may differ among different cargo-proteins (Stanley et al. 2006).

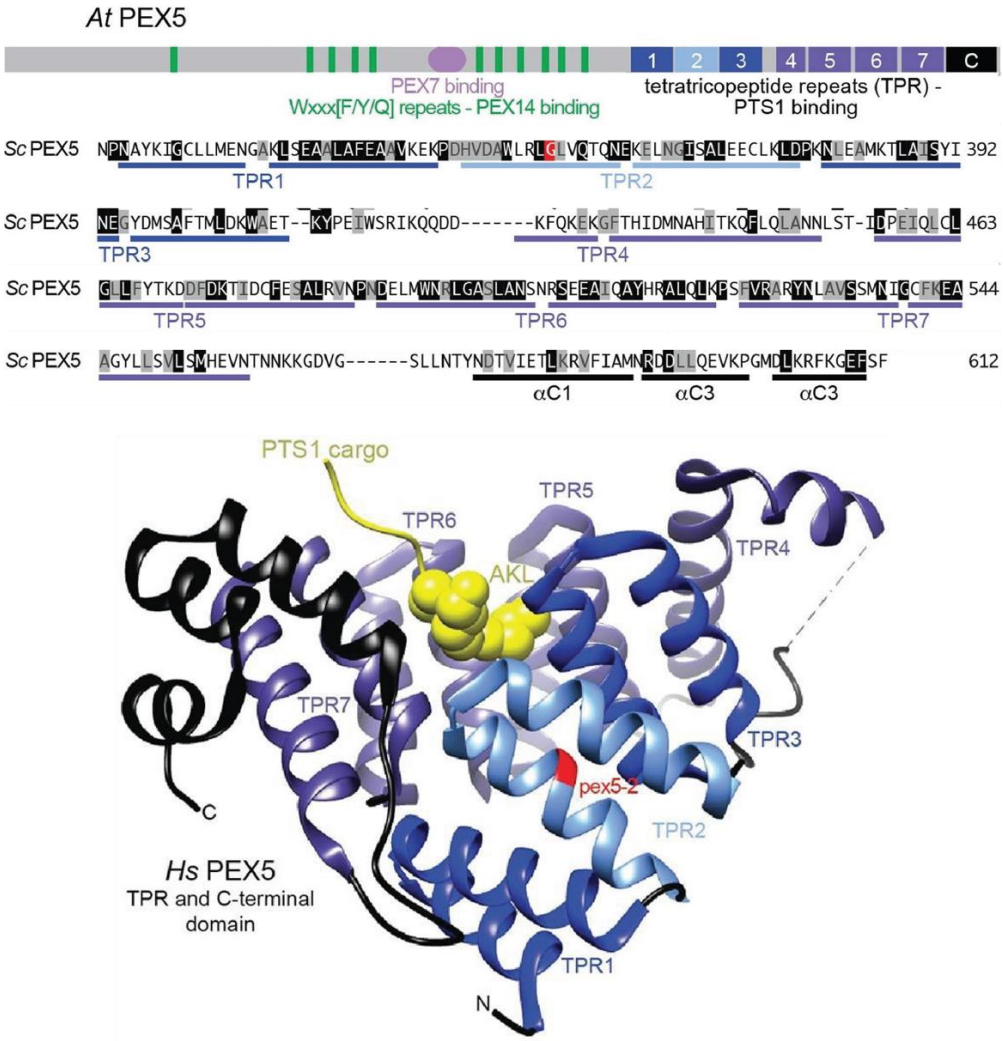

Figure (5): Schematic representation of the C-terminal sequence of PTS_1 receptor and the binding models' structure. Tetratricopeptide repeats (TPRs) are indicated with numbers 1-7. Following, the amino acid sequence of the C-terminal domain of *Saccharomyces cerevisiae* is displayed. Identical sequences with other organisms are highlighted in black, while chemically similar are highlighted in gray. Finally, a structure illustration of $PEX5_{TPR}$ domain in complex with a PTS_1 cargo protein (yellow) is displayed.
The ribbon diagram was generated from the PEX5-sterol carrier protein (SCP2) structure deposited in the Protein Data Bank under ID code (2C0L). DOI: (10.2210/pdb2C0L/pdb).Figure was taken and modified from (Patel et al. 2019).

Ma et al. additionally proved in their work that the formation or reduction of disulfide bonds on the highly conserved Cys_{10} residue regulates the oligomeric state of Pex5p and thereafter the cargo binding procedure. On the exterior of the peroxisomal membrane, Cys_{10} is able to

form disulfide bonds with the cargo, stabilizing this way the cargo-receptor complex (Ma et al. 2013).

1.2.4 Docking to the DTM - Translocation through the membrane

The N-terminus of Pex5p is an unstructured domain (Carvalho et al. 2006), that interacts with Pex14p, which in turn, anchors the receptor-cargo complex to the DTM. DTM consists of Pex14p, Pex13p and Pex17p (*S. cerevisiae*) and can be described as a docking platform construct that receives the cytosolic cargo (Dias et al. 2017) at the peroxisomal membrane. The diaromatic pentapeptide repeats (*WXXXF/Y*) are responsible for interaction with Pex14p and subsequently for the docking procedure (Saidowsky et al. 2001).

At the N-terminus of Pex14p, side chains of F_{35} and F_{52} obtrude from the surface of the protein molecule producing two separate pockets for the docking of the aforementioned *WXXXF/Y* motif of Pex5p. A_{32}, L_{53} and K_{56} also possess a vital role in the binding process (Neufeld et al. 2009). More precisely, binding is observed between *W*(first a.a of the motif)-F_{35} and *F*(fifth a.a of the motif)-F_{52} while at the same time, the fourth residue of the pentapeptide motif is crucial as an acidic amino acid for the formation of a salt bridge between K_{56} of Pex14p and the third amino acid of Pex5p (Neufeld et al. 2009). The 2nd motif does not present any binding with

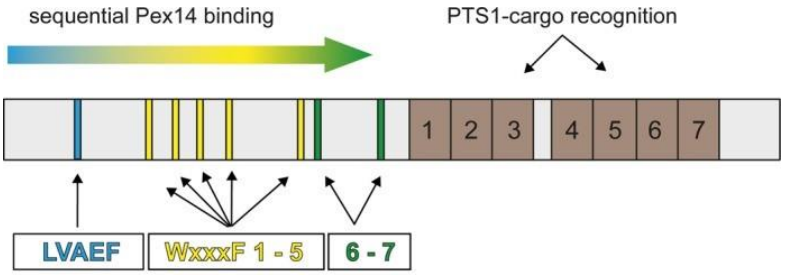

Figure (6): Schematic representation of sequential PEX5 binding to PEX14.

On the far right the 7 TPR peptides responsible for recognition of the target proteins are depicted in brown rectangles. On the N-terminus the *LVAEF* motif is represented with a blue band, while the 7 rest *WXXXF/Y* motifs accountable for PEX14 binding are illustrated with yellow and green bands. According to the sequential model, *LVAEF* initiates docking to the DTM and W_{1-5} interact with PEX14 during pore formation. Finally, $W_{6/7}$ bound to PEX14, causing cargo release. Figure was taken and modified from (Neuhaus et al. 2014).

Pex14p, due to the fact that it contains a *G* (*WGQDY*), thus prohibiting the pocket formation from the aromatic *W* and *Y* present in the motif. Finally, comparing the first and third motifs, *WAQHF* and *WAQEY* the presence of the negative residue clarifies the affinity discrepancy.

The existence of multiple docking-sites in Pex5p, either remedies sterical hindrance from larger sized cargo-proteins, or they are used with a sequential Pex14p binding-manner (shown and explained in **Figure (6)**) (Neuhaus et al. 2014).

Docking of Pex5p to DTM also contributes in positioning the PTS_1 receptor in the proper orientation for the upcoming monoubiquitination upon successful translocation of the cargo (Watanabe et al. 2016) (Platta et al. 2007).

Another integral membrane protein, Pex13p, is referred as a temporary component of the DTM and is suggested to be involved in the interaction network of Pex14p and Pex5p. The Pex5p-receptor binds in addition via its *WXXXF/Y* motifs to the SH3 domain of Pex13p (Azevedo and Schliebs 2006). Concerning Pex14p, the first 80 N-terminal amino acids are located in the peroxisomal matrix and bind Pex5p with higher affinity than the C-terminal binding site facing the cytosol (250-308 a.a) (Niederhoff et al. 2005) (Dias et al. 2017).

Moreover, in human, it has been shown that the SH3 and the N-terminal domain of PEX13, are able to bind to PEX5, as shown in **Figure (7)** below (Barros-Barbosa et al. 2019).

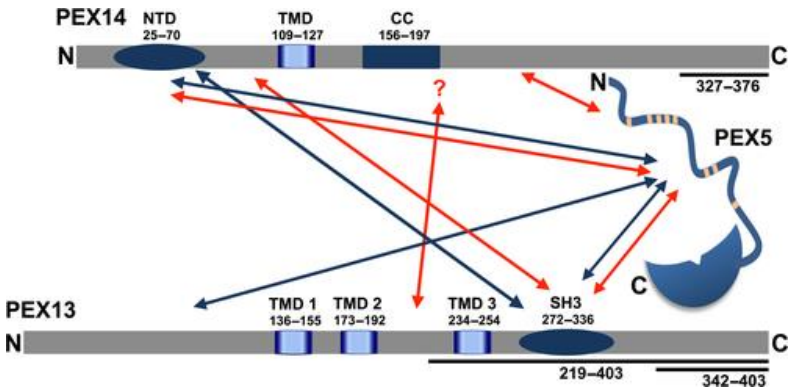

Figure (7): Schematic representation of the protein-protein interactions between DTM peroxins. TMD: Transmembrane Domain, CC: Coiled Coil, NTD: N-terminal Domain, SH3: Src Homology Domain. Figure taken from (Barros-Barbosa et al. 2019).

Pex5p in association with Pex14p are discussed to form together a transient pore in the peroxisomal membrane (Dias et al. 2017). Subsequently, cytosolic receptor-cargo complexes

are recruited by Pex13p and Pex14p to the DTM, where the interactions between Pex5p and these peroxins result into cargo release (Barros-Barbosa et al. 2019).

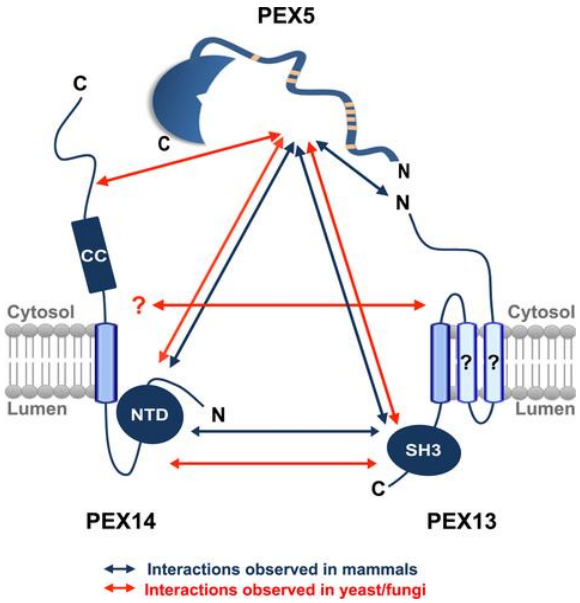

Figure (8): Illustration of membrane topologies of PEX14, PEX13.

N/CTDs topologies are demonstrated. With blue arrows the protein-protein interactions observed in mammals are depicted, while the interactions in yeast and fungi are given in red. The exact number of PEX13 TMDs is unknown, thus the cyan cylinders are marked with (?). Figure adapted from (Barros-Barbosa et al. 2019).

1.2.5 Cargo-release in the peroxisomal lumen

The exact molecular mechanism of cargo release is however not well understood and crucial mechanistic insights are still lacking.

After successful translocation, the cargo-receptor complex is located partially within the reducing environment of the peroxisomal matrix (Yano et al. 2010). Under these conditions, Pex5p transits to its homooligomeric form, which results into reduced affinity towards the PTS_1-containing cargo protein and subsequently cargo release (Ma et al. 2013). Another event that contributes in cargo release, is the binding of the Pex5p-NTD with another peroxin, Pex8p. This protein-protein interaction results in a conformational change in the TPR domain of Pex5p, which also reduces its binding affinity to the cargo. In mammals it has been reported that the N-terminus of PEX5 is antagonizing PTS_1-cargo for TPR binding (Harano et al. 2001).

1.2.6 Ubiquitination and the exportomer

Ubiquitination is the last step that determines the fate of Pex5p.

In the case of mono-ubiquitination, a conserved C_{11} residue is modified and Pex5p is designated for recycling upon extraction from the membrane via a AAA^+ ATPase (Pedrosa et al. 2018) (Fujiki et al. 2012) (Birschmann et al. 200) (Goto et al. 2011). The mono-ubiquitination on the C_{11} residue prevents poly-ubiquitination and therefore the degradation of Pex5p, preparing the recycling process (Schwartzkopff et al. 2015). In *S.cerevisiae* the mono-ubiquitination of Pex5p is catalyzed by other peroxins located in the peroxisomal lumen. In particular, Pex4p, (also mentioned as Ubc10p) is activated upon binding to the cytosolic domain of Pex22p, and serves as the ubiquitination conjugating enzyme (E_2). Additionally, a protein assembly comprising Pex2p, Pex10p and Pex12p constitutes a complex possessing E_3-enzymatic activity (Platta et al. 2016) (Meinecke et al. 2016). Pex10p connects Pex2p and Pex12p and at the same time these Really-Interesting-New-Gene (RING)-complex containing peroxins, form the aforementioned structure that is essential for Pex5p mono-ubiquitination.

In contrast, Pex5p poly-ubiquitination occurs on K_{18} and K_{24}, priming dysfunctional Pex5p for membrane release and consequent proteasomal degradation (Kiel et al. 2005) (Platta et al. 2004).

After ubiquitination, Pex5p is extracted from the membrane ATPase complex which is composed of Pex1p and Pex6p. The ATPase complex is anchored by the peroxin Pex15p to the peroxisomal membrane and is characterized as the Receptor Export Module (REM).

This peroxin-complex unfolds and translocates the ubiquitinated receptor from the membrane back to the cytosol (Romano et al. 2019) (Platta et al. 2005), in a procedure resembling processive threading (Pedrosa et al. 2018) (Fujiki et al. 2012) (Birschmann et al. 2003) (Goto et al. 2011).

Pex1p and Pex6p assemble into a heterohexameric complex with a stoichiometry of 3:3 (Birschmann et al. 2005) and unlike the import events, REM function depends on ATP hydrolysis (Miyata and Fujiki 2005).

1.3 Electron Microscopy (EM)

1.3.1 Setup of an electron microscope

Ernst Ruska (and his mentor Max Knoll) assembled the first Electron Microscope in the framework of his PhD thesis in 1931 (Knoll and Ruska 1932). They gave the term 'Elektronen Übermikroskop', due to the fact that the method was superior to light microscopy in terms of resolution. In 1939, while Ruska was collaborating with Kausche and Pfankuch, an important breakthrough was achieved, as they succeeded in visualizing the tobacco mosaic virus for the first time with an electron microscope (Kausche et al. 1939). Ernst Ruska (Kausche et al. 1939) shared the 1986 Physics Nobel Prize with Gerd Binnig and Heinrich Rohrer (designers of the scanning tunneling electron microscope in Zürich (1978)), for this achievement. This 'Übermikroskop' was initially used for physics and material science; however, in the early ninety-forties its first utilization in structural biology eventuated by Keith Roberts Porter**,** who initiated biological samples visualization such as the detail of the cell outline (Porter et al. 1945). He pioneered in the field with a multitude of findings (9+2 microtubule structure in the axoneme of cilia, naming of the endoplasmic reticulum). Although the theoretical resolution limit of an electron microscope was estimated 0.22 nm by replacing the light wavelength with the electron's wavelength at an accelerating voltage of 75 kV, such a resolution was only achieved forty years later (Bogner et al. 2007).

Cryo-electron microscopy was first introduced by a Swiss biophysicist in Heidelberg, Jacques Dubochet in 1980 (Dubochet 1987). Dubochet presented a unique sample preparation protocol that assisted in preserving biomolecules near native conditions inside a thin, amorphous ice layer, which permitted direct observation of the sample while working on liquid nitrogen temperatures or below (Murata and Wolf 2018). This approach, in combination with the new direct electron detectors, made it possible later to reach atomic resolution, and therefore obtain high-resolution structures with cryo-EM. Dubochet was awarded with the Chemistry Nobel Prize in 2017, sharing it with Joachim Frank (development of image processing methods of cryo-EM single particle data) and Richard Henderson (near atomic resolution structure analysis, using electron microscope).

After the recent advances in the field, cryo-EM revolutionized structural biology (Kühlbrandt 2014), as samples can be measured in conditions close to their native environment, in contrast to X-ray crystallography (Zhu and Zhu 2015) (Smith and Rubinstein 2014), declaring a new

era in the structural biology field (Doerr 2016) (Doerr et al. 2015) (Glaeser 2016). Nevertheless, X-ray crystallography still is the most preferred tool for structural analysis of smaller proteins.

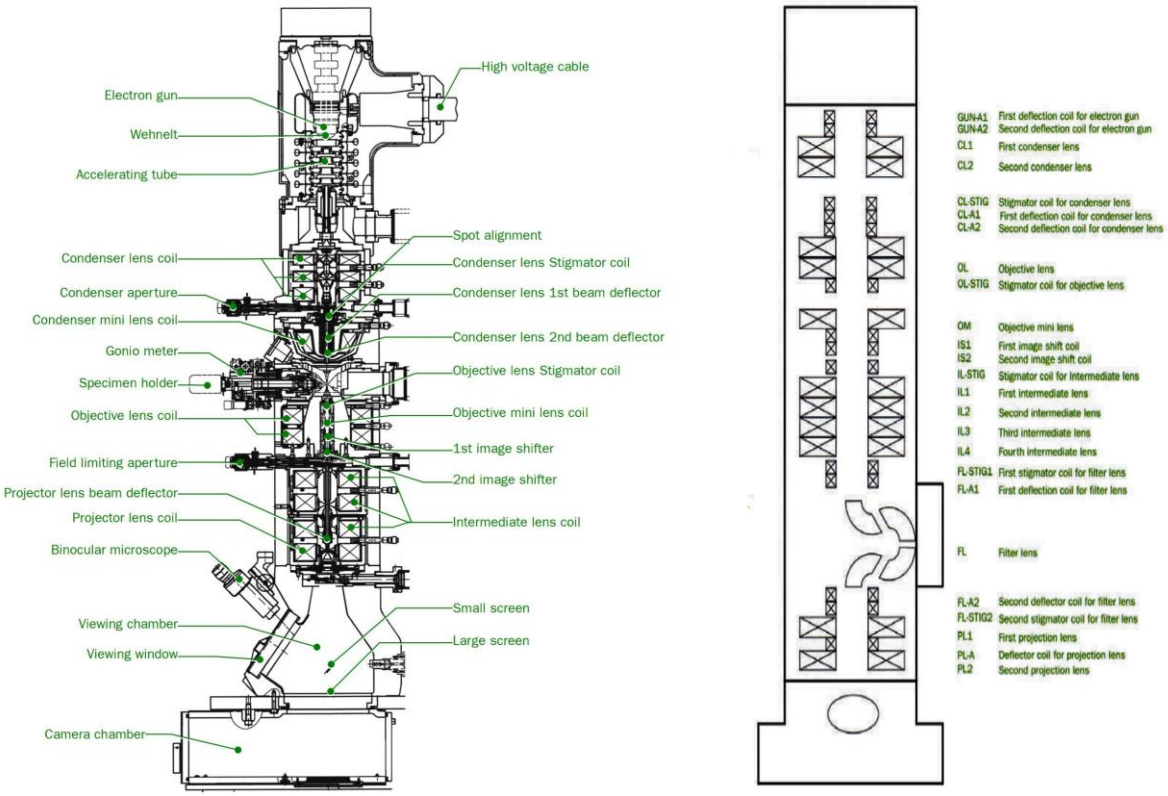

Figure (9): Setup of a Transmission Electron Microscope.

Drawing (**a**) and scheme (**b**) of a Transmission Electron Microscope. The 'electron gun' on the top is heated up emitting electrons that accelerate due to a voltage gradient and travel through vacuum. There are also four lens systems. Condenser, objective, intermediate and projection lens systems (from top to bottom). The sample is inserted in the sample chamber located exactly in between the condenser and the objective lenses. Finally, the image is visualized via a CCD or in new generation microscopes via a Direct Electron Detector. Figure is adapted from the user manual of the JEOL JEM1400 and JEM3200FSC. (https://www.aphys.kth.se/polopoly_fs/1.190438!/Menu/general/columncontent/attachment/TEM_manual_JEOL2100.pdf).

The basic setup of a Transmission Electron Microscope is given in **Figure (9)**. In general, the setup of a TEM microscope is comparable to a light microscope, while in transmission electron microscopy, accelerated electrons are used instead of photons.

Electron emission sources in TEM are termed electron guns. The electron guns are held at a very low voltage, while the bottom surface of the microscope is grounded (0kV). This results in the formation of an electric field that accelerates electrons nearly at 76 % of the speed of light. The most common electron guns in use are thermionic emitters like Tungsten filaments, Lanthanum Hexaborite (Lab_6) crystals or Field Emission Guns (FEGs). Since the quality can be defined as the coherence of the emitted electrons, FEGs offer the optimal condition as an

electron acceleration device. (ΔE=1.5-3eV for Lab_6 down to ΔE=0.2eV for a high brightness XFEG). The electrons are bundled into a beam going through the central axis of the microscope, under high vacuum conditions.

Most modern TEMs include a four-lens system. Each EM lens system consists of four basic components; two pairs of deflectors, a pair of stigmators, an aperture and the magnetic coils (lenses). In each lens system two pairs of deflectors are present, (set up perpendicular to the direction of the electron beam) and are responsible for redirecting the electron beam, by forcing the electrons to migrate through the microscope directly down the optical axis. Stigmators contribute by adding additional field strength compensating for the asymmetries caused to the beam by the lens itself, correcting astigmatism. The aperture serves as an insulator for the radiation that escapes the route of the optical axis by catching electrons deviating from the coherent beam. Four magnetic coils exist in the microscope. Starting from the top, there are the condenser lenses, C_1 and C_2. C_1 lens is responsible for focusing the beam to a certain spot, while the C_2 lens gathers the electrons emerging from the first spot and focuses them onto a specific region on the sample (Smith et al. 1983). The intensity of the beam is adjusted by modulating the position of the crossover position, by increasing and decreasing the strength of the C_2 lens, thus defining the region of the sample that is being illuminated. Directly below the C_2 lens, the specimen chamber is positioned. The sample is precisely positioned in the specimen chamber with the help of the 'specimen holder' (usually inserted from the side). Followed by this, the objective lens is located. Continuing to the microscopes' column, there reside the intermediate lenses (I_1, I_2, I_v) and the projection lens which define the ultimate magnification applied, using a pre-set combination of 'lens currents', prior to detection on a detector or fluorescent screen.

The task of the detector is to acquire information of the incoming electrons precisely along a given period of time, and ultimately transform this information into an image.

For example, in a CCD camera, electrons first collide with a scintillator converting them to light. Afterwards, the photons are transferred through a fiber optic bundle to a CCD camera where they are consequently converted to charge, which eventually is read out. (**Figure (10)**). A huge disadvantage of CCD detectors is the fact that upon collision of electrons with the scintillator, electrons might scatter with a big deviation from the entrty position, resulting in more than one delocalized count in the CCD camera (Downing et. al., Ultramicroscopy 75:215 (1999)). The aforementioned shortcoming of CCDs for imaging is remedied upon the recent development of direct electron detectors (Faruqi and McMullan 2018). The electrons arrive

directly to a CMOS imager and are converted immediately to charge. Moreover, the detectors have a higher read-out rate, allowing the collection of movies (Brilot et al. 2012).

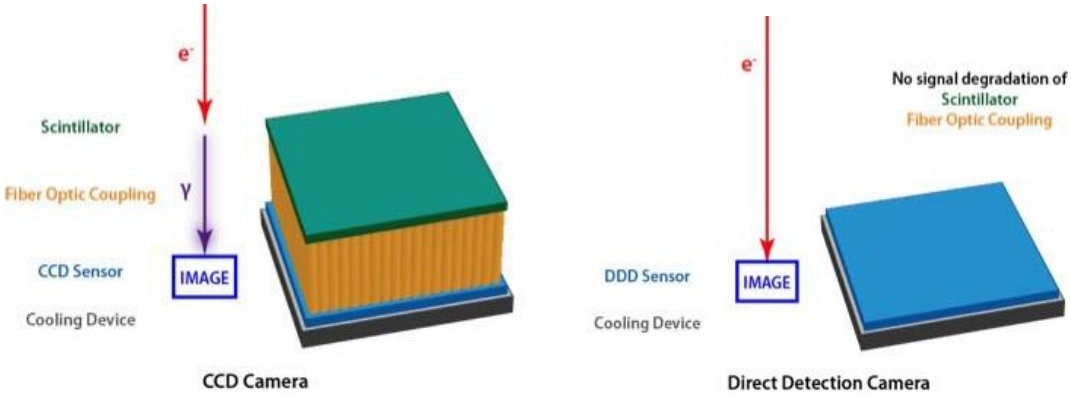

Figure (10): CCDs compared to Direct electron Detectors.

a) Illustrative depiction of a CCD sensor. Electrons are first converted to light, by colliding with a scintillator, that is transmitted through fiber optics to the CCD sensor which by turn converts photons into charge. **b)** Illustrative depiction of a Direct Electron Detector. Electrons in that case are directly detected from a CMOS imager (semiconductor material). Therefore, thermal background noise is reduced and the hurdle of the. scattering on the scintillator surface is overthrown. Image was taken from: Directelectron (de-series)

1.3.2 Image formation

In transmission electron microscopy the projection derived from a sample, is a real space-image containing amplitude and phase information. In that event, the image can be used directly for structure reconstruction in contrast to X-ray crystallography (Rhodes 2006).

Electrons have a dual nature, and can be considered as molecules and waves. (Broglie and De Broglie 1925).

When the electron beam comes across a dense molecule, it might scatter in different directions. Specifically, electrons may scatter in an elastic or in an inelastic manner. Inelastic scattering contributes to background noise and radiation damage. When electrons are inelastically scattered, their velocity (and energy) is reduced. These electrons are usually removed by the filters presented in section (**1.3.1)**.

Elastically scattered electrons carry all the valuable information of the sample, since they scatter from atoms without energy loss. However, most of the incident electrons pass the specimen without any interaction. To this effect, amplitude contrast is weak, not sufficient, and a phase contrast is needed in order to obtain a valuable image.

Electrons transmit through the microscope as planar waves that collide with the sample. Scattering centers of the sample will slow down the phase of a certain part of the electron wave

by creating 'phase ripples'. 'Phase ripples' in turn, will interfere with each other and each elastically scattered electron will interfere with the non-scattered electron beam, resulting in phase contrast.

Biological samples are really weak phase objects, since they mainly consist of Carbon (C), Oxygen (O), Phosphorus (P), Sulphur (S), Hydrogen (H) and Nitrogen (N), that do not scatter electrons very efficiently compared to inorganic materials (Rhodes 2006) (Nuclear Analytical Techniques in Medi...) (Advances in Atomic, Molecular, and Op...), leading to a minimal shift of the amplitude of the superimposed wave. For this reason in Transmission Electron Microscopy, during acquisition, a defocus in the scale of μm is applied to increase phase contrast (Zhu et al. 1997) (Orlova and Saibil 2011).

An EM image is a projected electron scattering density of an object modified by the 'Contrast Transfer Function' (CTF).

$$CTF = -2sinx(k, \Delta z) = -2sin\pi(\Delta z \lambda k^2 - \frac{1}{2} C_s \lambda^3 k^4)$$

k: spatial frequency, Δz: defocus, C_s: spherical aberration, λ: wavelength of the radiation

CTF is dependent on the defocus, the spherical aberration (C_s) and the wavelength that is being used (Reimer and Wächter 1978). However, each microscope has a specific spherical aberration and at the same time the wavelength depends on the acceleration voltage, thus these two values are constants. Therefore, the final contrast of the image depends on the defocus Δz that is applied and also the spatial frequency k (Orlova and Saibil 2011).

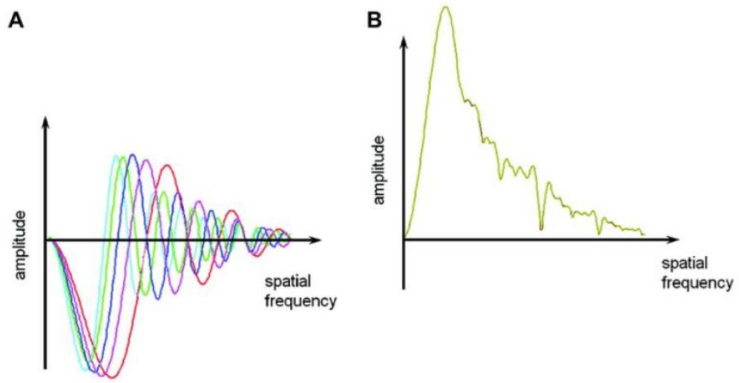

Figure (11): Contrast transfer function and transfer of overall contrast.

A) Contrast transfer functions close to focus (red) and with higher defocus (cyan). **B)** Summed absolute values of the curves in A, depicting the overall amplitude transfer at different frequencies. It is evident that in high spatial frequencies less information is collected. Figure taken from (Orlova and Saibil 2011).

Since electron sources and the magnetic coils (lenses) are not perfect, electrons have limited coherence. In spite of the aforementioned predicament, CTF is damped at high spatial

frequencies (**Figure (11.B)**). Therefore, high frequency components are affected crucially while the low frequency are not altered significantly. The "dampening" of the high frequency components, is termed CTF envelope function, and is depicted in **Figure (12)** below.

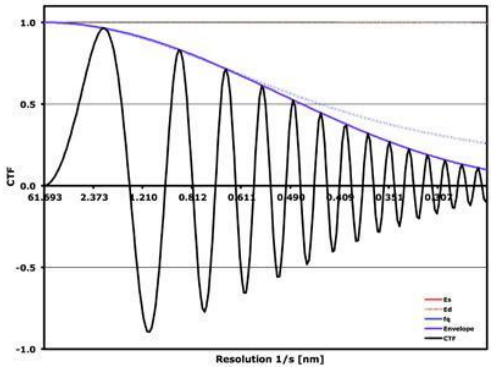

Figure (12): **Envelope function of CTF.** (Jiang et al. 2010)

By changing defocus values, the zero positions on a CTF plot (where the information is lost) would shift thus accordingly. Therefore, recording data in a series of different defocus compensates for the loss of information, since each individual defocus value counterbalances the zero points of the other (Zou et al. 2011), (Thon 1971). Finally, phase-flipping of the spatial frequencies that have negative components in the CTF (0, -1) by adding 180° to their phases, secures the correct amplitude of the contrast. As a result every component would be contributing contrast in the same way (positive contribution) (Penczek et al. 2014), (Jiang et al. 2010).

1.4 Sample preparation of proteins.

1.4.1 Negative stain

As described in section (**1.3.2**), the C, H, N, O, P, S atoms of the protein molecules impede the detected contrast. Hence, with regard to amplitude contrast, it is advisable to embed proteins in a heavy-metal containing stain solution (Harris 2007), since heavy metals increase the ratio of elastic to inelastic scattering (Vitturi and Zardi 1987). Biomaterials are enclosed within an aqueous film of negative stain solution, in order to produce a strong contrast between the background and the protein particle (Ohi et al. 2004) (De Carlo and Harris 2011). The choice of the heavy metal depends on the grain size. Respectively, uranyl acetate (UA) has a larger grain size and is therefore, more suitable for proteins with a molecular weight > 350 kDa. In

contrast, uranyl formate (UF) has a smaller grain size and is often used for smaller proteins (De Carlo and Harris 2011). Notably, the protein is not being directly visualized, as the result after staining of the biological samples corresponds to a footprint of the molecules. Furthermore, heavy metals can protect the sample and assist it in retaining its structural conformation during the drying process by enveloping it. However, the sample is dehydrated, large molecules are often flattened (Ohi et al. 2004) on the surface of the grid and in general this method can only provide low-resolution reconstruction of ~18 - 20 Å (Scarff et al. 2018).

Recent developments in transmission electron microscopy including data processing strategies (SPHIRE package (Wagner et al. 2019) (Wagner and Raunser 2020)) and sample preparation have resulted in better characterization and ultimately in the reconstruction of a multitude of membrane proteins.

1.4.2 Cryo-electron microscopy

In cryo-EM proteins are rapidly vitrified, without losing their hydration cell, in a close to native environment. As a result, proteins are fixated in an amorphous ice layer (Nogales and Scheres 2015). The vitrification process takes place with the help of cryo-plunge devices, where the sample is rapidly plunged into liquid ethane.

This technique is really sensitive since poor handling can lead to ice crystal contamination of the sample, which as a consequence, affects data acquisition.

A limitation of this technique is that the protein sample, during the creation of the ice layer, gets exposed to conditions and surfaces that are very different from the inside of a test tube/cell and it might even dissociate due to exposure to the air-water interface. The aforementioned effects cannot be calculated prior to screening and can be avoided upon addition of detergents (Passmore and Russo 2016).

2. Aim and motivation of this work

Mutations in the peroxisomal protein importing machinery, result in dysfunctional peroxisomal biogenesis and relate to a multitude of diseases like the Zellweger syndrome and other metabolic dysfunctions, that eventually lead to early death. Up to this point, the structure of several peroxins has been solved, but the field is still lacking structural insights into higher order assemblies and membrane complexes and especially into the mechanism of pore formation.

One of the main objectives of this thesis is the characterization of the yeast Pex14p, the major component of the yeast docking complex (consisting of Pex14p/17p/13p). Up to this point Pex14p was not characterized alone in the absence of Pex17p. Additionally, another goal was the reconstitution of Pex14p (and Pex14p/Pex17p) in circular lipid nanodiscs and comparative studies between the two assemblies, for the elucidation of Pex17p role to the docking complex. Moreover, another main point of this thesis was the purification of Human PEX14 and its characterization by electron microscopy.

Finally, the last main goal of this thesis was to study the formation of the peroxisomal transient pore. For this reason, peroxins comprising the importing machinery were reconstituted in liposomes.

3. Materials and methods

3.1 Materials

3.1.1 Instruments

Table (1): **List of used instruments**

Instruments	Manufacturer
Centrifuge 5424	Eppendorf (Hamburg, Germany)
Centrifuge Allegra® X-15R	Beckman Coulter (Brea, USA)
Centrifuge Avanti® J-26XP	Beckman Coulter (Brea, USA)
Centrifuge Rotors (JLA 8.100, JA-25.50, JA-10)	Beckman Coulter (Brea, USA)
Electroporator Gene Pulser Xcell™System	Bio-Rad (Hercules-California, USA)
FEI Vitrobot	FEI (Hillsboro, USA)
Incubator (37 °C)	BINDER (Tuttlingen, Germany)
Magnetic stirrer MR3000	Heidolph (Schwabach, Germany)
Micro-Äkta Purifier	GE Healthcare (Pittsburgh, USA)
Mini-membrane-vacuum pump Laboport®	KNF (St. Luis, USA)
Mini-Protean® Tetra-Cell	Bio-Rad (Hercules-California, USA)
Molecular Imager® Gel Doc™ XR System	Bio-Rad (Hercules-California, USA)
NanoDrop Spectrophotometer ND-1000	PEQLAB (Nuremberg, Germany)
pH-Meter FE20 Five Easy™	Mettler Toledo (Ohio, USA)
Pipettes PIPETMAN (0,2-2 µl, 1-10 µl, 2-20 µl, 100-1000 µl, 1-10 µl multi.)	Gilson (Wisconsin, USA)
Pipetting device	Hirschmann Laborgeräte (Eberstadt, Germany)
PowerPac 300	Bio-Rad (Hercules-California, USA)
PowerPac HV Power Supply	Bio-Rad (Hercules-California, USA)
Shaker	INFORS HT (Bottmingen, Switzerland)
Table top centrifuge 5417R	Eppendorf (Hamburg, Germany)

ThermoStat Plus	Eppendorf (Hamburg, Germany)
Ultrasonic bath	Sonorex Digitec Bandelin
Vortex-Genie 2	Scientific Industries (Bohemia, USA)

3.1.2 Microscopes

Table (2): List of used microscopes

Microscopes	Manufacturer
FEI Tecnai™ Spirit	FEI (Eindhoven, Netherlands)
JEOL JEM-1400	JEOL (Akishima, Tokyo, Japan)
TALOS Arctica	ThermoFisher Scientific GmbH (Waltham, USA)

3.1.3 Software

Table (3): List of used software.

Software	Website
ChimeraX	https://www.rbvi.ucsf.edu/chmerax/
crYOLO (Wagner et al.)	htpp://sphire.mpg.de
Eman2 (Tang et al. 2007)	http://blake.bcm.edu/emanwiki/EMAN2
MS Office	htpps://products.office.com/de
MotionCor (Tang et al. 2007; Zheng et al. 2017)	http://msg.ucsf.edu/em/software/motioncor2.html
SPHIRE (Moriya et al. 2017)	http://sphire.mpg.de
TranSPHIRE	http://sphire.mpg.de
Illustrator	https://www.adobe.com/de/
Origin	https://www.originlab.com/index.aspx?go=Products/Origin

3.1.4 Chemicals

Table (4): List of used chemicals.

Name	Supplier
2-(4_Hydoxyphenylazobenzoic acid (HABA)	Sigma-Aldrich (St. Luis, USA)
Bio-Beads™ SM-2 Adsorbent Media	Bio-Rad (Hercules-California, USA)
Boric Acid	GERBU Biotechnik GmbH (Heidelberg, Germany)
Cholic acid-Na-salt (Cholate)	SERVA Electrophoresis GmbH (Heidelberg, Germany)
Collodion solution 2% (in amylacetate)	Merck Millipore (Burlington USA)
cOmplete Mini EDTA-free Protease Inhibitor Cocktail	Sigma-Aldrich (St. Luis, USA)
Coomassie-Brillantblue R250	SERVA Electrophoresis GmbH (Heidelberg, Germany)
ddH_2O	-
Desthibiotin	Sigma-Aldrich (St. Luis, USA)
Ethanol (absolute p.a)	J.T Baker (Randor, USA)
Ethylenediaminetetraacetic acid (EDTA)	Sigma-Aldrich (St. Luis, USA)
Glycerol	Sigma-Aldrich Chemie GmbH (München, Germany)
Imidazole	Carl Roth GmH + Co. KG (Karlsuhe, Germany)
Magnesium Chloride ($MgCl_2$)	J.T Baker (Randor, USA)
Hydrochloric acid (HCL)	J.T Baker (Radnor, USA)
n-dodecyl-β-D-maltoside (DDM)	Anatrace (Maumee, Ohio, USA)
PageRuler™Protein Ladder	ThermoFisher Scientific GmbH (Waltham, USA)
Phenylmethylsulfonyl fluoride (PMSF)	Sigma-Aldrich (St. Luis, USA)
Sf-900 III SFM	ThermoFisher Scientific GmbH (Waltham, USA)
S.O.C medium	MPI Dortmund

Sodium chloride	Roth (Karlsruhe, Germany)
Sodium dodecylsulfate (SDS)	Roth (Karlsruhe, Germany)
Tris(2-carboxyethyl)phosphine hydrochloride (TCEP)	FLUKA (Buchs, Switzerland)
Trypan blue	FLUKA (Buchs, Switzerland)
Uranyl formate	Polyscience (Warrington, USA)
TRIS	Roth (Karlsruhe, Germany)

3.1.5 Consumables

Table (5): **List of used consumables**

Material	Supplier
10 cm petri-dish, sterile	Corning (New York, USA)
6-well plates (sterile)	Corning (New York, USA)
96-well deep well plates 2,2 ml	VWR (Radnor, USA)
Amicon®Ultra Concentrators	Millipore (Massachuset, USA)
Copper Grids G2400C	Plano EM (Wetzlar, Germany)
Econo-Pac® chromatography columns	Bio-Rad (Hercules-California, USA)
Eppendorf tubes (0,2 ml, 0,5 ml, 1,5 ml, 2 ml, 5ml)	Eppendorf (Hamburg, Germany)
Falcon Tubes (15 ml, 50 ml)	Eppendorf (Hamburg, Germany
Filterpaper Whatman No. 4	GE Healthcare (Chicago, USA)
Pipette tips(10 µl, 200 µl, 1.25 µl)	Sigma-Aldrich (St. Luis, USA)
Quantifoil 1.2 mesh 300 holey carbon grids	Quantifoil (Großlöbichau, Germany)
SDS-Gels Mini-PROTEAN TGX Stain Free Precast Gels (4-15%, 15 wells)	Bio-Rad (Hercules-California, USA)
Serological Pipettes, sterile (5 ml, 10 ml, 25 ml)	Sigma-Aldrich (St. Luis, USA)
Serological Rotilabo®-Pipettes	Roth (Karlsruhe, Germany)

3.1.6 Buffer Solutions

Table (6): **List of used buffer solutions**

General Buffers	Composition
SOC-Media	20 g tryptone 5 g yeast-extract 0.58 g NaCl 0.19 g KCl 2.03 g MgCl2 × 6 H2O 2.46 g MgSO4 × 7 H2O 50% glucose solution
10x HABA solution	24.22 mg HABA dissolve it in 99 ml mQ-H2O add 1ml 1N NaOH
Regeneration Buffer Strep-Column	1x HABA solution 100 mM Tris-HCl (pH 8) 150 mM NaCl 0.5 mM EDTA adjust to pH 8
SDS sample buffer	250 mM Tris-HCl (pH 8) 100 mM DTT 6% SDS 40% glycerol 0.02% Bromophenolblue
10x SDS running buffer	250 mM Tris-HCl (pH 8) 1.9 M glycine 2.8% SDS
Coomassie staining solution	0.15% Coomassie Brilliant Blue R250 12% Acetic acid 44% Ethanol
Coomassie destaining solution	10% Acetic acid
Cholate Buffer	50mM NaCl 50mM Tris pH=8.0 100mM Cholate (Cholic Acid-Na-salt)

3.1.7 PEX14 Purification Buffer Solutions

Table (7): **List of used buffer solutions for PEX14 purification**

PEX14 Purification Buffers	Composition
Resuspension Buffer	150mM NaCL 100mM Tris-HCl (pH 8) 10% Glycerol 1mM TCEP
Homogenization Buffer	150mM NaCL 100mM Tris-HCl (pH 8) 10% Glycerol 1mM TCEP 1% DDM
Wash Buffer (1) His-Column	150mM NaCL 100mM Tris-HCl (pH 8) 10% Glycerol 1mM TCEP 0,1% DDM 5mM Imidazole
Wash Buffer (2) His-Column	150mM NaCL 100mM Tris-HCl (pH 8) 10% Glycerol 1mM TCEP 0,1% DDM 10mM Imidazole
Elution Buffer (1) His-Column	150mM NaCL 100mM Tris-HCl (pH 8) 5% Glycerol 1mM TCEP 0,1% DDM 100mM Imidazole
Elution Buffer (2) His-Column	150mM NaCL 100mM Tris-HCl (pH 8) 5% Glycerol 1mM TCEP 0,1% DDM 250mM Imidazole
SEC Buffer (PEX14 soluble)	150mM NaCL 100mM Tris-HCl (pH 8) 0,1% DDM
SEC Buffer (PEX14 in NanoDiscs)	150mM NaCL

	100mM Tris-HCl (pH 8)

3.1.8 Cell Lines

Table (8): **List of used cell lines**

Organism	Name	Description
Escherichia coli	DH10EmBacY	F-mcrA Δ(mrr-hsdRMS-mcrBC) φ80lacZΔM15 ΔlacX74 recA1 endA1 araD139 Δ (ara, leu)7697 galU galK λ-rpsL nupG/ bMON14272/ pMON7124
Spodoptera frugiperda	Sf9	Immortalized insect ovarian cell line - line for virus production
Trichoplusia Ni	Hi5	Expression cell line

3.2 Methods

3.2.1 PEX14 Human purification

Hi5 cells, are harvested 72 hours after transduction by centrifugation at 4.500 rpm for 15 min at 4 ˚C. The cell pellet was resuspended in a 0.1% DDM containing buffer and lysed on the same day by crushing the cells thirty times using the glass homogenizer. During the lysis step, a final concentration of 1% DDM was used to solubilize the integral membrane protein PEX14. The crude lysate was incubated for one hour on a rotating platform at 4 ˚C and afterwards it was centrifuged at 25.000 rpm for one hour at 4 ˚C in a JA 25.50 rotor in order to separate the transmembrane protein from the membrane "debris" in the pellet.

Supernatant, containing the solubilized protein, was thereafter diluted in a 1:1 ratio with resuspension buffer to a final volume of 70 ml.

Then, the supernatant was slowly applied to an affinity-flow chromatography column packed with 5 ml of Nickel-NTA beads. The column was washed with 20 column volumes of wash (1) buffer, following another wash round of 20 column volumes of wash (2) buffer took place. Subsequently, a final washing step was performed with elution (1) buffer in order to get rid of His-tagged-dirt proteins coming from *Hi5* cells. Finally, PEX14 was eluted with 250 mM

imidazole containing elution (2) buffer, in 2 ml collecting steps. Purification success was assessed by SDS-PAGE (stain-free and Coomassie stain) electrophoresis. Pure fractions were thereafter combined and used for further purification steps and single particle analysis.

3.2.2 Liposome formation

Protein of interest (Pex14p(M51L)/Pex17p) was mixed with lipids in a ratio of 1:3 respectively. Additionally, the final mixture contained 0,1% DDM to prevent overhasty liposome formation. A typical preparation of liposomes was performed according to the following conditions summarized in **Table (9)**:

Table (9): **Liposome assembly composition mixture**

	Stock	**Molarity**	**Volume**
Buffer TBS + 0,1% DDM	150mM NaCl, 50mM Tris pH=8.0 + 0,1% DDM	245.85 mM	430 µl
Pex14p(M51L)/Pex17p	2 mg/ml	150 µM	65.5 µl
POPC lipids	50 mM in 100 mM Cholate	450 µM	4.5 µl
Total Volume	-	-	500 µl

The liposome mixture has to be prepared with the order described above. Additionally, each and every handling step has to be performed, at 4 °C (cold room) and incubated in the exact same temperature for at least 5 hours up to 15 hours. Following the preparation of the lipoprotein mixture, SM-2® Bio-Beads were used in order to remove DDM from the solution and enable liposome formation.

SM-2® Bio-Beads are washed extensively with a TBS buffer before use in order to equilibrate and activate them. Washing procedure consists of 3 identical rounds including a centrifugation step at 4 °C for 3 minutes at 11.000 rpm. Immediately after being activated SM-2® Bio-Beads were added directly to the liposome preparation in an eppendorf-tube and finally placed on a rotating platform inside the cold room for an overnight incubation running at 6.5 rpm (Knol et al. 1998). After 12-24 hours, liposomes were screened by negative stain EM in order to assess the result.

3.2.3 Nanodisc reconstitution

In order to keep the transmembrane proteins soluble and prevent the formation of undesired detergent micelles (Zhou and Cross 2013) (Cross et al. 2013), lipid nanodiscs (ND) were used as a tool to stabilize peroxins (Efremov et al. 2017). The reconstitution in lipid ND is a technique widely used for the purpose of characterizing transmembrane proteins with single particle analysis (Denisov and Sligar 2016).

The MSP1D1Δ4-6 ND-version produces a disc with 6-8 nm outer diameter, which is appropriate for peroxins. Adding to that, the circularized version of the ND prevents heterogeneity and offers additional stability (Miehling et al. 2018).

For the nanodisc assembly, cMSP1D1Δ4-6 was used, diluted in 20 mM Tris, pH=7.5, 200 mM NaCl, 0.5 mM EDTA and 1 mM TCEP. Resulting in a 6-7 nm nanodisc assembly, a size appropriate for the filamentous peroxisomal transmembrane protein molecules.

A typical preparation of nanodisc reconstitution was performed according to the following general conditions summarized in **Table (10)**:

Table (10): **Nanodisc assembly composition mixture**

	Molarity	**Volume used**
Protein (of interest)	440 mM	125 µl
DDM (0.1%)	689.83 mM	2.5 µl
cMSPD1Δ4-6	20 mM	45 µl
Lipids (POPC)	50 mM	2.25 µl
Cholate Buffer	50 mM	75.25 µl
Total	-	250 µl

After the ND mixture is prepared, overnight incubation at 4 °C (cold room) in a prepared ice-bucket is performed.

0.25 g of SM-2® Bio-Beads are washed extensively with a TBS buffer before use in order to equilibrate and activate the beads. Washing procedure consists of 3 identical rounds including a centrifugation step at 4 °C for 3 minutes at 11.000 rpm.

Following Bio-Bead activation, the mixed-sample is placed at the Bio-Beads tube and is incubated for 3-6 hours on the rotating wheel in the cold chamber. After the last incubation step, the mixture is separated from the Bio-Beads with the use of a syringe and is applied to a

new eppendorf-tube. Finally, the sample is spinned down at 3.000 g for 2 min at 4 °C and is ready for SEC analysis.

3.2.4 Negative stain

3.2.4.1 Preparation of negative stain grids

Copper grids are initially prepared by being covered with a collodion film.

A glass vessel is filled up to the middle with distilled H_2O. Three drops of collodion are added in the center of the vessel in close proximity to the H_2O surface in order to not disturb its surface. After a while, a plastic layer is visible on the surface. This process is repeated until the layer is uniformly covering the surface of the distilled H_2O, and the grids are placed on top of it, with the assistance of a filter paper serving as the anchoring platform. Grids are thereafter picked up and air-dried overnight. Subsequently, grids are coated with a carbon layer, with a thickness of 4.5 – 7 nm, by a carbon coating machine (Leica 600ACE). Finally, negative stain grids are glow-discharged, in order to get more hydrophilic, negatively charged and also have their surface "cleaned" prior to sample screening.

3.2.4.2 Negative Stain

Samples are embedded within a heavy metal salt film, containing uranyl acetate (UA) or uranyl formate (UF) in order to introduce heavy metal particles to the sample and therefore create enhanced amplitude contrast. Areas with thicker stain will scatter electrons stronger compared to areas with less stain (interior of particles). This is the reason why particles appear to be bright molecules with dark edges, on top of a dark-black background, resulting in naming the technique "Negative stain".

Sample is placed on top of the glow discharged surface of the grid and incubated for one minute. The grid is thereafter washed with two drops of 4 µl $_{dd}H_2O$ and finally incubated once again with 4 µl of stain for 40 s. Finally, excess stain is removed by blotting it away using a filter paper.

In the case of peroxins UF was used, because of their low molecular weight (40-70 kDa).

Best results were observed when blotting away in a manner that allows a thick layer of stain to remain on top of the molecules.

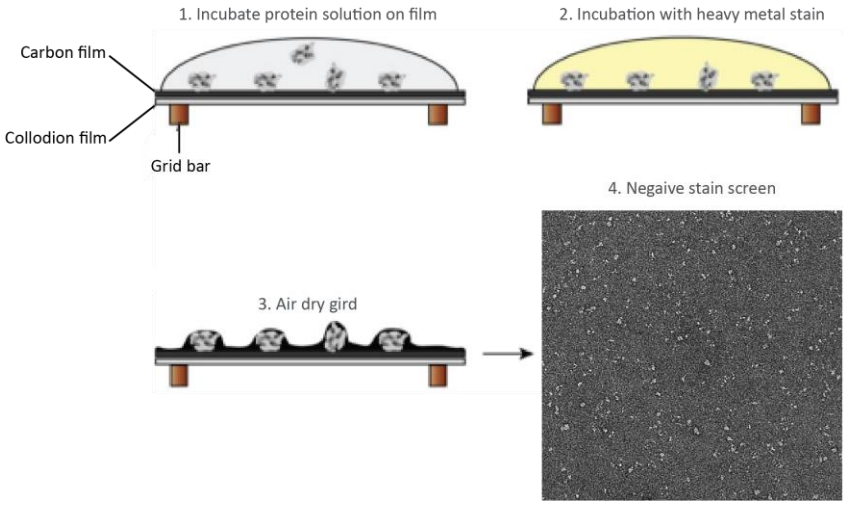

Figure (13): **Negative stain analysis preparation.**

1.In negative stain, protein samples are placed on carbon enveloped grids and (**2**) stained with a heavy metal solution (UF). **3.** Consequently, sample is air dried and the stain accumulates at the edges of the particles. Therefore, particles appear light on a dark background. **4.**Exemplary micrograph of Pex5p.

(Lydia Borgelt Master Thesis 2018)

3.2.5 Cryo-preparation

In order for samples to be analyzed with cryo-EM, their vitrification within a layer of amorphous ice is necessary. This is achieved by plunging sample-containing grids into liquid ethane (section (**1.4.2)**).

The vitrification step was performed using the Vitrobot Mark II system (FEI Eindhoven). Grids were fixed inside an 8 °C chamber and controlled humidity (100%), with the help of specific tweezers.

For the study of peroxins, Quantifoil 1.2 (mesh 300) grids were used. Grids were fixed to the specific tweezer and 4 µl of sample was applied. Excess sample was removed by blotting immediately for 3.5 seconds with a blotting force of 6 with a filter paper. Immediately, after the blotting step, grids were plunged into liquid ethane that was cooled down to -180 °C by liquid nitrogen. By using liquid ethane (section **(1.4.2)**), ice-crystal formation is overthrown. Thereafter, grids were transferred to precooled (with liquid nitrogen) grid-boxes and finally stored in a liquid nitrogen tank for future analysis.

3.2.6 Single particle reconstruction – Image processing

The aim of EM is to reconstruct a high-quality 3D-model of the under-investigation protein molecule. For this reason, information from 2D projections of proteins (in this thesis peroxins), is being collected by recording datasets using electron microscopes. Each particle present in

the dataset micrographs, has to be located and its unknown parameters, like orientation (angle, shift) have to be characterized, in order to project it back to 3D and compute a 3D reconstruction.

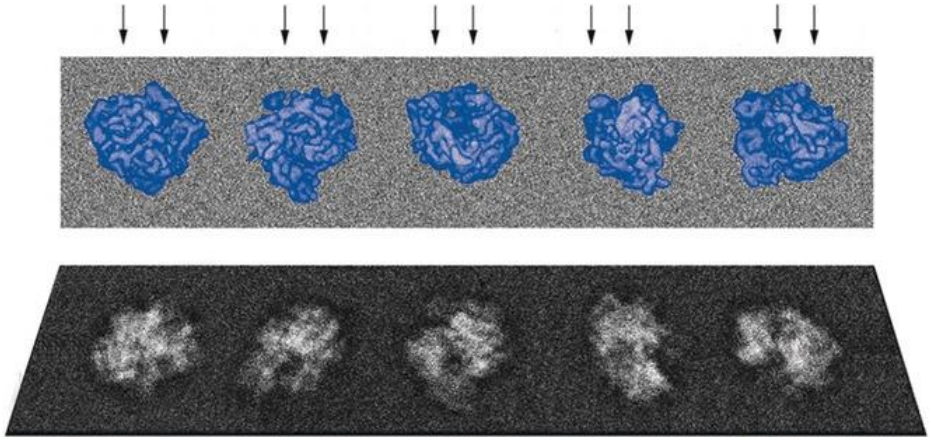

Figure (14): Schematic representation of single particle collection.

Particles depicted are fixed in vitrified ice and demonstrate different orientations. Below 2D-projections of each protein molecule are illustrated respectively. Figure was modified from (Frank 2018).

Numerous particles are therefore picked from the micrographs and are averaged. An illustration of 2D projections projected from a single 3D object is shown in **Figure (15.a)**.

a **b**

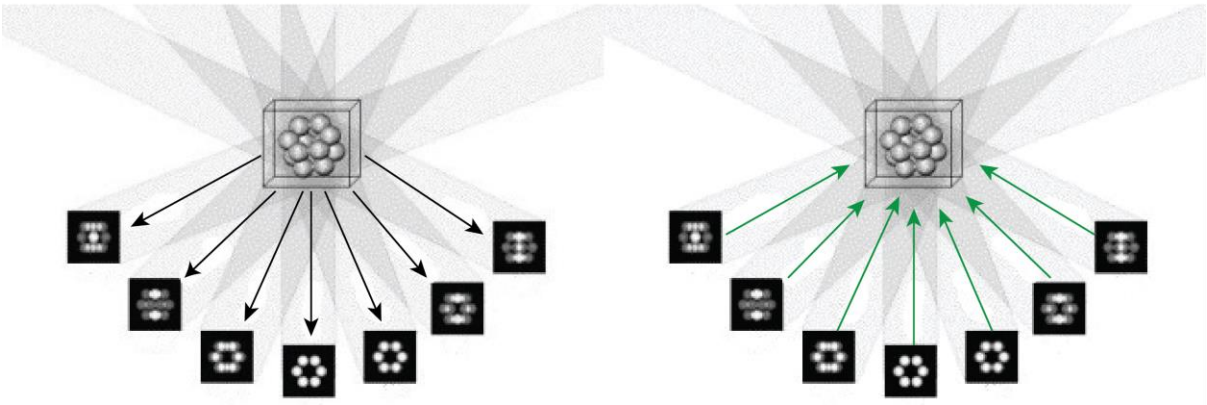

Figure (15): A schematic demonstration of different 2D projections resulting/reconstructing the 3D molecule.

a) Illustration of potential 2D projections gathered during a dataset collection.

b) Illustration of the back-projection of the 2D projections that results in the initial 3D model.

Figure was modified from (Bilbao-Castro et al. 2006).

This set of the recorded 2D-projection can be used vise-versa, meaning that the 3D structure that existed and gave rise to these projection images, can be calculated with '**back-projection**' of the 2D projections and following averaging (**Figure (15.b**).

Solving the structure of a protein, by recording the 2D projections, is best described by the 'Projection Theorem' (Garreau and Rudin 1987). According to this, the Fourier transform of a

single 2D projection of an object has the same amplitude and phase as a central slice that exists in the 3D Fourier transform of the object itself. By recording a large variety of projections with different angles and calculating the Fourier transforms of each of those images, a 3D Fourier transform of the object can be populated (Friedrich et al. 2009). The 3D model can be finally obtained by an inverse 3D Fourier Transformation (**Figure (16)**).

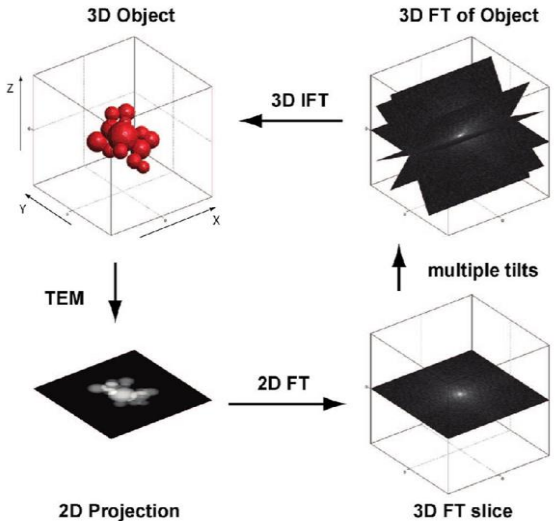

Figure (16): Schematic representation of the Projection Theorem.
Each individual Fourier transform of any 2D projection can be considered as a central section of the Fourier transform of the 3D object. By collecting/detecting enough 2D projection`s, the information needed for the 3D TF of the object will be accumulated and an inverse FT will finally reconstruct the protein molecule (Friedrich et al. 2009).

In order to identify a suitable region for high-magnification imaging and dataset collection, first images of the grid are collected at lower magnification (4000x). Most negative stain grids, display stain-gradients caused by the unilateral blotting of the excess stain solution. Regarding visualization of the small proxins, regions with thick stain layers were optimal.

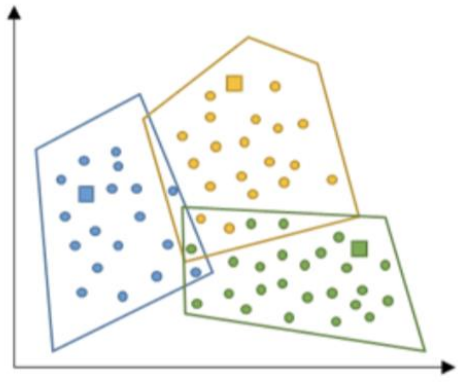

Figure (17): k-means clustering in 2D-space.
Clustering of particles depicted as points in a hyperspace in regard to random starting points forming 3 distinct class averages.
(Master Thesis Pascal Lill 2016)

After identification of the suitable region, higher magnification images were recorded using a 2x2 spotscan. From those images, single particles were selected and extracted manually using a box size of ⅓ larger than the longest particle diameter. Only particles that did not overlap with each other were selected and particles near to the edge of the recorded micrographs

were ignored. Further steps of image processing, following the collection of datasets, were performed with the software package SPHIRE (Moriya et al. 2017). Classification of the already picked particles was performed using the ISAC (Interactive Stable Alignment and Clustering) algorithm, that is a modified version of the k-means algorithm (Yang et al. 2012). Regarding k-means algorithm, as it is depicted in **Figure (17)**, the projection images of the protein molecules are regarded as points in a n-dimensional hyperspace, with n being the number of pixels. Hence, the corresponding axis value of each individual point is determined by the density value of a certain pixel. In principle, in this hyperspace a different combination of starting points **is** being set. According to **Figure (17)** if k=3, the algorithm will set 3 starting points. Each point will be clustered to the nearest reference starting point and three distinct class averages will form. Afterwards the center of each individual cluster will be used as the new reference and a new of iteration begins. If the sum of the distances of every class average remains identical after a new iteration, clustering comes to an end. ISAC uses the same principle, but performs multiple k-means rounds and validates the reproducibility of the class averages, after an initial reference-free 2D alignment of the images. This way, particles that do not classify and align in a stable manner, are excluded automatically (Cheng et al. 2015) (Yang et al. 2012).

Class averages coming from negative stain datasets were in turn, used to compute three dimensional models using RVIPER, based on the Validation of Individual Parameter Reproducibility (VIPER) method.

4. Results

$Strep_{II}$-Pex14p(M51L)/His_6-17p, His_6-Pex5p and $Strep_{II}$-Pex14p(M51L) were expressed in *E. coli* and purified with affinity chromatography. These peroxins were provided to the group by Dr. Tobias Hansen (AG Prof. Erdmann from the Institute of Biochemistry and Pathobiochemistry, Faculty of Medicine, System Biochemistry, Ruhr-University Bochum, Bochum, Germany).

4.1 Pex17p importance in the Pex14p/17p yeast docking complex

The peroxisomal yeast docking complex (DTM) serves as a docking platform for the receptor-cargo complex at the peroxisomal membrane (Urquhart et al. 2000). It comprises Pex14p, Pex17p, which are tightly associated and another transmembrane protein, Pex13p. However, little is known regarding the task of Pex17p in this process. The main responsibility of the DTM is the recruitment of Pex5p, and its corresponding cargo, to the peroxisomal membrane, where subsequently a transient pore is formed, to translocate the cargo-receptor complex.

In order to reveal the mechanism of the pore formation, the characterization of the DTM and its individual components is of high importance. For that reason, comparative studies between Pex14p/Pex17p and Pex14p were performed. Absence of Pex17p from the complex was anticipated to have an impact on Pex14p behavior, proving thus further structural evidence about the Pex17p role in the DTM.

4.1.1 Nanodisc reconstitution of $Strep_{II}$-Pex14p(M51L)/His_6Pex17p

Both Pex14p and Pex17p contain a single transmembrane helix. Therefore, the overall structure of the $Strep_{II}$-Pex14p(M51L)/His_6-Pex17p complex possesses a small transmembrane domain that is used for insertion in the peroxisomal membrane. The complex was reconstituted into lipid nanodiscs, in order to stabilize and analyze it with EM, in order to provide a close to native membrane environment.

As already mentioned in section **(3.2.3)**, cMSPD1Δ4-6 nanodiscs were used. The circularized nanodisc with a size of 6-7 nm is smaller and more heterogeneous, compared to commercially available MSP-nanodiscs (Miehling et al. 2018), which is crucial for the successful EM analysis of the small membrane peroxin complexes.

For the purpose of preparing the assembly, concentration of the $Strep_{II}$-Pex14p(M51L)/His_6-Pex17p complex was estimated to a total concentration of 2.2 mg/ml. Nanodisc reconstitution was performed according to the following conditions summarized in **Table (11)**:

Table (11): **$Strep_{II}$-Pex14p(M51L)/His_6-Pex17p reconstitution into cMSP11DΔ46**

	Molarity	**Volume used**
$Strep_{II}$-Pex14p(M51L)/His_6Pex17p	440 mM	113,67 µl
DDM (0.1%)	689.83 mM	2,5 µl
cMSP1D1Δ4-6	20 mM	45 µl
Lipids (POPC)	50 mM	2,25 µl
Cholate Buffer	50 mM	86,58 µl
Total Volume	-	250 µl

After all ingredients were transferred into one reaction tube, the sample was incubated overnight at 4 °C. Next day, the solution was placed in a reaction-tube containing 250 g of SM-2® Bio-Beads, in order to remove the detergent, with a three-hour incubation in 4°C.

Bio-Beads were removed and the assembled Pex14p/Pex17p-ND complex was separated from empty ND and excess lipids by size exclusion chromatography using a Superose 6 increase 5/150 GE column pre-equilibrated in TBS Buffer.

The main peak of the chromatogram (**Figure (18.a)**) elutes at a volume range of 1.25 – 1.9 ml. Verification of the protein quality was performed by SDS-PAGE gel (**Figure (18.b)**). The protein bands identified at a height of 50 and 29 kDa, correspond to Pex14p and Pex17p accordingly. An additional protein band, was identified at 12 kDa, matching the size of the cMSP1D1Δ4-6 ND which seems to co-elute with the Pex14p/Pex17p complex, suggesting that incorporation has been successful.

The 1.1 ml peak observed in the chromatogram represents the void volume, which contains the excess of lipids that were used for the reconstitution. Due to peroxin-reconstitution optimization, the peak appeared only at 0.3 mAU.

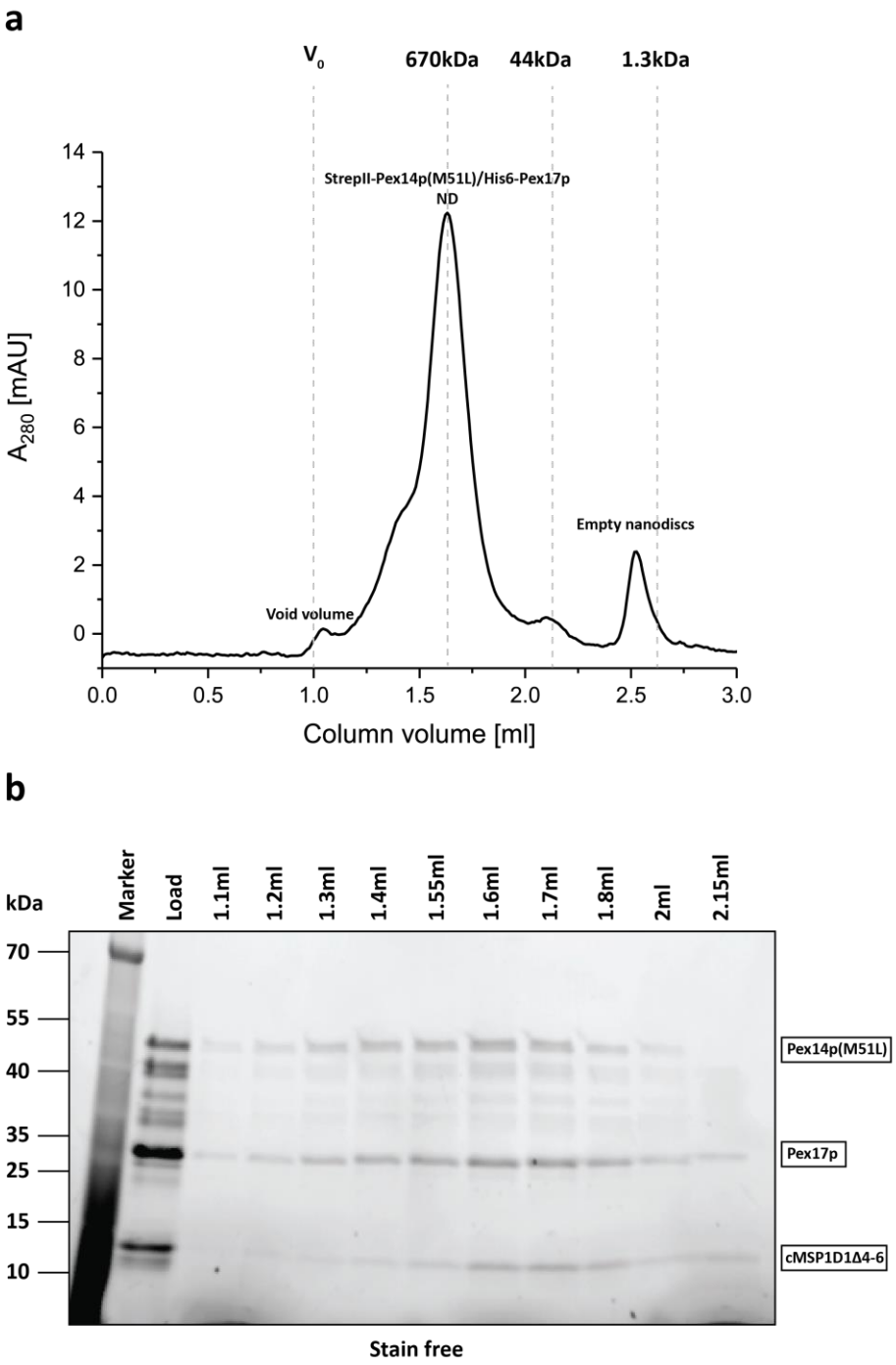

Figure (18): Size exclusion chromatography of the StrepII-Pex14p(M51L)/His6-Pex17p complex reconstituted into cMS1P1DΔ46 lipid nanodiscs.

a) Chromatogram of Superose 6 Increase 5/150 GE column of $Strep_{II}$-Pex14p(M51L)/His_6-Pex17p complex into ND after O/N incubation on SM-2® Bio-Beads. The 1.1 ml peak corresponds to the void volume. The main peak is observed at the range of 1.25 – 1.9 ml and includes the proteo-lipid assembly. Finally, at 2.5 ml the empty ND peak is observed.

b) Stain -free SDS-PAGE of 80µl fractions of the SEC purification. Pex14p(M51L), Pex17p and cMSP1D1Δ4-6 run at 50, 29 and 12 kDa accordingly.

Dashed lines represent the BioRad protein standard (#1511901).

Moreover, at 2.5 ml the empty nanodisc peak is detected.

Finally, at 2.15 ml another weak peak of 0.5 mAU is observed. This peak, in combination with the SDS-PAGE bands observed after electrophoresis, showed the presence of Pex17p reconstituted in the lipid ND. However, the concentration was not sufficient to perform electron microscopy analysis.

4.1.2 Negative stain analysis of the reconstituted complex

The corresponding fraction at 1.55 ml of the main chromatograms' peak, shown in **Figure (18.a),** was further analyzed with negative stain electron microscopy (**Figure (19)**) to further assess successful nanodisc incorporation. The visualized particles were identical to previous shown results (Lill et al.). A dataset of 324 micrographs was collected on JEOL JEM 1400 with a nominal magnification of 60.000x at a corresponding pixel-size of 1.84Å/pixel.

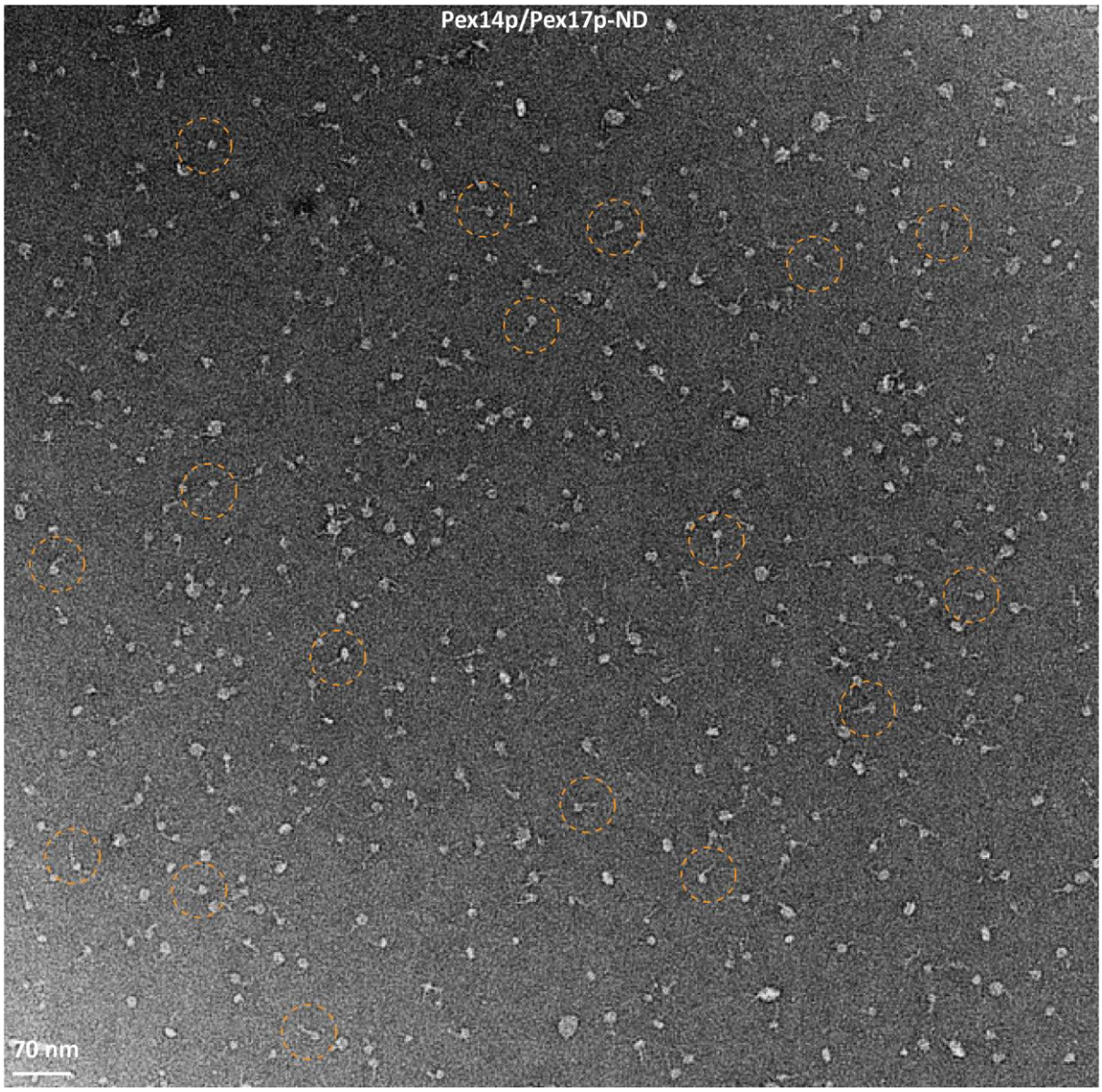

Figure (19): Negative stain micrograph of StrepII-Pex14p(M51L)/His6-Pex17p complex after being reconstituted into cMS1P1DΔ46 lipid nanodiscs. (scale bar is 70 nm).

Negative stain micrograph of $Strep_{II}$-Pex14p(M51L)/His_6-Pex17p complex reconstituted in ND. With dotted orange circles, examples of the proteo-nanodisc containing $Strep_{II}$-Pex14p(M51L)/His_6-Pex17p are indicated.

$Strep_{II}$-Pex14p(M51L)/His_6-Pex17p are indicated.

In total, 16,872 particles of Pex14p(M51L)/Pex17p in cMSPs were extracted, aligned and sorted using the SPHIRE package. As mentioned in (Lill et al.), class averages showed the characteristic rod-like shape with a side view preferred orientation. The elongated rod like structure revealed a particle length of 22 nm.

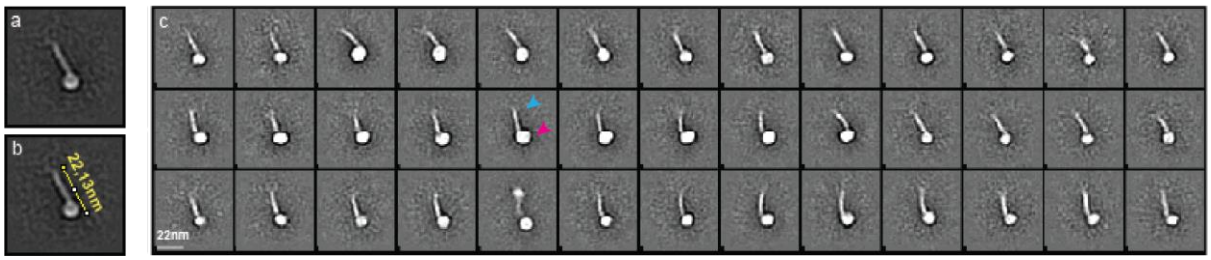

Figure (20): Exemplary class averages of negative stained Strep$_{II}$-Pex14p(M51L)/His$_6$-Pex17p complex after being reconstituted into cMSP1D1Δ4-6 lipid nanodiscs. (scale bar is 22 nm).

a) A single Strep$_{II}$-Pex14p(M51L)/His$_6$-Pex17p particle reconstituted into ND.

b) Diameter measurement of the rod-shaped particle with Fiji.

c) 2D classes of Strep$_{II}$-Pex14p(M51L)/His$_6$-Pex17p complex collected with SPHIRE. The circular density (hot-pink arrowhead) corresponds to the cMSP1D1Δ4-6, while the rod-shaped particle (cyan arrowhead) is inserted in the ND.

According to **Figure (20)**, and also (Lill et al.), the 2D-class averages revealed that only a single copy of the Pex14p(M51L)/Pex17p complex was inserted in the ND. Also, the complex appears to be a filamentous, (cyan arrowhead), with a single rod-like particle inserted within a single copy of circularized disc (pink arrowhead).

4.1.3 Negative stain analysis of Strep$_{II}$-Pex14p(M51L)

First of all, Strep$_{II}$-Pex14p(M51L) was purified alone. Analysis of Pex14p alone in the absence of Pex17p and comparative analysis to Pex14p/Pex17p would also provide valuable information about the structure of Pex17p and its role in the Pex14p/Pex17p complex.

Previous experiments showed that, within the Pex14p/Pex17p complex, the Pex14p individual molecules arrange in a coiled-coil-like assembly forming a pseudo symmetric homo-trimeric structure, resembling a thin filament (Lill et al.), whereas a single copy of Pex17p is incorporated with its two predicted coiled-coil domains into this arrangement.

For the purpose of handling Strep$_{II}$-Pex14p(M51L), buffer containing 0.1% DDM was used in order to keep the transmembrane protein in its soluble state.

For characterization, size exclusion chromatography using a Superose 6 increase 5/150 GE column pre-equilibrated in 0.1% containing TBS Buffer, was performed.

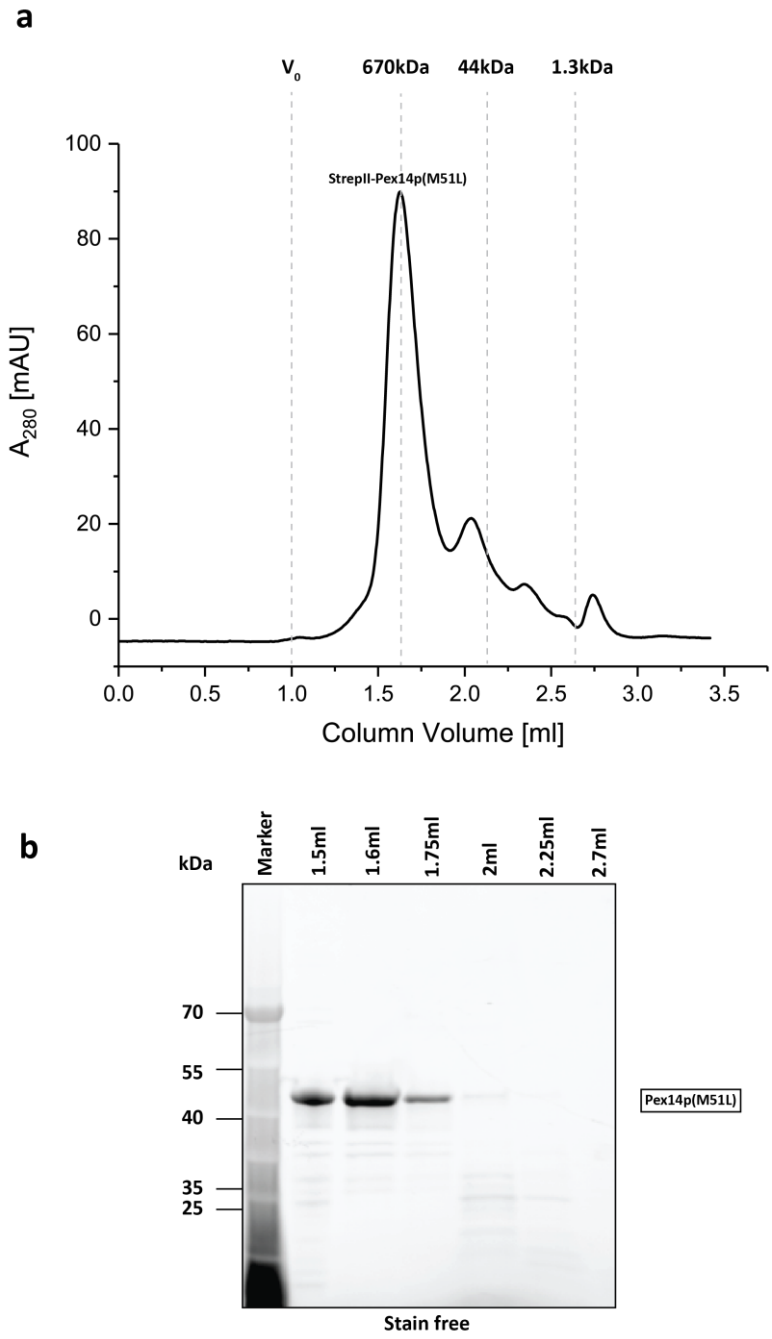

Figure (21): Size exclusion chromatography of StrepII-Pex14p(M51L).

a) Chromatogram of Superose 6 Increase 5/150 GE column of Strep$_{II}$-Pex14p(M51L). The main peak eluting at 1.25 – 1.8 ml corresponds to Pex14p. The peaks eluting at 2.1, 2.3, 2.7 ml could represent different oligomeric populations of Pex14p (monomer, dimer),

b) Stain - free SDS-PAGE of 80µl fractions of the SEC purification. The protein bands running at 50 kDa correspond to Pex14p.

Dashed lines represent the BioRad protein standard (#1511901).

The main peak of the chromatogram elutes at a volume range of 1.25 – 1.8 ml (**Figure (21.a)**). SDS-PAGE gel (**Figure (21.b)**), displays that the corresponding protein band of Pex14p runs at a height of 50 kDa.

Additionally, the SEC chromatogram revealed weak mAU peaks at 2.1, 2.3 and 2.7 ml, respectively. These peaks suggest that the previously characterized homotrimeric Pex14p bundle in the 3:1 Pex14p/Pex17p complex is unstable in the absence of Pex17p, and Pex14p (alone) forms instead dimers and monomers. However, according to SDS-PAGE analysis this requires further analysis.

The fraction of 1.6 ml of the main chromatograms' peak, shown in **Figure (21),** was further analyzed with negative stain electron microscopy (**Figure (22)**) in order to define the structural characteristics of the solubilized Pex14p. Collection of the dataset was performed as described above and 500 images were recorded with a nominal magnification of 60.000x that corresponds to a pixel-size of 1.84Å/pixel.

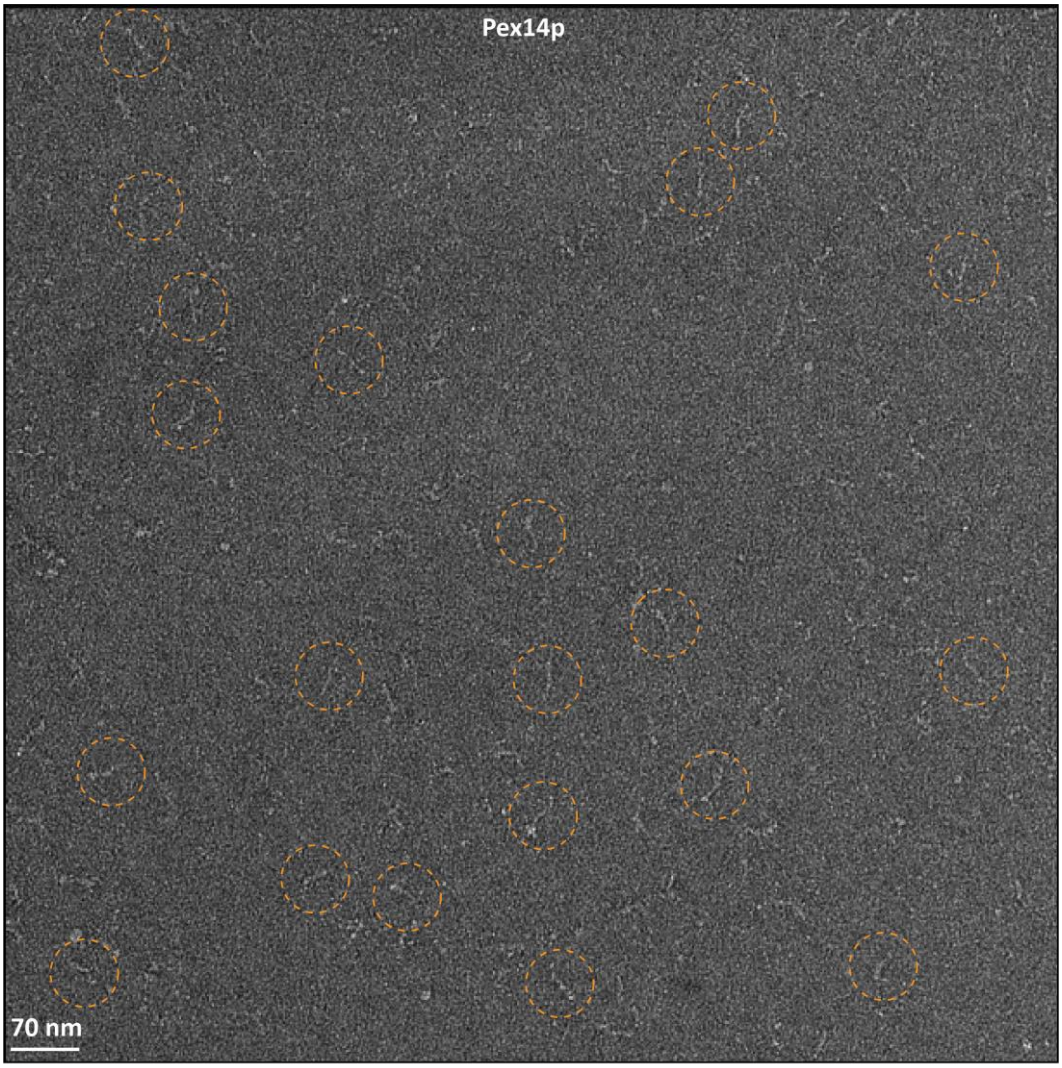

Figure (22): Negative stain micrograph of StrepII-Pex14p(M51L). (scale bar is 70 nm).

a) Negative stain micrograph of $Strep_{II}$-Pex14p(M51L).

b) With orange dotted circles, examples of $Strep_{II}$-Pex14p(M51L) are indicated.

Pex14p(M51L) appears to be a rod-shaped peroxin, resembling the Pex14p/Pex17p molecules.

Consequently, a dataset of $Strep_{II}$-Pex14p(M51L) was recorded and in total, 42,872 particles of Pex14p(M51L) were extracted, aligned and classified using SPHIRE.

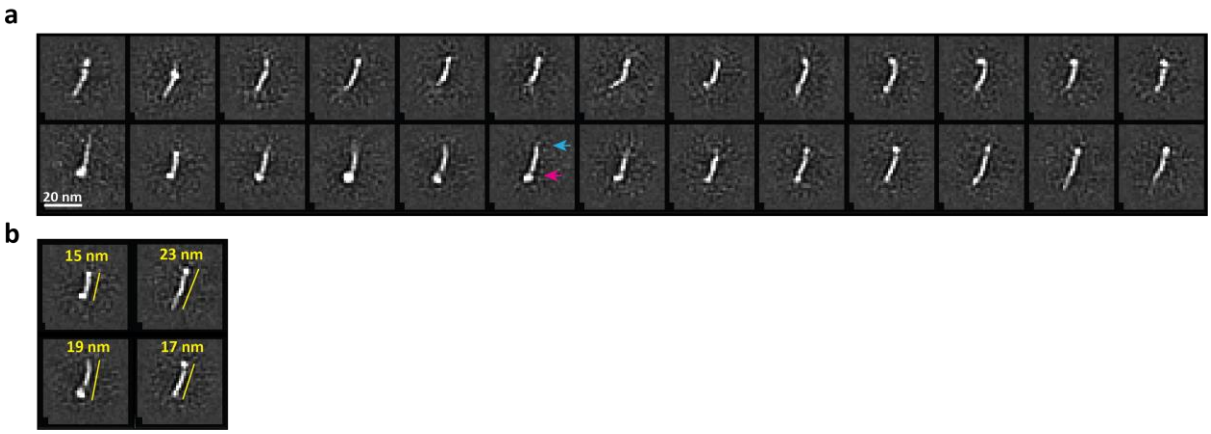

Figure (23): Exemplary 2D classes of negative stained StrepII-Pex14p(M51L). (scale bar is 20 nm).
a) 2D classes of Strep$_{II}$-Pex14p(M51L) obtained by using the SPHIRE package. With a cyan arrowhead, the detergent micelle is indicated and with the hot-pink arrowhead the filamentous protein molecule is pointed out correspondingly.
b) Schematic of 4 distinct Strep$_{II}$-Pex14p(M51L) 2D classes demonstrating the variance observed regarding the rod-size.

A high variety of Pex14p particles is observed regarding their size and at the same time their thickness as well, as it is shown in the 2D class averages in **Figure (23.b).** Pex14p appears to be a filamentous, rod-shaped molecule (cyan arrowhead) that is inserted inside a detergent micelle (pink arrowhead), which appears, similar to the lipid ND, as a bulky region. The size of the filament varies between 15 nm and 22.3 nm.

4.1.4 Nanodisc reconstitution of Strep$_{II}$-Pex14p(M51L)

Strep$_{II}$-Pex14p(M51L) was reconstituted into lipid nanodiscs, to provide a close to native, homogeneous lipid environment. This experiment will also enable a side to side comparison of Pex14p/Pex17p and Pex14p.

Strep$_{II}$-Pex14p(M51L) was purified alone in *E. coli*, in the absence of Pex17p and subsequently reconstituted into cMSP1D1Δ4-6. For the purpose of preparing the assembly, concentration of Strep$_{II}$-Pex14p(M51L) was estimated to 1.74 mg/ml. Therefore, nanodisc reconstitution was performed according to the following conditions summarized in **Table (12)**:

Table (12): **Strep$_{II}$-Pex14p(M51L) reconstitution into cMSPD1Δ4-6**

	Molarity	Volume used
Strep$_{II}$-Pex14p	440 mM	143,7 µl
DDM (0.1%)	689.83 mM	2,5 µl
cMSP1D1Δ4-6	20 mM	45 µl
Lipids (POPC)	50 mM	2,25 µl
Chocolate Buffer	50 mM	56,55 µl
Total Volume	-	250 µl

The mixture was incubated overnight at 4 °C. Next day, the mixture was placed in a reaction-tube containing 250 mg of SM-2® Bio-Beads, in order to remove the detergent, by a three-hour incubation in 4 °C.

Bio-Beads were discarded and the assembled Pex14p-ND complex was separated from empty ND and excess lipids by size exclusion chromatography using a Superose 6 increase 5/150 GE column pre-equilibrated in TBS Buffer (**Figure (24.a)**).

The peak eluting at 1.1 ml represents the void volume due to excess of lipids.

The main peak of the chromatogram trace elutes at a volume range of 1.25 – 2 ml. SDS-PAGE analysis (**Figure (24.b)**), revealed protein bands running at a height of 50 and 12 kDa, which correspond to Pex14p and cMSPD1Δ4-6 ND, respectively. This supports the successful reconstitution of the proteins, as the lipid ND is co-eluting with Pex14p.

Finally, at 2.5 ml the empty nanodisc peak is detected.

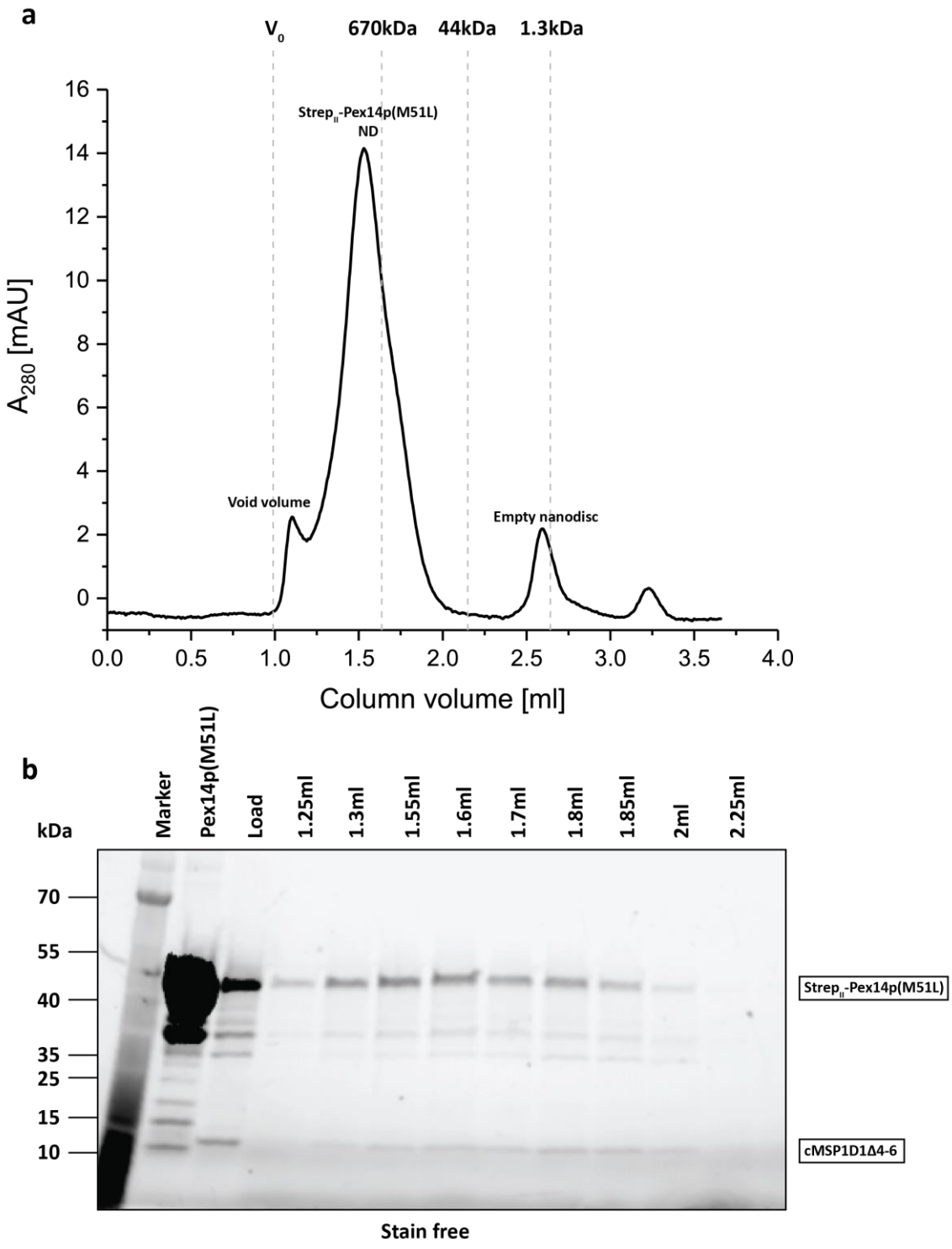

Figure (24): Size exclusion chromatography of the Strep$_{II}$-Pex14p(M51L) reconstituted into cMSP1D1Δ4-6 lipid nanodiscs.

a) Chromatogram of Superose 6 Increase 5/150 GE column of Strep$_{II}$-Pex14p(M51L) reconstituted into ND after O/N incubation on SM-2® Bio-Beads. The 1.1 ml peak corresponds to the void volume. The main peak is eluting at 1.25 – 2 ml and it corresponds to the Pex14p-ND assembly. Finally, at 2.5 ml the empty ND peak is eluting.

b) Stain - free SDS-PAGE of 80µl fractions of the SEC purification. Protein bands running at 50 kDa correspond to the Pex14p peroxin, while at 12 kDa the cMSP1D1Δ4-6 ND is running.

Dashed lines represent the BioRad protein standard (#1511901).

4.1.5 Negative stain analysis of Strep$_{II}$-Pex14p(M51L) reconstituted to lipid nanodiscs

The fraction of 1.6 ml shown in **Figure (24.a),** was further analyzed with negative stain electron microscopy (**Figure (25)**) to assess successful nanodisc incorporation.

226 micrographs were recorded on a JEOL JEM 1400 at a nominal magnification of 60.000x corresponding to a pixel-size of 1.84Å/pixel.

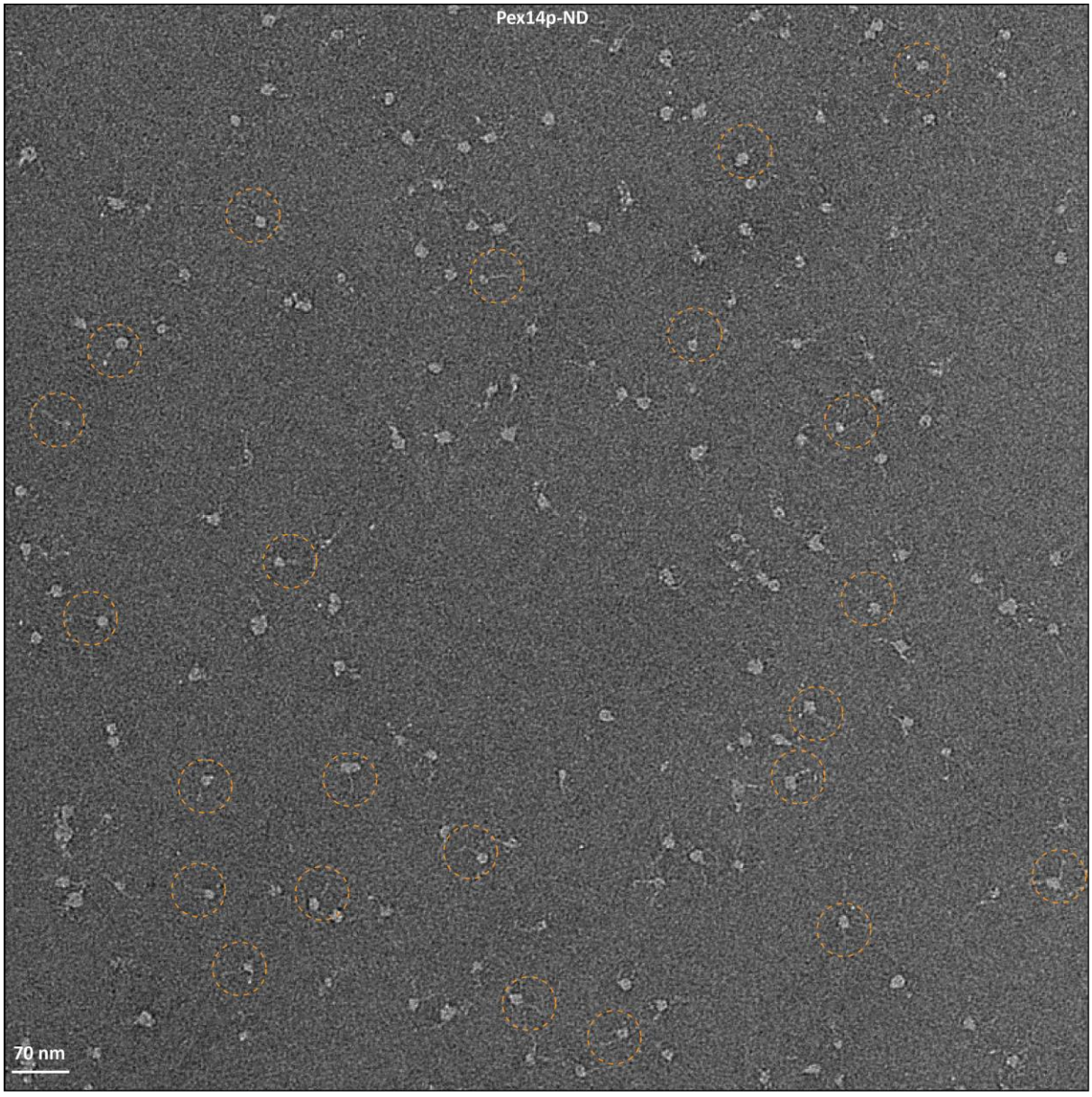

Figure (25): **Negative stain micrograph of Strep$_{II}$-Pex14p(M51L) reconstituted in ND. (scale bar is 70 nm).**

a) Negative stain micrograph of Strep$_{II}$-Pex14p(M51L) reconstituted into lipid ND.

b) With dotted circles, examples of the proteo-nanodisc containing Strep$_{II}$-Pex14p(M51L) are indicated.

The ND-reconstituted particles, appear to be comparable to the Pex14p/Pex17p-ND molecules.

In total, 15.876 particles of Pex14p(M51L) were extracted from these images, aligned and classified using the SPHIRE package.

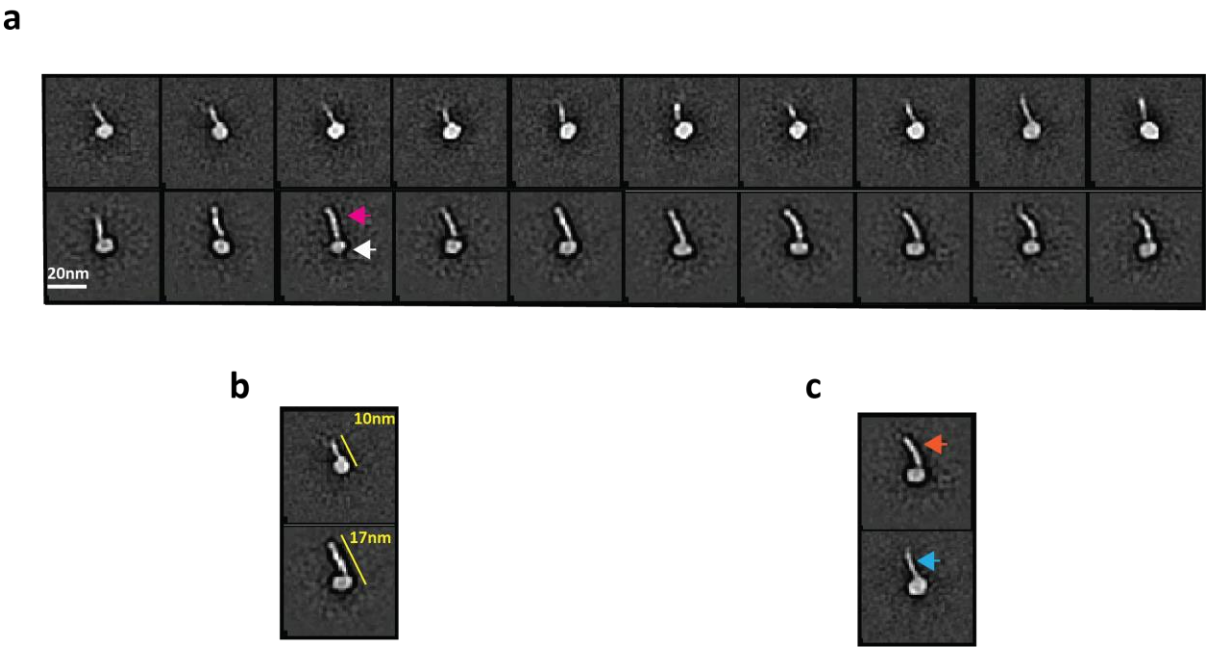

Figure (26): Exemplary class averages of negative stained Strep$_{II}$-Pex14p(M51L) after being reconstituted into cMSP1D1Δ4-6 lipid nanodiscs. (scale bar is 20 nm).

a) 2D classes of Strep$_{II}$-Pex14p(M51L) reconstituted into cMSP1D1Δ46 ND. With the white, the lipid ND is indicated, while with the hot-pink arrowhead, Strep$_{II}$-Pex14p(M51L) is.

b) Using Fiji to measure particle diameter, a schematic illustration depicts differences in the length size of the resulting 2D classes.

c) Variance in the filament width of Strep$_{II}$-Pex14p(M51L) is shown in this pair of particles indicated orange and blue arrowheads correspondingly.

The 2D-classification of Pex14p-ND assembly, resulted in diverse 2D class averages. Pex14p appears to be, as expected, a filamentous, rod-shaped molecule (pink arrowhead) that is inserted inside the ND (white arrowhead), which is visible as a bulky region.

The length of the particles, ranges between 10 nm and 22.3 nm. In addition, the 2D-classes show variance in the width of the filament as well. In **Figure (26.c)**, for example, the rod marked with the red arrowhead, appears denser than the one indicated with the cyan arrowhead.

4.2 Sngle particle analysis of PEX14 of the human docking complex

Although human PEX14 has been suggested having the same cellular function as yeast Pex14p, both molecules show distinct structural differences. The human docking complex consists of PEX14 and PEX13 and apparently Pex17p is not required at all in higher eukaryotes. Mammalian and yeast orthologues have only a 26-29% sequence identity with an overall similarity ranging between 43-45% throughout the entire peroxins' length (Will et al. 1999). Human PEX14 can also bind PEX5 on a non-canonical *LVxAF* motif, diverging from Pex14p (Neuhaus et al. 2014) (**Figure (3)**). Additionally, due to absence of Pex17p it is expected that

there might be differences concerning PEX14 topology and oligomerization in the peroxisomal membrane.

For this reason, using the bacmid system and expression in *Hi5* insect cells, PEX14 was expressed in significant yield and thereafter incorporated into circular lipid nanodiscs for further comparative studies.

4.2.1 Expression - Purification of PEX14 into Hi5 insect cells

After generating the viruses carrying His_6-PEX14, *Hi5* insect cells were infected. After the expression time frame of 72 hours was over, cells were harvested and centrifuged using the Avanti® J-26XP centrifuge with the JLA 8.100 rotor, at 4.500 rpm for 15 min at 4˚C. The

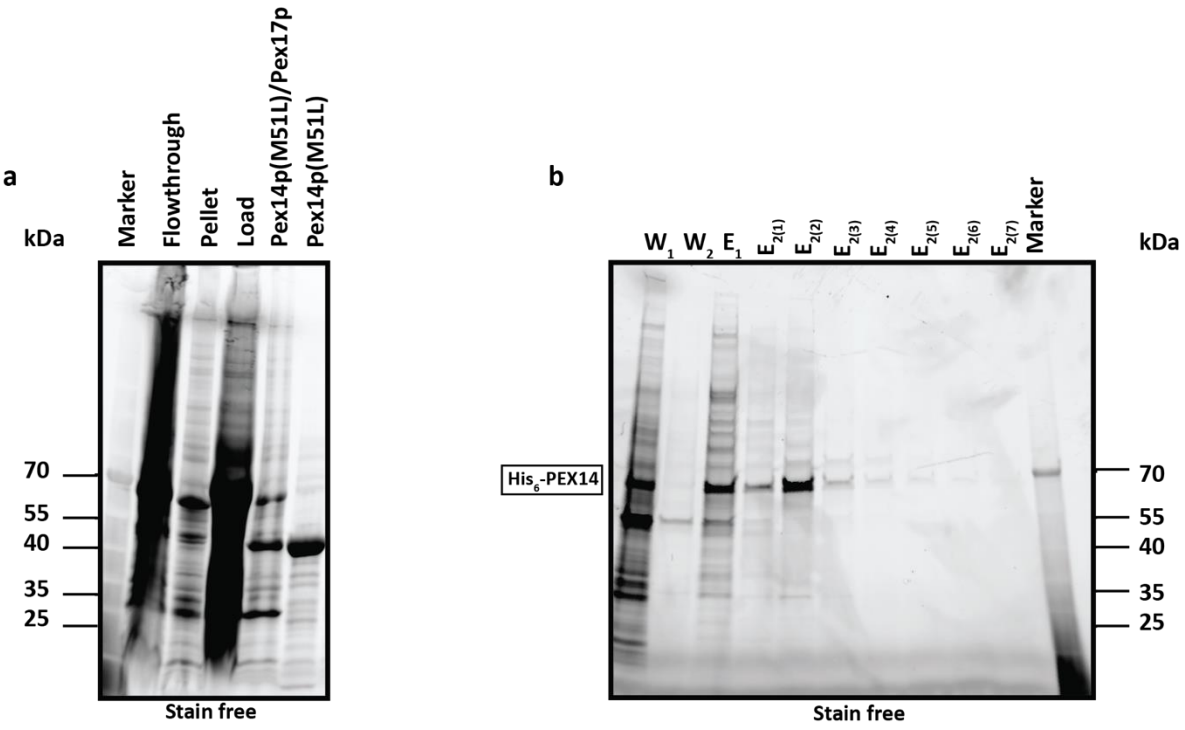

Figure (27): **SDS-PAGE analysis of His_6-PEX14 expression.**

a) Stain free SDS-PAGE of PEX14. Controls.

b) Stain free SDS-PAGE of PEX14. Purification was performed via Ni-NTA in a 0.1% containing Buffer solution. Fractions W_1 - $E_{1(7)}$. The protein band running at 68 kDa corresponds to PEX14. Also, another protein band running at 110 kDa is speculated to represent a PEX14 dimer.

E_1: An elution step of 10 ml with 100 mM imidazole took place in order to remove His-tagged undesired protein-molecules coming from insect cells.

$E_{1(1)}$-$E_{1(7)}$: Elution steps of 2 ml with 250 mM Imidazole in order to collect high-purity PEX14 fractions

.

resulting pellets were consequently resuspended in a 1% DDM containing buffer (**Table (6)**), in order to solubilize the transmembrane protein PEX14, and combined prior lysis. Lysis was performed according to section (**3.2.1**). Supernatant was then collected and applied on a Ni-NTA chromatography affinity column. Buffer solution used for the purification step had a concentration of 0.1% DDM (**Table (6)**).

According to the SDS-PAGE analysis, (**Figure (27)**), among the elution fractions $E_{2(1)}$-$E_{2(4)}$ there are two protein bands running at 68 kDa and 110 kDa. The second band is really weak; and for this reason it is suggested that it corresponds to an impurity.
Size exclusion chromatography was performed using a Superose 6 increase 5/150 GE column. The column was pre-equilibrated in a 0.1% DDM containing TBS buffer in order to keep PEX14 soluble in solution.
The chromatograms' profile (**Figure (28.a)**), displayed a monodisperse peak at the elution volume of 1.25 – 2.5 ml, a sharp peak appears. SDS-PAGE analysis showed a protein band running at the height of 68 kDa which corresponds well to the molecular weight of PEX14. In both stain free (**Figure (28.b)**) and Coomassie stain (**Figure (28.c)**) the second band running at 110 kDa, is still visible. However, in the gel filtration profile, a second peak is absent, suggesting that the existence of possible dimeric oligomerization states in solution is in a rather low abundance.

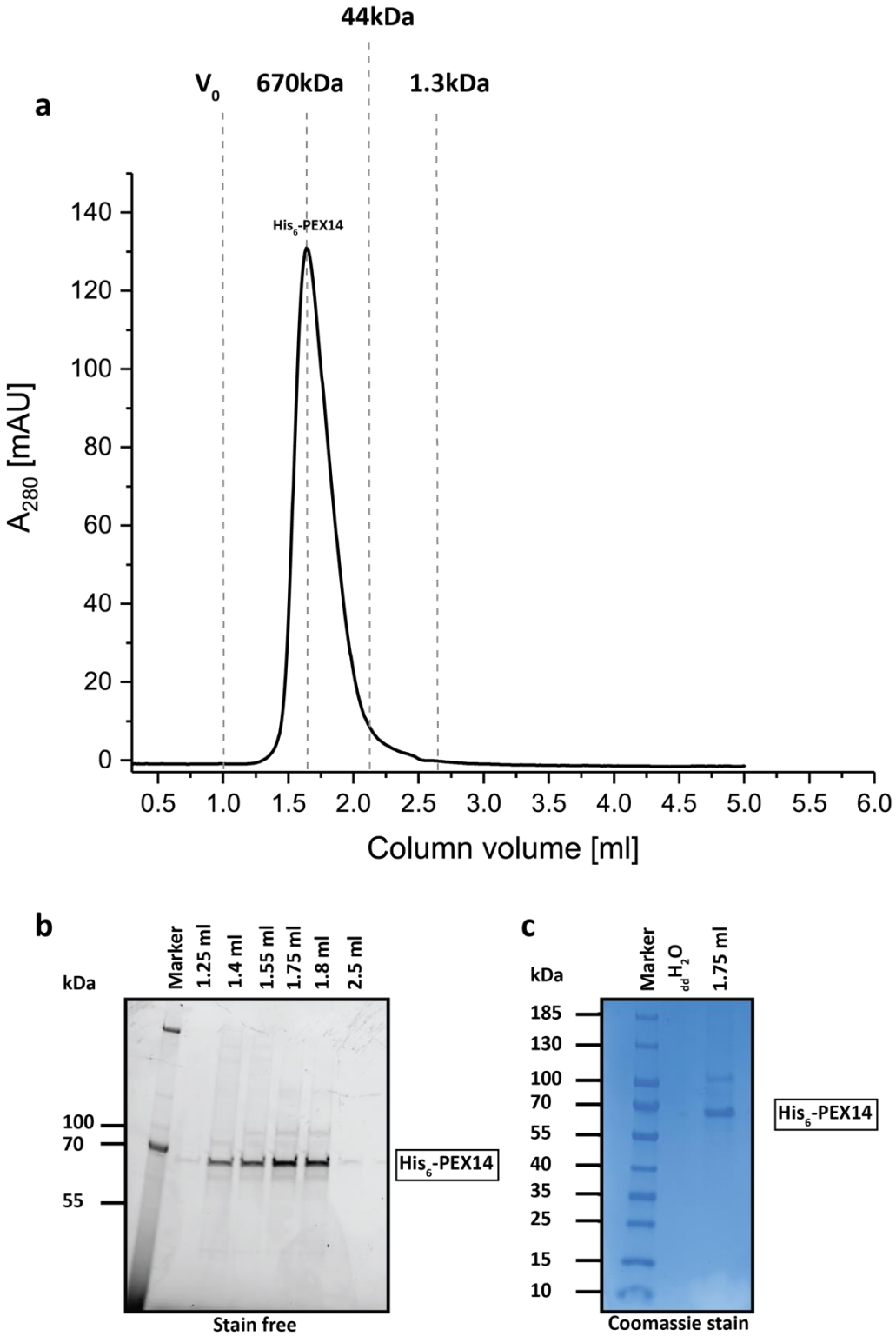

Figure (28): Size exclusion chromatography of His_6-PEX14 and SDS-PAGE analysis of the collected fractions.

a) Chromatogram of Superose 6 Increase 5/150 GE column of His_6-PEX14. The peak eluting at 1.25 – 2.5 ml corresponds to PEX14.

b) Stain - free SDS-PAGE of 80µl fractions of the SEC purification. Protein bands running at 68 kDa correspond to PEX14. Moreover, protein bands visible at the height of 11- kDa are suggested to be a dimer population of PEX14.

c) Coomassie stain of the 1.75 ml fraction.

Dashed lines represent the BioRad protein standard (#1511901).

4.2.2 Negative stain analysis of PEX14

After expressing and purifying PEX14, the next step was to further characterize the protein sample with negative stain microscopy. The fraction of 1.75 ml of the chromatogram, shown in **Figure (28),** was further analyzed with negative stain electron microscopy (**Figure (29)**).

Negative stain grids containing PEX14, were washed 6 times with 10 µl droplets of $_{dd}H_2O$. This approach made sure that excess of DDM was washed away, resulting in a more appropriate background for protein screening.

226 micrographs were recorded on a JEOL JEM 1400 at a nominal magnification of 60.000x corresponding to a pixel-size of 1.84Å/pixel.

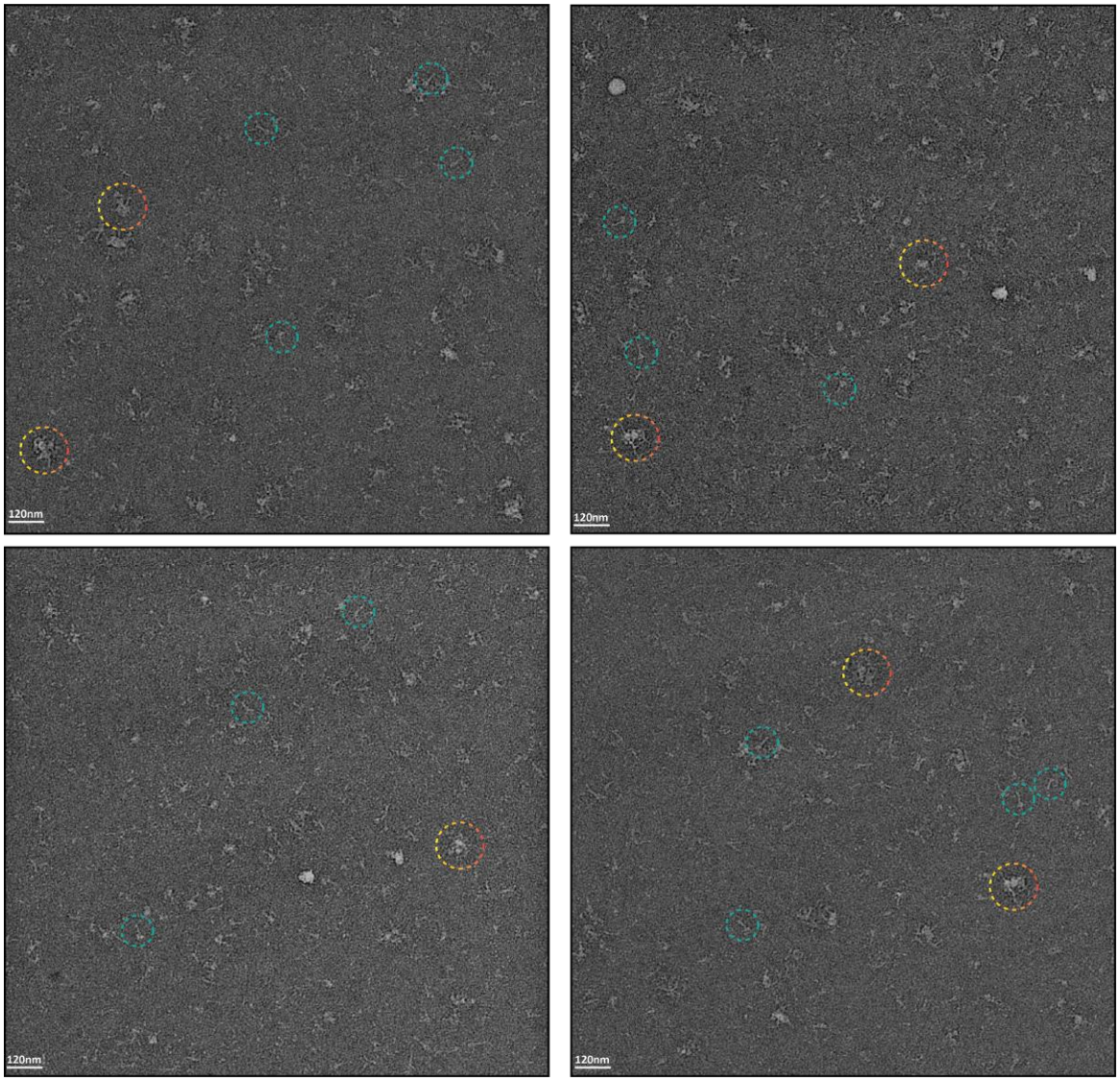

Figure (29): Close up look of negative stain micrographs of His_6-PEX14. (scale bar is 120 nm). In all four micrograph-parts, a wide variety of particles are detectable. With orange-red dotted circles aggregates are indicated, while with cyan dotted circles protein particles of His_6-PEX14 (only a few exemplary particles) with a rod-shaped filamentous structure is shown, resembling $Strep_{II}$-Pex14p(M51L) studied in section (**4.1.3**).

The negative stain screening revealed that the quality of the protein sample was rather not sufficient for further EM studies, since a monodisperse population of particles was not detected. However, in the micrographs, in addition to larger aggregates, several rod-shaped molecules were detected resembling Pex14p(M51L) molecules (cyan indications **Figure (29)**). Additionally, detergent micelles were also formed around the transmembrane region of PEX14, exhibiting even more similarities with the particles of the yeast homolog (**Figure (23)**).
In spite of the sample not being optimal, PEX14 was nevertheless reconstituted into cMSP1D1Δ4-6 lipid nanodiscs. Nanodisc reconstitution was performed according to the following conditions summarized in **Table (13)** below:

Table (13): **His_6-PEX14 reconstitution into cMSP1D1Δ4-6**

	Molarity	**Volume used**
His_6-PEX14	440 mM	87,7 µl
DDM (0.1%)	689.83 mM	2,5 µl
cMSPD1Δ4-6	20 mM	45 µl
Lipids (POPC)	50 mM	2,25 µl
Cholate Buffer	50 mM	112,55 µl
Total Volume	-	250 µl

The mixture was incubated for 12 hours at 4 °C. Next, detergent removal was performed by placing the solution in a new reaction-tube containing 250 mg of SM-2® Bio-Beads, followed by a three-hour incubation in 4°C.
Afterwards, Bio-Beads were discarded and the assembled PEX14-ND complex was separated from empty ND and excess lipids by size exclusion chromatography using a Superose 6 increase 5/150 GE column pre-equilibrated in TBS Buffer (**Figure (30)**).

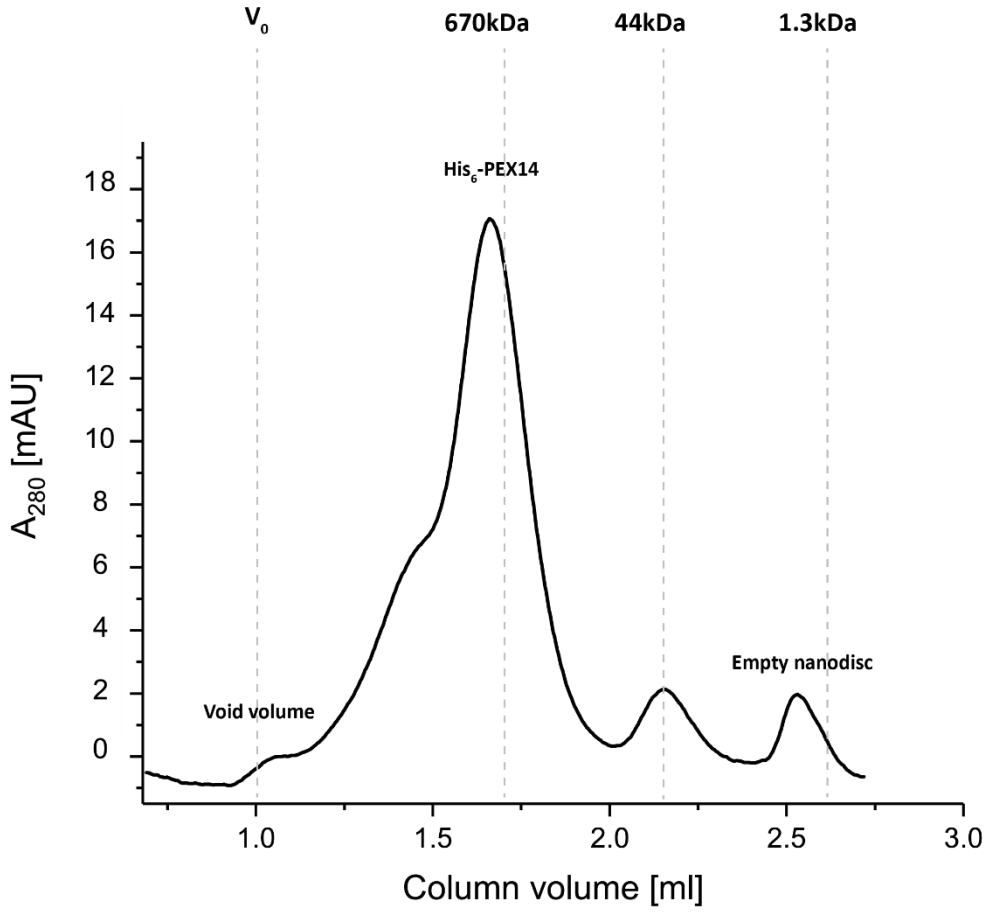

Figure (30): Chromatogram of Superose 6 Increase 5/150 GE column of His_6-PEX14 reconstituted into cMSP1D1Δ4-6 lipid nanodiscs.

The main peak coming at 1.25 – 1.9 ml corresponds to the PEX14-ND assembly. However, a shoulder appears at 1.25 – 1.5 ml that is suggested to represent an insertion of a dimer PEX14 population to the lipid-ND.

Dashed lines represent the BioRad protein standard (#1511901).

The chromatogram represented a low void volume peak, a broad sample peak and corresponding peaks for empty nanodiscs. At an elution volume of 1 ml, the void volume was observed, including the aggregates of PEX14 and the excess of lipids.

The main peak of the SEC profile elutes broad with a range of 1.25 ml – 1.9 ml. The main fraction was collected at around 1.6 ml according to the previous obtained data with yeast Pex14p. The shoulder at around 1.5 ml possibly represents reconstitution of two PEX14 copies into a single circular nanodisc. At 2.5 ml the empty nanodisc peak is detected.

4.2.3 Negative stain analysis of PEX14 reconstituted to lipid nanodiscs

The fraction of 1.7ml on the gel filtration shown in **Figure (30)** was analyzed further by negative stain electron microscopy (**Figure (31)**), for assessing whether nanodisc incorporation was successful or not.

Dataset acquisition was performed with JEOL and 226 images were recorded in a nominal magnification of 60.000x corresponding to a pixel-size of 1.84Å/pixel.

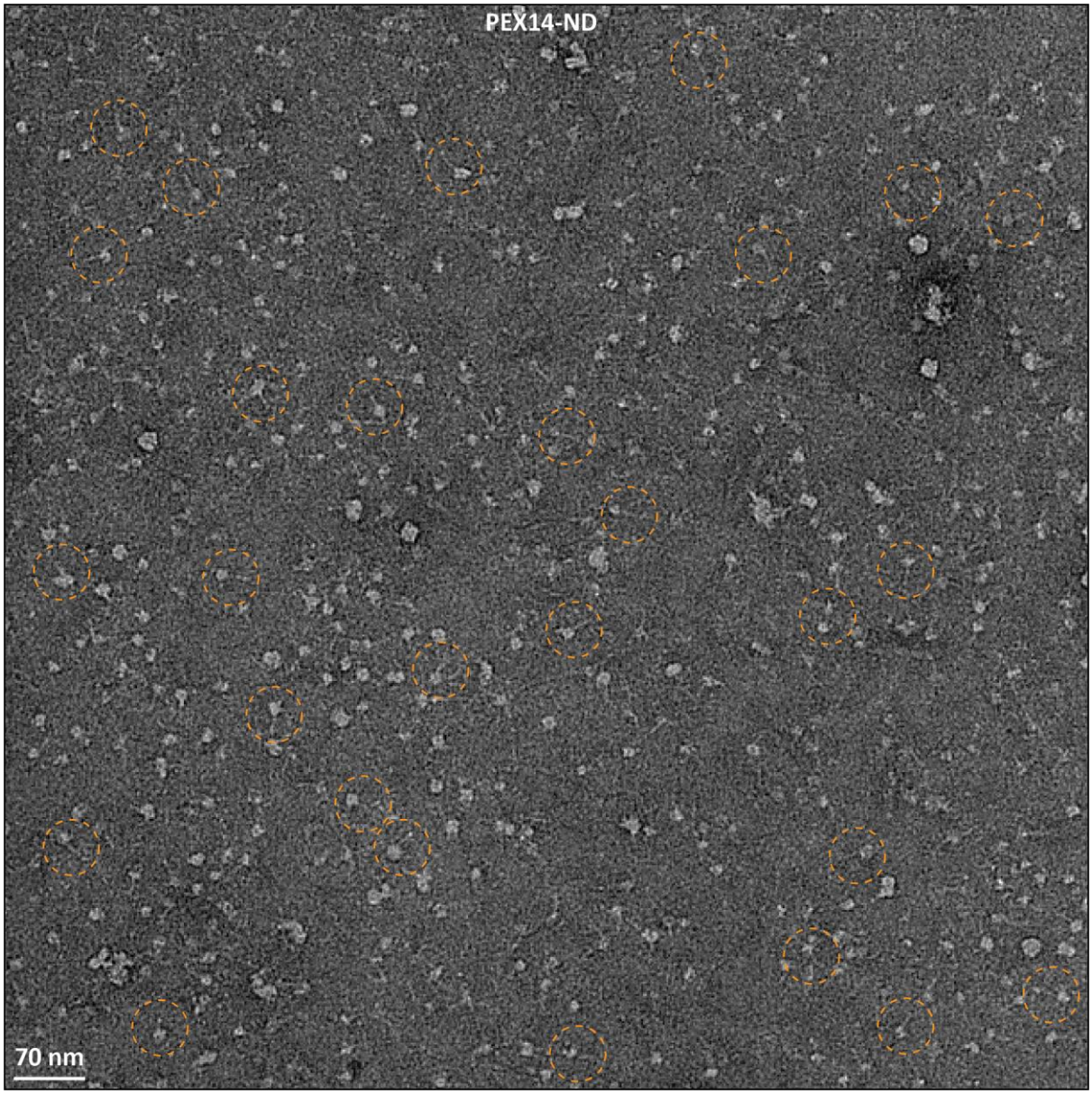

Figure (31): Negative stain micrograph of His_6-PEX14 after being reconstituted into cMS1P1DΔ4-6 lipid nanodiscs. (scale bar is 70nm).

a) Negative stain micrograph of His_6-PEX14 reconstituted into cMSP1D1Δ4-6 lipid nanodiscs.

b) With orange dotted circles, examples of the proteo-nanodisc containing His_6-PEX14 are indicated.

The reconstituted protein particles are similar to the previous reconstitution assemblies of the yeast homologues.

In total 52.346 particles of PEX14 were extracted, aligned and classified using ISAC as implemented in the SPHIRE software package.

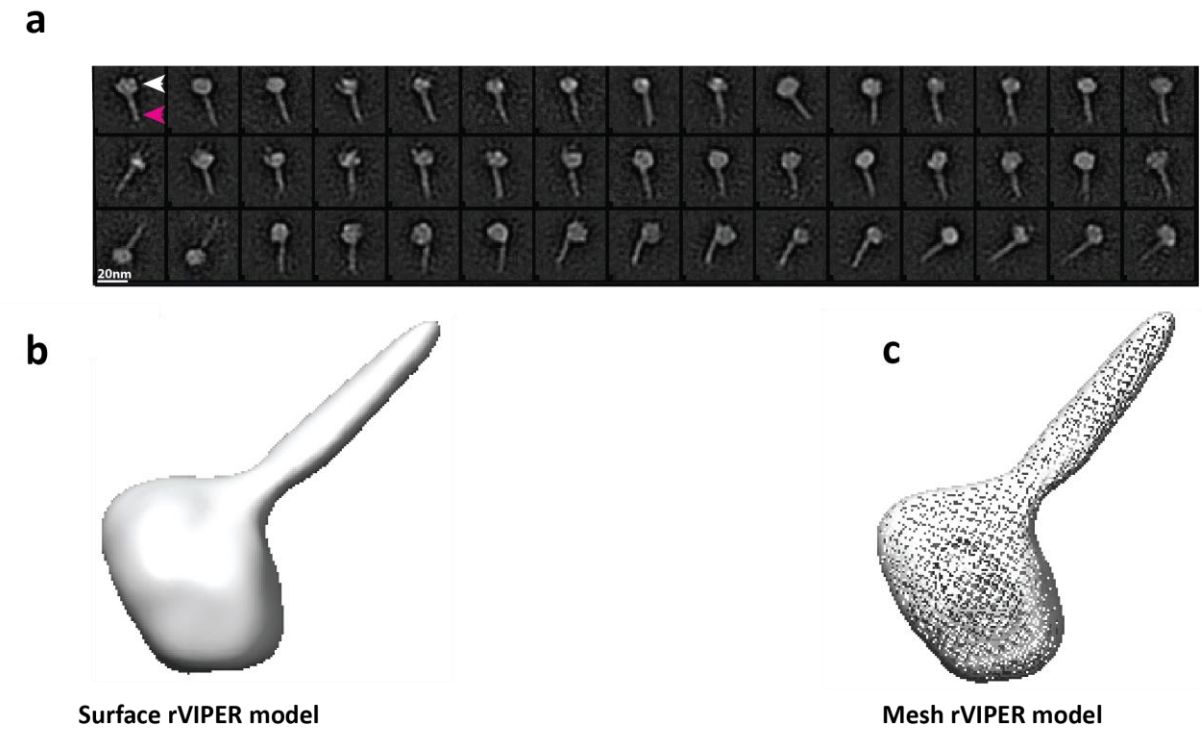

Figure (32): Exemplary class averages of negative stained His_6-PEX14 after being reconstituted into cMSP1D1Δ4-6 lipid nanodiscs. (scale bar is 20nm).

a) 2D classes of His_6-PEX14 reconstituted into cMSP1D1Δ4-6 ND. With the white arrowhead the lipid ND is indicated while with the hot-pink arrowhead His_6-PEX14 is shown.

b) Using Chimera, a surface rVIPER schematic illustration depicts a 20 Å His_6-PEX14 reconstruction model.

c) Using Chimera, a mesh rVIPER schematic illustration depicts a 20 Å His_6-PEX14 reconstruction model.

The class averages confirm successful reconstitution of PEX14 into cMSPs. At first glance, classes showed an elongated rod shaped structure with a bulky region similar to the yeast Pex14p or Pex14p/Pex17p complex (**Figure (32.a)**). The predicted coiled coil region (pink arrowhead), filaments are protruding from the lipid ND (white arrowhead) that appears as a bulky region.

The elongated rod shaped particle, is variable in length (18 – 24 nm). Notably, the yeast complex of Pex14p/Pex17p had a similar size variation, whereas Pex14p, alone, appeared rather smaller.

Afterwards, classes were sorted in order to obtain a homogeneous dataset with regard to size distribution and an ab initio model was calculated using VIPER (**Figure (32.b.c)**). The ab initio model from VIPER, displays PEX14 as a rod-shaped filament protruding from the lipid ND. However, the rod seems to be flattened, due to the preferred orientation of the particle on the

grid. The resolution of negative stain is limited for a particle of this size; however, the quality of the sample is now suitable for cryo-EM analysis

4.2.4 Cryo-EM analysis of PEX14 reconstituted into cMSP1D1Δ4-6 lipid nanodiscs

For cryo-EM of PEX14 reconstituted into lipid nanodiscs, Quantifoil 1.2 / 1.3 grids were first glow discharged. Plunging was performed using a Vitrobot Mark II. 4µl of 0.3 mg/ml of the PEX14-ND proteo-lipid solution was applied under 100% humidity at 8 °C to the grids, followed by a subsequent blotting process by applying -3 force. Vitrification was then performed by plunging the grid in liquid ethane.

Screening of the grids using a FEI TALOS ARTICA microscope, revealed a gradient with regard to ice thickness (**Figure (33)**). Therefore, a different range of ice layered squares with most optimal ice thickness were selected, in order to identify the optimal positions for visualization of the PEX14-ND particles. A typical square is shown in **Figure (33.b)**. However, the PEX14-ND complex was only visible in holes embedded with a rather medium-ice thickness layer.

Since the contrast was low, particles were barely visible. Nevertheless, the present study provides a good starting point for future cryo-EM studies of PEX14, which will however require extensive optimization of the vitrification conditions.

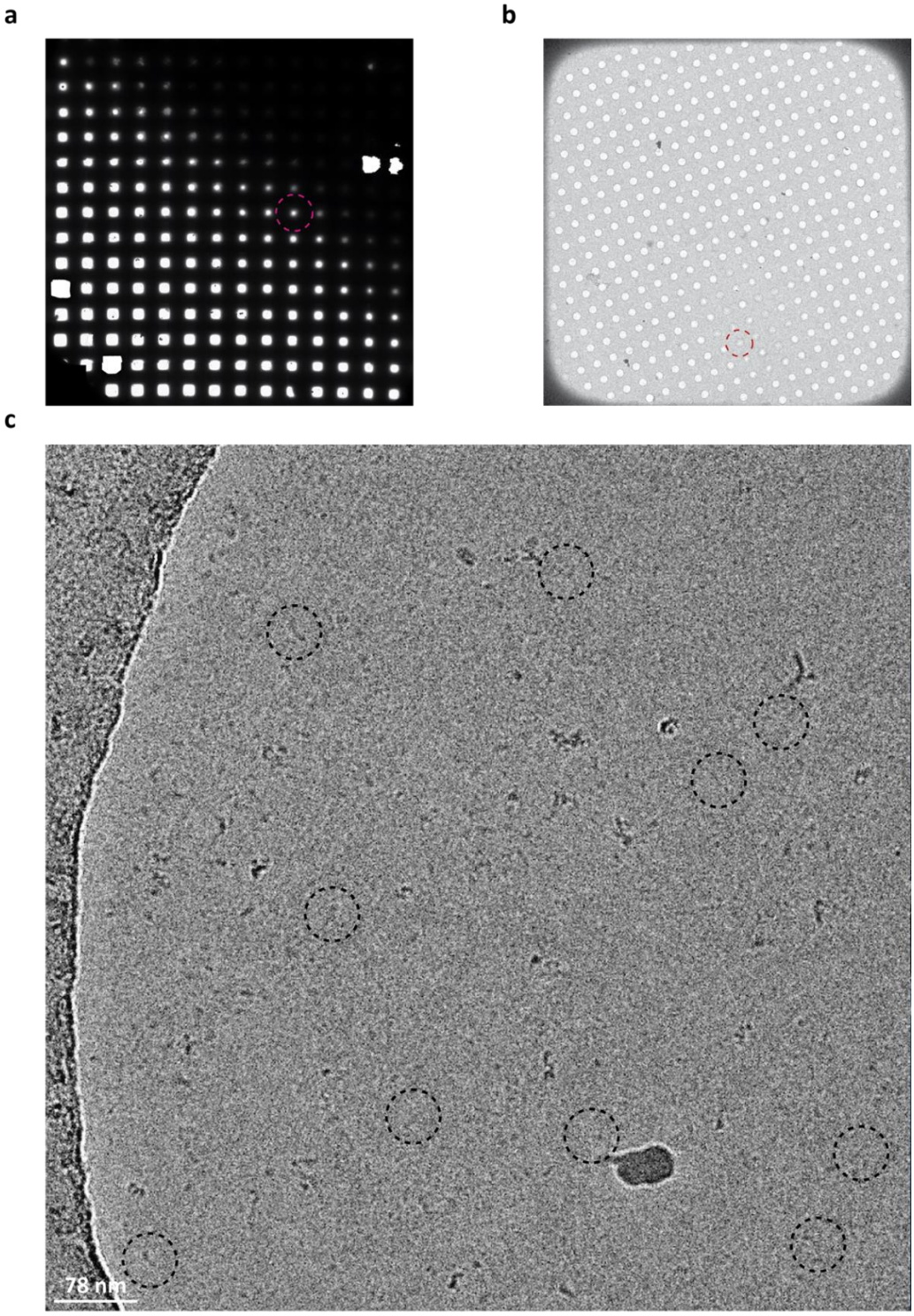

<u>Figure (33):</u> ATLAS, hole image and cryo-EM micrograph of His_6-PEX14 after reconstitution to cMSP1D1Δ4-6 lipid nanodiscs (scale bar is 78nm).

a) Collected ATLAS from a complete screening of the entire Quantifoil 1.2 grid surface. Ice thickness gradient is evident form bottom left to top right (thin – thick). With a hot-pink circle is the grid square selected for screening.

b) Image of selected square from (a) representing the holes that the sample resides. With a red dotted circle, the selected hole is highlighted once again. (preferred medium thickness ice layer)

c) Cryo-EM micrograph of the selected hole from (b). His_6-PEX14 particles are barely visible in the micrograph and some examples are shown within red-dotted circles.

4.3 Pore formation studies

As described already in the introduction (chapter (**1.2**)), several studies suggest that yeast Pex14p/Pex17p (docking complex) combined with Pex5p (cargo protein receptor) are comprising the importomer and that only these three peroxins constitute the minimal functional peroxisomal pore (Ma et al. 2009). Towards the visualization of the pore, we first focused on a complex formed by the docking complex and the receptor protein, in absence of cargo. We also visualized the receptor alone, using negative stain EM, to clarify if Pex5p is forming a monomeric complex under negative stain conditions.

To provide a close to native membrane environment, liposomes were formed decorated with the Pex14p/Pex17p docking complex. Finally, Pex5p was added to the reconstituted Pex14p/Pex17p complex, to visualize the effect of receptor binding on the structure of the docking complex.

Moreover, we also reconstituted the docking complex, together with Pex5p in cMSP1D1Δ4-6 lipid nanodiscs, for subsequent single particle studies of the receptor/docking-complex assembly.

4.3.1 His_6-Pex5p negative stain analysis

Pex5p, is the receptor protein and suggested as the main protagonist in the peroxisomal import. The peroxin has a molecular weight of 69.3 kDa and is reported to form dimers, trimers, tetramers and even higher oligomeric states in solution (Ma et al. 2013).

Purification of His_6-Pex5p was performed here, using a Superose 6 Increase 5/150 GE column pre-equilibrated in TBS Buffer **Figure (34.a)**.

The main peak of the chromatogram elutes at the volume of 1.5 ml to 2.4ml. The peak displayed a shoulder at an alution volume of 1.6 ml. However, SDS-PAGE analysis (**Figure (35.b)**) showed that only Pex5p was present in the elution volume of, 1.5 ml to 2.4 ml. This leads to the suggestion that the shoulder peak might represent higher oligomeric forms of Pex5p.

Main fractions of the corresponding elution volume of 2.3 ml and 1.6 ml were dilluted to a concentration of 0.03mg/ml. Negative stain grids were prepared by washing the grids three times with 4 µl of TBS buffer. instead of $_{dd}H_2O$ was required for optimal negative stain screening. Grids were then screened using the JEOL JEM 1400 with a magnification of 80.000x and a corresponding pixel size of 1.3Å/pixel.

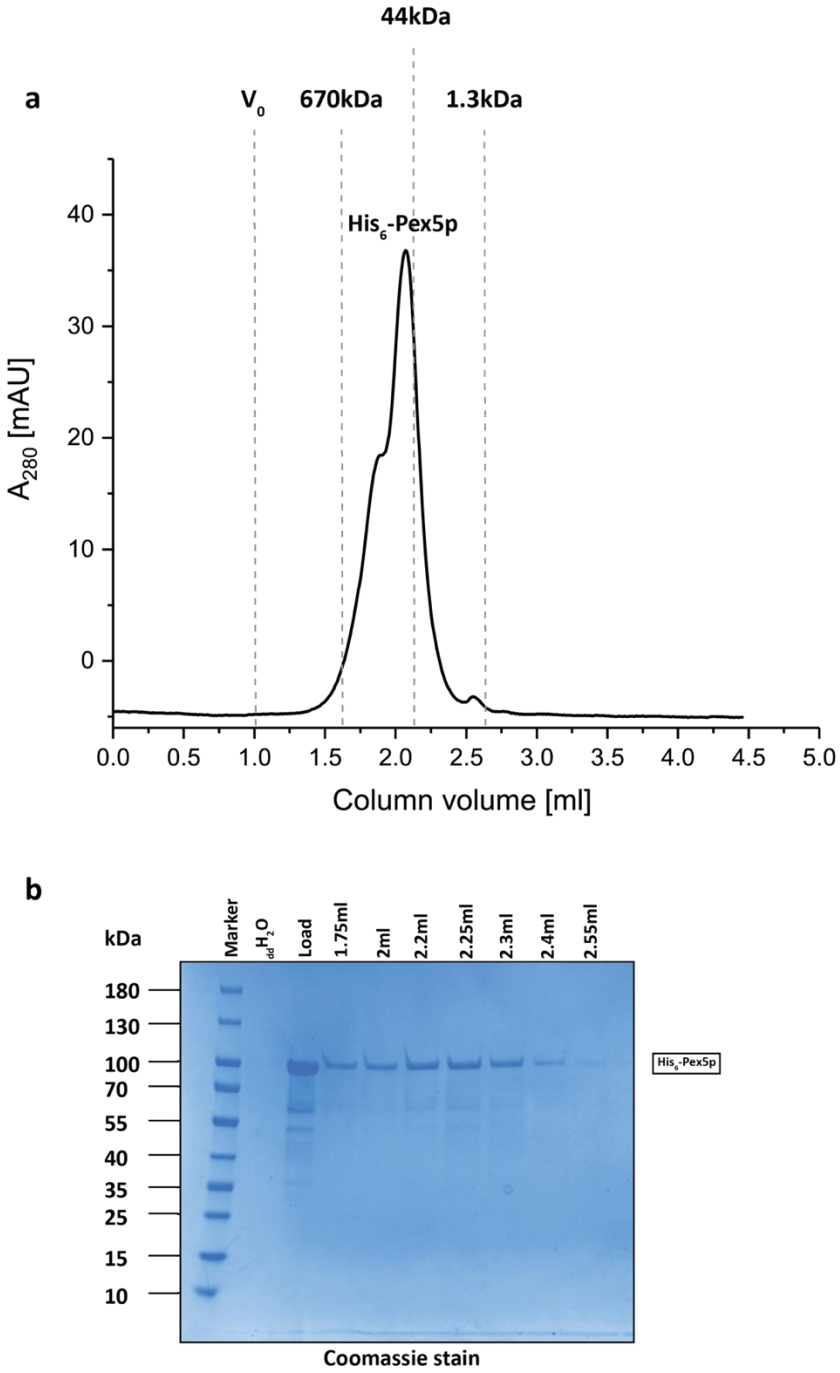

Figure (34): Size exclusion chromatography of His_6-Pex5p and SDS-PAGE analysis of the collected fractions.

a) Chromatogram of Superose 6 Increase 5/150 GE column of His_6-Pex5p. The peak corresponding to Pex5p elutes at 1.5 – 2.4 ml. Also, a shoulder is visible at 1.5 – 1.8 ml, suggesting that high-oligomeric populations of Pex5p exist in solution.

b) Coomassie stain SDS-PAGE of 80µl fractions of the SEC purification. Protein bands running at 100 kDa, correspond to Pex5p

Dashed lines represent the BioRad protein standard (#1511901).

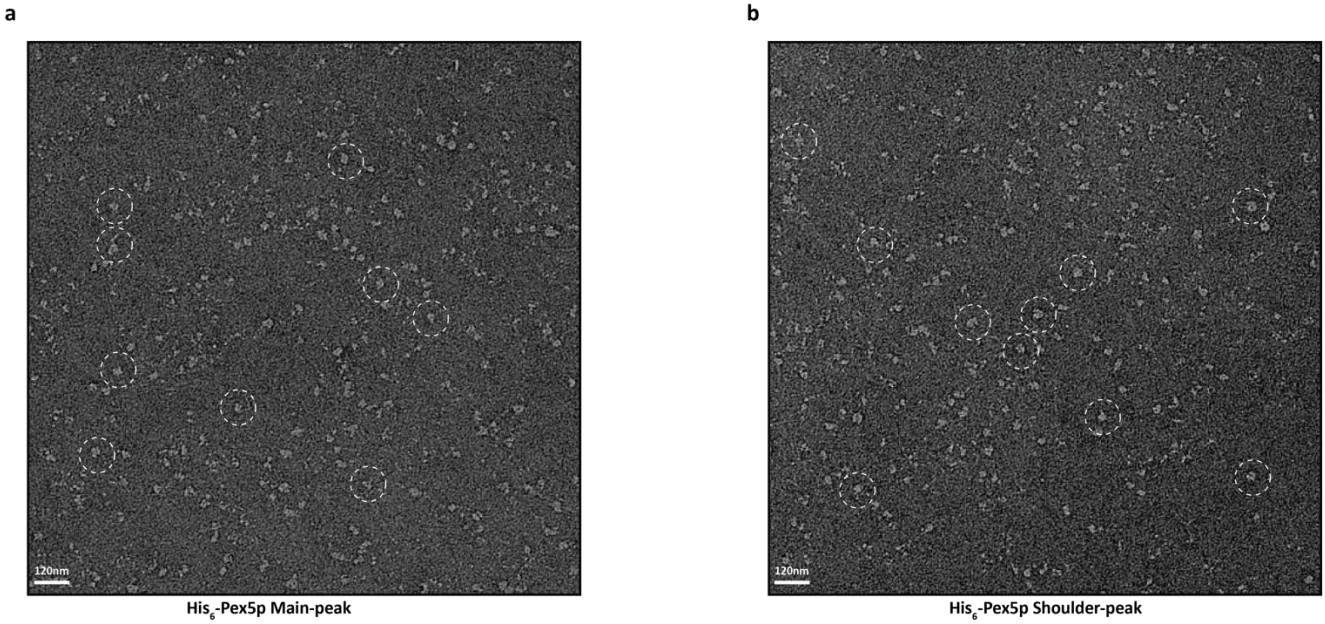

Figure (35): Negative stain screening micrographs of His_6-Pex5p. (scale bar is 120nm).

a) Negative stain micrograph of the main peak of His_6-Pex5p size exclusion chromatogram.

b) Negative stain micrograph of the shoulder peak of His_6-Pex5p size exclusion chromatogram.

In both cases exemplary particles of His_6-Pex5p are highlighted with white dotted circles.

Both fractions showed under negative stain conditions similar populations of particles. This finding suggests that a small population of Pex5p might elute earlier due to its flexible N-terminus which might induce a different PI value. Moreover, oligomerization of Pex5p might rather be induced at higher pH or concentration of the protein.

A dataset of 112 micrographs of the main peak was collected, using once again the JEOL JEM 1400 electron microscope. In total 18.324 particles of Pex5p were extracted, aligned and classified using the SPHIRE software package (**Figure (36)**).

The 2D classification revealed that the sample is homogeneous and includes different populations of particles and possibly different oligomeric states of Pex5p (**Figure (36.b-e)**.

Several classes show a central core with additional extensions, that might indicate the C-terminal and N-terminal domains of Pex5p (discussed in section **(1.2.1)**). We interpret these results as such the TPR domain (pink arrowhead) appears with a bulky-globular conformation, while the disordered N-terminal domain (cyan arrowhead) is distinguished as a thin filament protruding from the TPR. The N-terminus domain is visible in only a few of these 2D classes. This occurs because the N-terminus is unstructured and extremely flexible and might bend

relative to the helical TPR domain and thus averaged out by the classification process of ISAC.

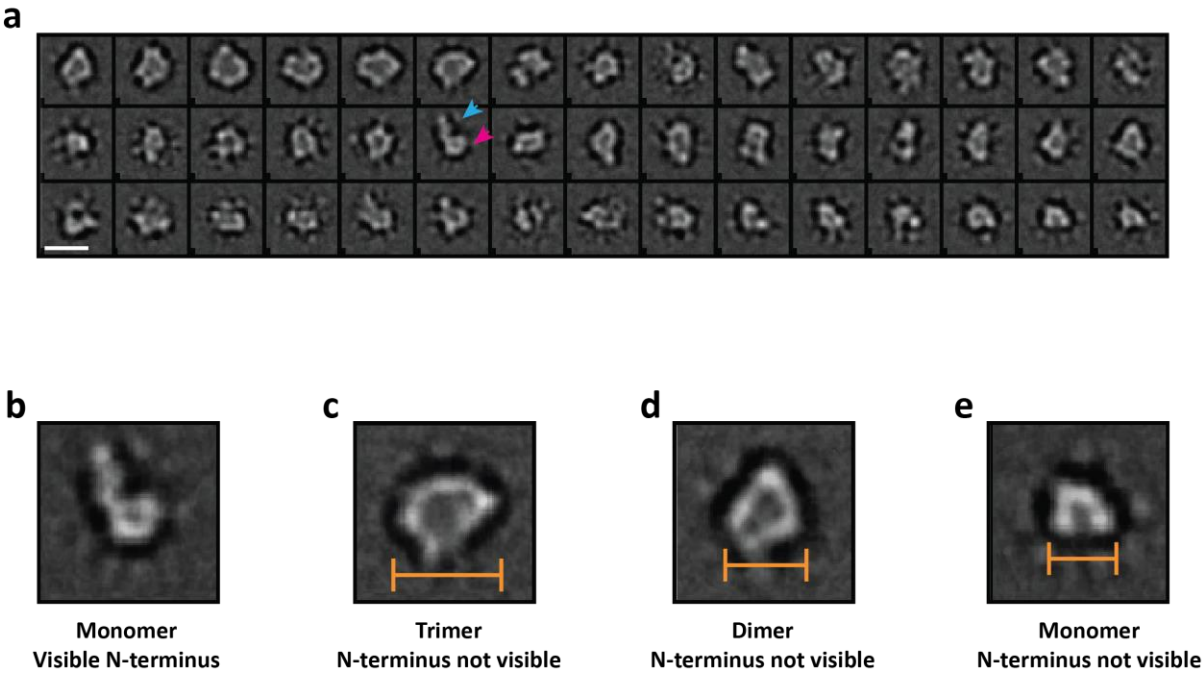

Figure (36): **Exemplary class averages of negative stained His_6-Pex5p (scale bar is 14nm).**
Based on the 2D-class averages, it seems that different oligomeric states of Pex5p exist in solution.
a) 2D classes of His_6-Pex5p.
b) Monomer 2D class example of Pex5p where the N-terminus is visible as a really thin filament.
c) Trimer 2D class example of Pex5p where the N-terminus is not visible. (scale bar is 18)
d) Dimer 2D class example of Pex5p where the N-terminus is not visible. (scale bat is 14 nm)
e) Monomer 2D class example of Pex5p where the N-terminus is not visible. (scale bat is 10 nm)

4.3.2 Nanodisc reconstitution of Pex5p

Since Pex5p is considered as a major key player for the formation of the transient pore at the peroxisomal membrane, incorporation of the protein into cMSPD1Δ4-6 lipid nanodiscs was attempted. Therefore, nanodisc reconstitution was performed according to the following conditions summarized in **Table (14)** below:

Table (14): **His_6-Pex5p reconstitution into cMSP1D1Δ4-6**

	Molarity	Volume used
His_6-Pex5p	440 mM	62,5 µl
DDM (0.1%)	689.83 mM	2,5 µl
cMSP1D1Δ4-6	20 mM	45 µl
Lipids (POPC)	50 mM	2,25 µl
Cholate Buffer	50 mM	137,75 µl
Total Volume	-	250 µl

Solution containing all necessary ingredients was incubated overnight at 4 °C. The solution was then placed in a reaction-tube containing 250 mg of SM-2® Bio-Beads. Detergent was removed by incubation of the sample with 250 mg of SM-2 Biobeads for three hours at 4 °C. Bio-Beads were discarded and the assembled Pex5p-ND complex was separated from empty ND and excess lipids by size exclusion chromatography using a Superose 6 increase 5/150 GE column pre-equilibrated in TBS Buffer (**Figure (37.a)**).

The main peak of the SEC profile elutes in the range of 1.75 ml – 2.4 ml shows a monodisperse elution profile. SDS-PAGE analysis (**Figure (37.b)**), showed corresponding bands for Pex5p (100kDa) and the cMSP (12kDa) at the same elution fraction, suggesting a successful incorporation of Pex5p.

At 2.5 ml the empty nanodisc peak is detected. Also, at 1 ml there seems to be also a small void volume peak.

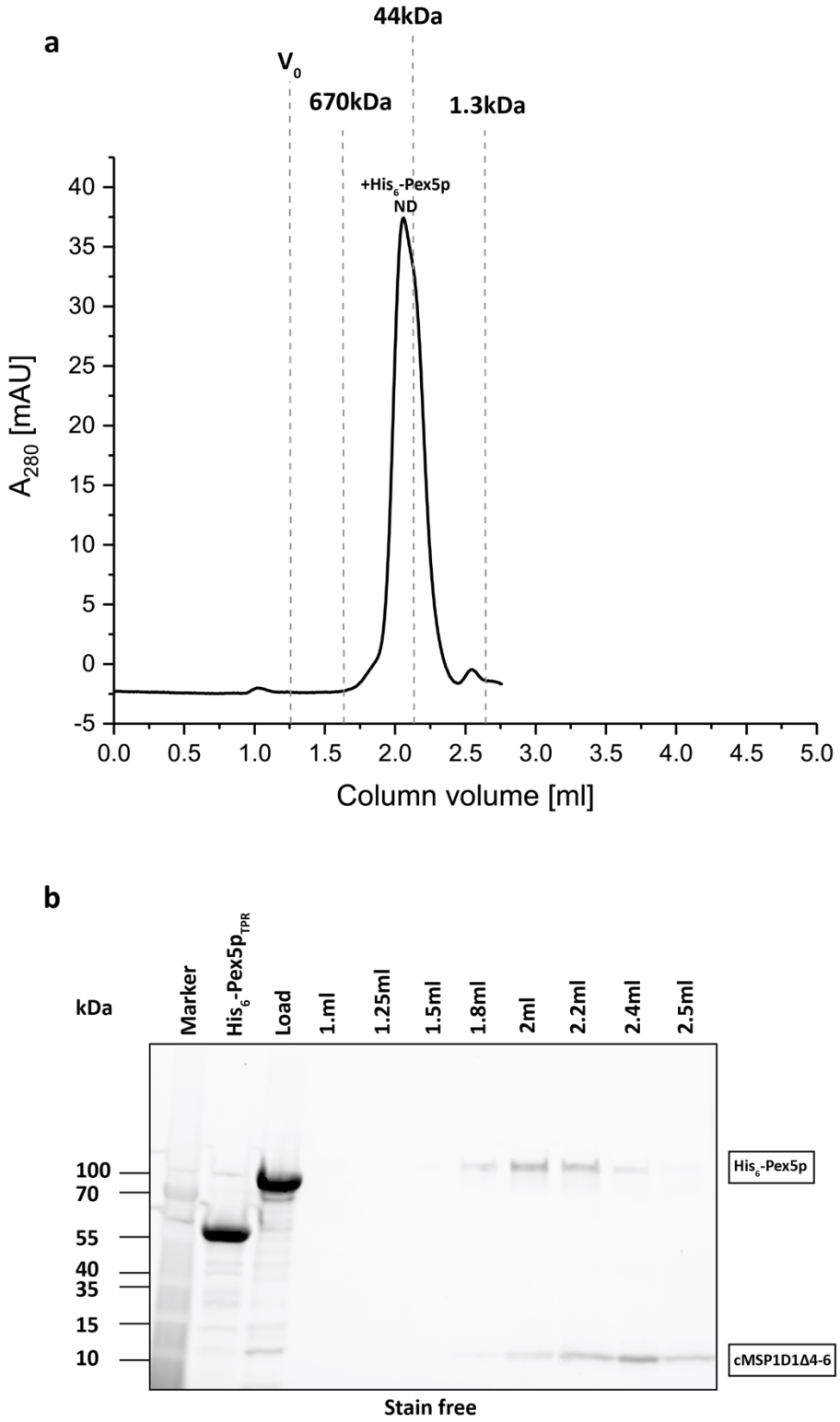

Figure (37): Size exclusion chromatography of His_6-Pex5p after reconstitution to cMSP1D1Δ4-6 lipid ND and SDS-PAGE analysis of the collected fractions.

a) Chromatogram of Superose 6 Increase 5/150 GE column of His_6-Pex5p reconstituted to lipid ND. The main peak eluting at 1.75 – 2.4 ml corresponds to the Pex5p-ND assembly. Small peaks observed at 1 ml and 2.5 ml represent the void volume and the empty ND accordingly.

b) Stain free SDS-PAGE of 80µl fractions of the SEC purification.

Dashed lines represent the BioRad protein standard (#1511901).

In order to assess if Pex5p incorporation to the cMSP1D1Δ4-6 lipid ND was achieved, the fraction of 1.7 ml of the main peak, shown in **Figure (37.a),** was further analyzed with negative stain electron microscopy (**Figure (38.a)**). Thereafter, grids were glow discharged and screened with JEOL JEM 1400 microscope at nominal magnification of 60.000x that corresponds to a pixel-size of 1.84Å/pixel

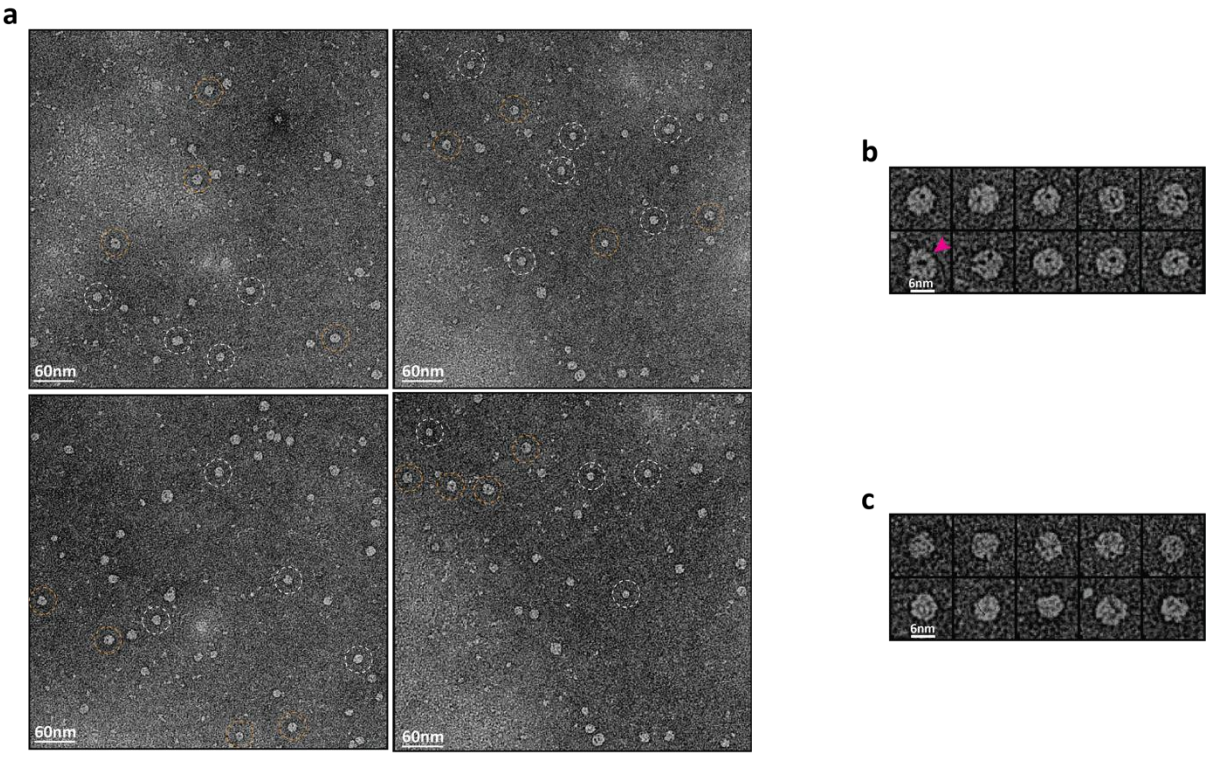

Figure (38): **Negative stain micrograph of His_6-Pex5p after reconstitution to cMSP1D1Δ4-6 lipid nanodiscs (scale bar is 60 nm).**

a) Negative stain micrographs of His_6-Pex5p reconstituted into cMSP1D1Δ4-6 lipid ND. With white dotted empty ND are indicated while with orange dotted circles ND carrying a dark dot resembling an opening in their periphery are pointed.

b) Examples of the nanodiscs possessing, the what looks to be, a pore formation in the lipid nanodisc periphery. With a hot-pink arrowhead the black dot is indicated.

c) Examples of lipid nanodiscs where there is no effect caused by His_6-Pex5p.

Negative stain analysis displays that the obtained, particles can be distinguished in empty NDs and a ND assembly with a density resembling a hole in the middle. Pex5p particles are not visualized as an additional density. Therefore, negative stain EM did not provide enough information regarding Pex5p reconstitution.

4.3.3 Importomer studies

4.3.3.1 Liposome formation - $Strep_{II}$-Pex14p(M51L)/His_6Pex17p decoration

After elucidating the characteristic and the possible effect on membrane environments of Pex5p, investigations have been made in the assembly of the docking complex together with the receptor Pex5p.

Therefore, liposome-formation conditions were extensively screened. First of all, liposomes were formed and extruded. Here, the size of the liposomes was controlled by applying the lipid-solution in a filter. However, after filtration, the resulting liposomes were not decorated with the peroxins (**Figure 39.f-g)**).

For that reason, we tried to form liposomes by removing the detergent using Bio-Beads instead. Here, different volumes of protein solution, lipids and concentrations of Bio-Beads were screened.

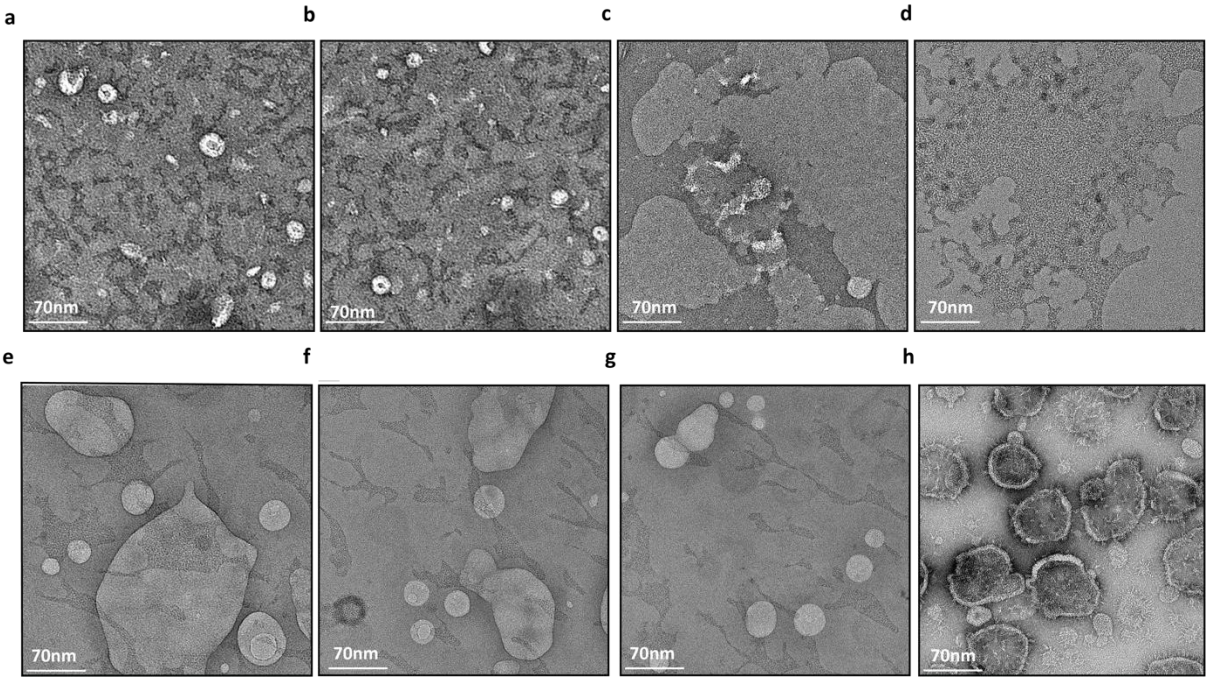

Figure (39): Failed attempts to create $Strep_{II}$-Pex14p(M51L)/His_6Pex17p decorated liposomes. (scale bar is 70 nm).

Micrographs of negative stain microscopy, highlighting the failed attempts to decorate liposome periphery with the Pex14p/Pex17p complex.

a) Result of liposome formation after using too few Bio-Beads.

b) Result of liposome formation after using too much Bio-Beads.

c) Result of liposome formation without washing Bio-Beads 3 times with TBS solution.

d) Result of liposome formation without performing all the steps at 4˚C.

e, f, g) Result of liposome formation with the extrusion protocol (non - decorated liposomes).

h) Perfectly shaped and decorated liposomes (desired result).

Without activation of Bio-Beads in TBS buffer, liposome formation was impaired. Finally, it was determined that every step regarding the liposome formation handling, had to be performed in 4 ˚C. Otherwise, liposomes aggregated or did not form at all (**Figure (39.a-e)**).

In **Figure (39)**, micrographs of the different liposome formation approaches are displayed and compared with the final optimized liposome formation (**Figure (39.h)**).

For the purpose of liposomes, POPC lipids were selected in order to resemble as much as possible the natural environment of the peroxisomal membrane and therefore provide a more native environment for the Pex14p/Pex17p complex. Therefore, liposome formation was performed according to the following conditions summarized in **Table (15)**.

Negative stain grids were prepared and screened at a magnification of 40.000x with a corresponding pixel-size of 2.8Å/pixel and EM analysis confirmed the formation of homogeneous liposomes. Moreover, the periphery of the liposomes was isotropically decorated with the Pex14p/Pex17p complex (**Figure (40)**).

Table (15): **$Strep_{II}$-Pex14p(M51L)/His_6Pex17p liposome assembly composition mixture**

	Stock	**Molarity**	**Volume**
Buffer TBS	150 mM NaCl, 50 mM Tris pH=8.0 + 0,1% DDM	245.85 mM	430 µl
$Strep_{II}$-Pex14p(M51L)/His_6Pex17p	2 mg/ml	1.5 µM	65.5 µl
POPC lipids	50 mM in 100 mM Cholate	450 µM	4.5 µl
Total Volume	-	-	500 µl

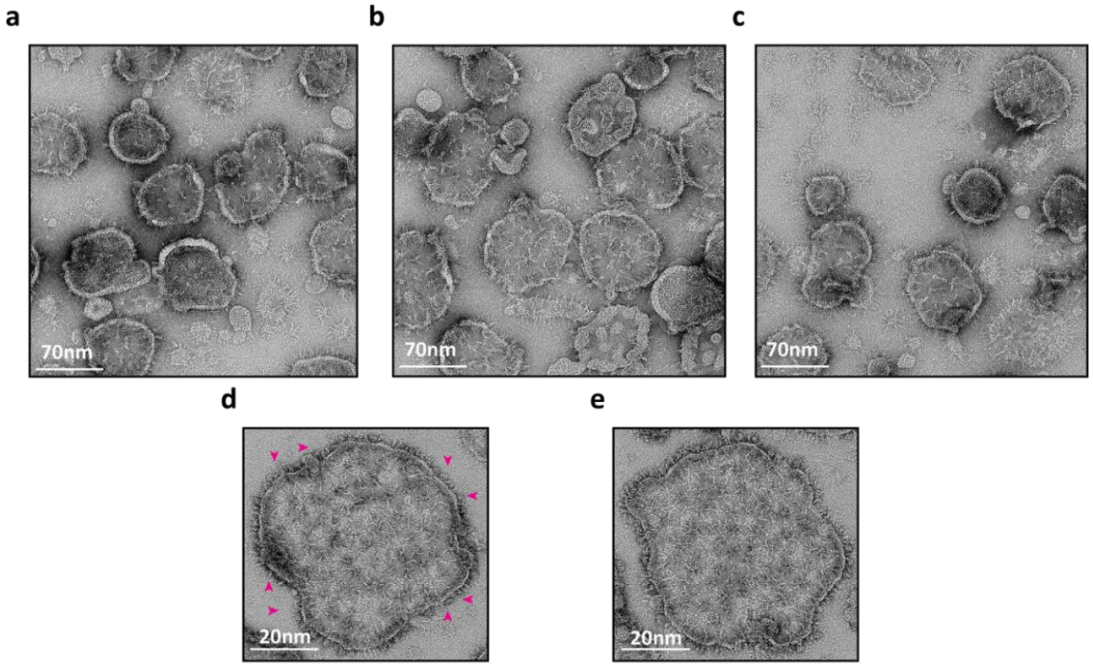

Figure (40): Successful attempts to create $Strep_{II}$-Pex14p(M51L)/His_6Pex17p decorated liposomes (scalebar is 70nm and 20nm).

Negative stain microscopy micrographs depicting successful Pex14p/Pex17p decoration of liposomes' periphery

a, b, c) Result of liposome formation after using the protocol mentioned in **Table (15)**.

d, e) Close up look on liposomes. Membrane of liposomes is decorated with -Pex14p(M51L)/His_6Pex17p.

4.3.3.2 His_6-Pex5p effect to the already formed liposomes

Liposomes were thus assembled and successfully decorated with the docking complex of $Strep_{II}$-Pex14p(M51L)/His-$_6$Pex17p (**Figure (40)**).

As a next step, 0.03mg/ml of Pex5p was added to the already existing liposome assembly exposing the docking complex and samples were screened on a FEI Tecnai Spirit G2

microscope. Images were recorded at a nominal magnification of 42.000x corresponding to a pixel size of 2.6Å/pixel (**Figure (41)**).

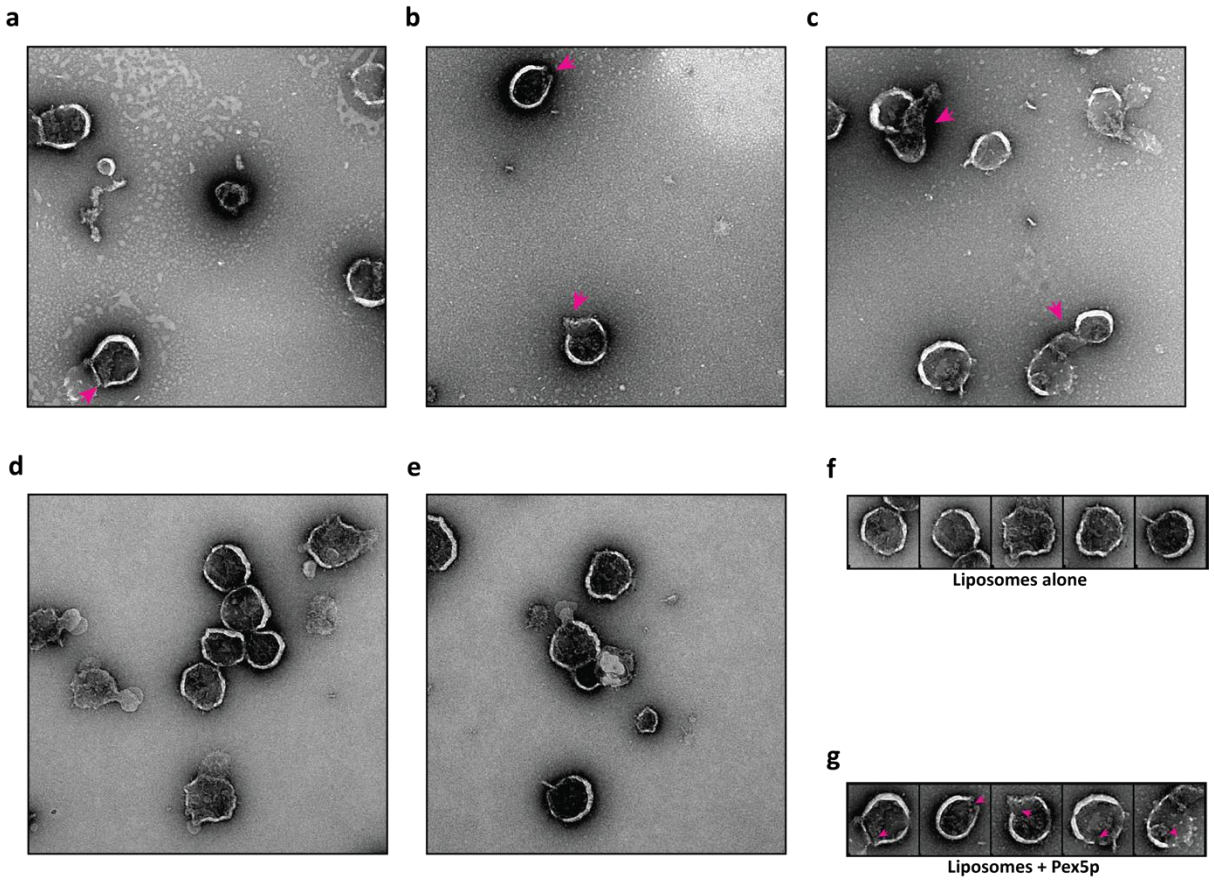

Figure (41): His_6-Pex5p effect on $Strep_{II}$-Pex14p(M51L)/His_6Pex17p decorated liposomes.

Negative stain microscopy micrographs suggesting that in the presence of the cargo-receptor Pex5p a pore forms in the liposomes' membrane.

a, b, c) His_6-Pex5p (+) sample. His_6-Pex5p can be detected as grains in the background. With hot-pink arrowheads, break points in the periphery of the liposomes are indicated.

d, e) Control micrographs of liposomes decorated with $Strep_{II}$-Pex14p(M51L)/His_6Pex17p.

f) Closer look in liposomes decorated with $Strep_{II}$-Pex14p(M51L)/His_6Pex17p.

g) Closer look at the effect caused by the addition of His_6-Pex5p.

The comparison of the liposomes **Figure (41.f)** and **Figure (41.g)** shows that addition of Pex5p did not lead to any characteristic change. However, the membranes of several liposomes appear disrupted. It is however unclear yet, if those are induced by Pex5p, since liposomes often tend to break during negative stain EM experiments. Nevertheless, this study provides a solid foundation for further experiments in this direction.

4.3.4 Pex5p addition to the reconstituted docking complex

In order to achieve the reconstruction of the importomer into cMSPs, the ND assembly protocols from section (**4.1.1**) and (**4.1.5**) were used.

In this section two different approaches will be demonstrated. First Pex5p was added on the $Strep_{II}$-Pex14p(M51L)/His_6-Pex17p-ND and on $Strep_{II}$-Pex14p(M51L)-ND complex respectively.

4.3.4.1 Pex5p addition to the Pex14p(M51L) - ND assembly

$Strep_{II}$-Pex14p(M51L) was reconstituted in cMSP1D1Δ4-6 lipid nanodiscs and His_6-Pex5p was purified according to section (**4.1.5)** and (**4.3.1**) respectively. After that, purified His_6-Pex5p was mixed with the proteo-lipid assembly in a 1:1 ratio, followed by a one-hour incubation at 4 °C.

Afterwards, size exclusion chromatography was performed using a Superose 6 increase 5/150 GE column pre-equilibrated in TBS Buffer (**Figure (43)**).

At 1 ml the void volume of excess lipids was eluting, followed by the main peak eluting at the range of 1.2 ml – 1.75 ml which was analyzed by SDS-PAGE electrophoresis **Figure (43.b)**. Here, the corresponding protein bands were identified at a molecular weight of 100 kDa and 34 kDa (Pex5p, Pex14p). In addition to that, the cMSP protein band was detected at a molecular weight of 12 kDa, co-eluting with the complex, suggesting successful reconstitution.

Adding to that, the second main peak elutes in-between 1.75 ml and 2.4 ml. SDS-PAGE analysis could identify only the presence of Pex5p in these fractions **Figure (43.b)**

Finally, at 2.5 ml the empty nanodisc peak is detected.

This initial experiment suggests successful binding of Pex5p to Pex14p reconstituted in nanodiscs, which however requires further verification by additional biophysical approaches.

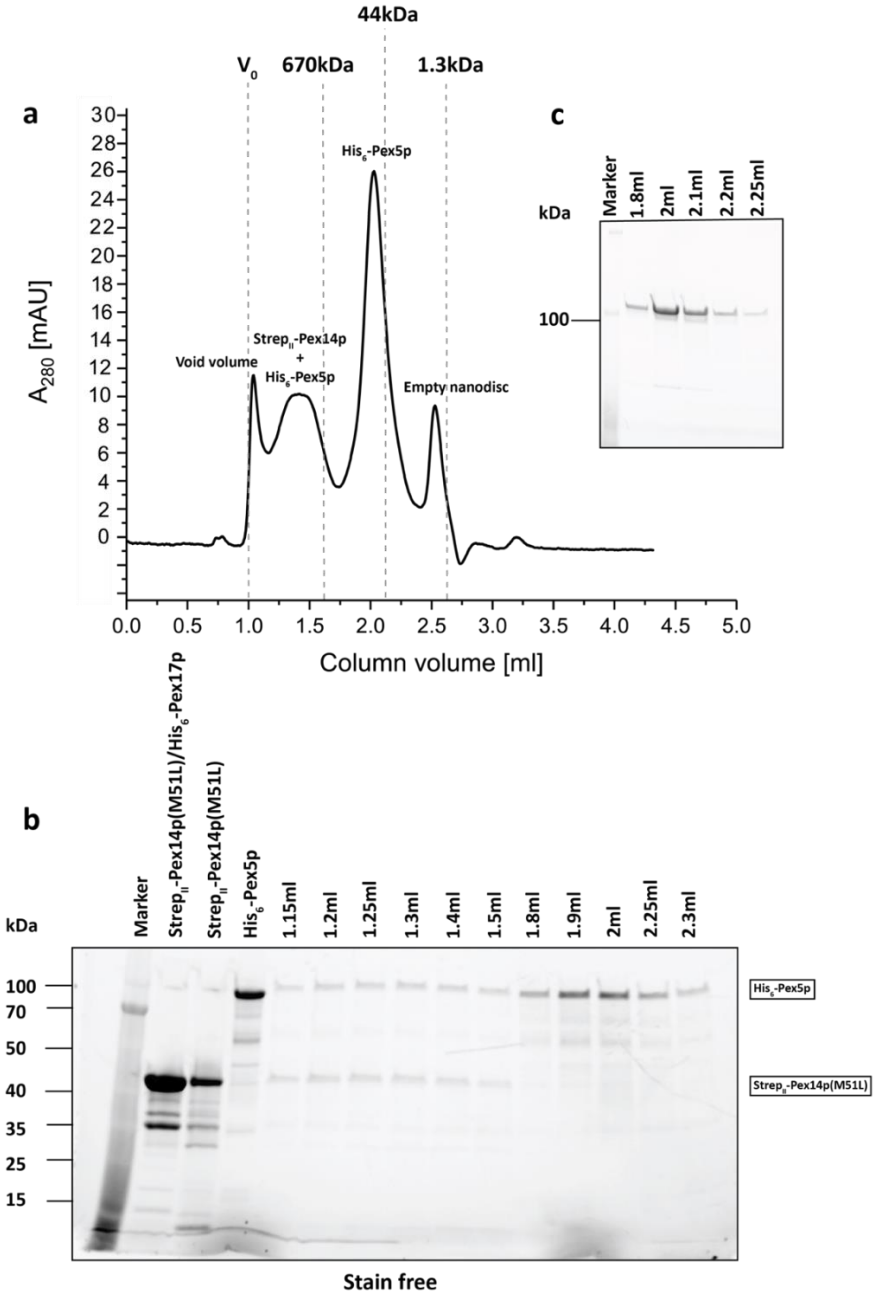

Figure (42): Size exclusion chromatography of the StrepII-Pex14p(M51L)/His_6-Pex17p/His_6-Pex5p complex reconstituted into cMS1P1DΔ46 lipid nanodiscs.

a) Chromatogram of Superose 6 Increase 5/150 GE column of $Strep_{II}$-Pex14p(M51L)/**His_6-Pex5p** complex into ND after O/N incubation on SM-2® Bio-Beads. The peak eluting at 1.2 -1.75 ml corresponds to the Pex14p/Pex17p/Pex5p-ND assembly. Following, the peak coming at 1.75 -2.4 corresponds to the excess of Pex5p that was not bound to the complex. Finally, peaks eluting at 1 ml and 2.5 ml represent the void volume and the empty NDs accordingly.

b) Stain -free SDS-PAGE of 80µl fractions of the SEC purification (complex peak analysis). Protein bands running at 100, 50 and 12 kDa correspond to Pex5p, Pex14p, and the lipid-ND.

c) Stain -free SDS-PAGE of 80µl fractions of the SEC purification (Pex5p peak analysis). Protein bands running at 100 kDa correspond to Pex5p.

c) Stain -free SDS-PAGE of 80µl fractions of the SEC purification (Pex5p peak analysis). Protein bands running at 100 kDa correspond to Pex5p.

Dashed lines represent the BioRad protein standard (#1511901).

4.3.4.2 Pex5p addition to the Pex14p(M51L)/Pex17p - ND assembly

Similar as before, the docking complex and Pex5p were purified, mixed and incubated at 4 °C. Afterwards size exclusion chromatography was performed using a Superose 6 increase 5/150 GE column pre-equilibrated in TBS Buffer (**Figure (42)**).

Comparable to the previous SEC profile, at 1 ml the void volume elutes, followed by the main peak observed around 1.2 ml – 1.75 ml, which was analyzed by SDS-PAGE electrophoresis. In this case the corresponding proteins were identified according to their molecular weight of 100, 34 and 24 kDa (Pex5p, Pex14p, Pex17p). Additionally, at 12 kDa cMSP is detected suggesting the successful reconstitution of the complex.

Adding to that, the second main peak elutes at the range of 1.75 ml – 2.4 ml. Similarly, as section (**4.3.4.1**) this peak corresponds to not-bound Pex5p.

Finally, at 2.5 ml the empty nanodisc peak is detected.

This initial experiment suggests successful binding of Pex5p to the Pex14p.Pex17p complex reconstituted in nanodiscs.

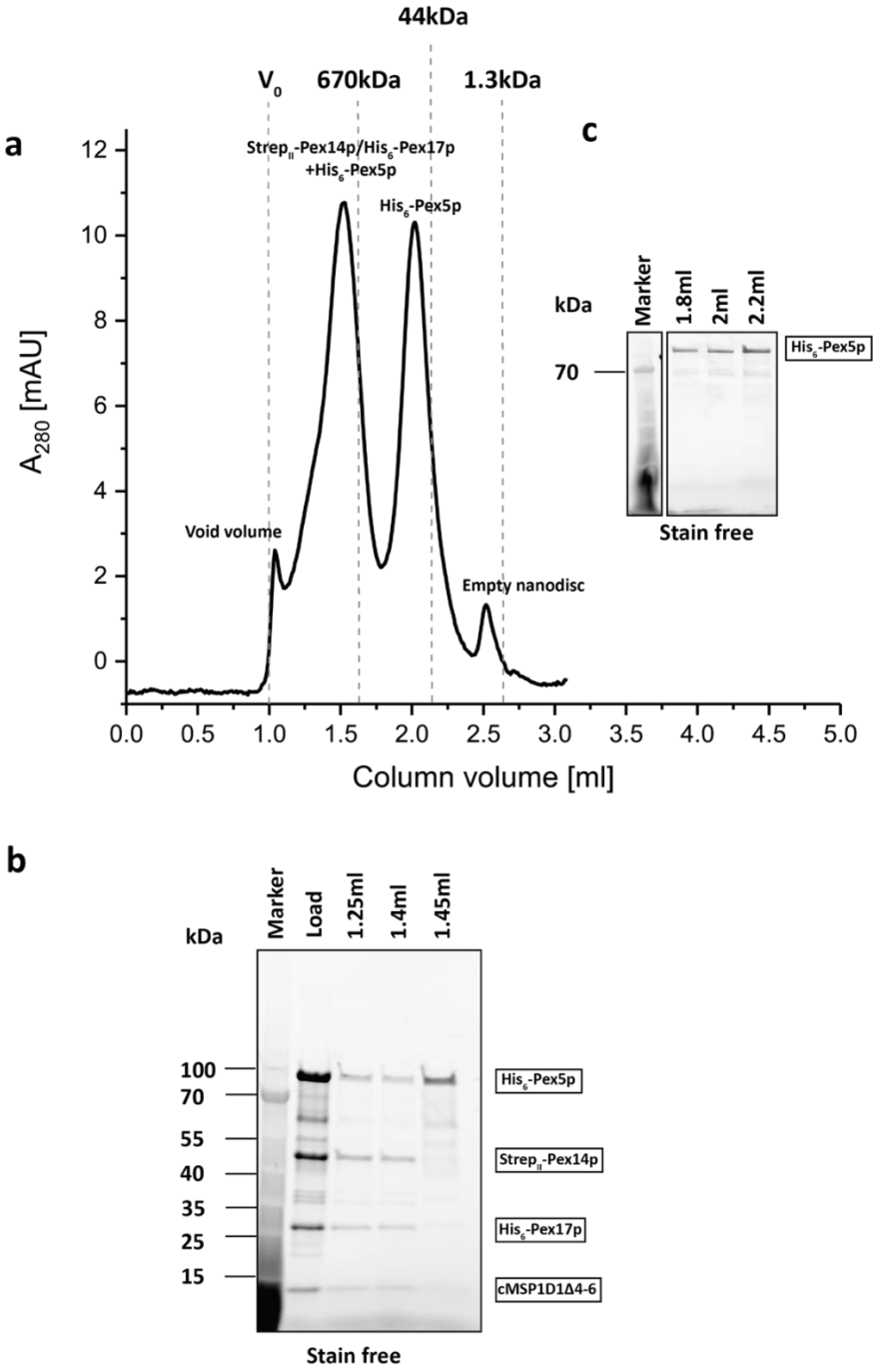

Figure (43): Size exclusion chromatography of the StrepII-Pex14p(M51L)/His_6-Pex17p/His_6-Pex5p complex reconstituted into cMS1P1DΔ46 lipid nanodiscs.

a) Chromatogram of Superose 6 Increase 5/150 GE column of $Strep_{II}$-Pex14p(M51L)/His_6-Pex17p/**His_6-Pex5p** complex into ND after O/N incubation on SM-2® Bio-Beads. The peak eluting at 1.2 -1.75 ml corresponds to the Pex14p/Pex17p/Pex5p-ND assembly. Following, the peak coming at 1.75 -2.4 corresponds to the excess of Pex5p that was not bound to the complex. Finally, peaks eluting at 1 ml and 2.5 ml represent the void volume and the empty NDs accordingly.

b) Stain -free SDS-PAGE of 80µl fractions of the SEC purification (complex peak analysis). Protein bands running at 100, 50, 29 and 12 kDa correspond to Pex5p, Pex14p, Pex17p and the lipid-ND.

c) Stain -free SDS-PAGE of 80µl fractions of the SEC purification (Pex5p peak analysis). Protein bands running at 100 kDa correspond to Pex5p.

Dashed lines represent the BioRad protein standard (#1511901).

5. Discussion

The mechanism of the peroxisomal import, still remain unclear. According to (Ma et al. 2009), the combination and synergy between the cargo-receptor, Pex5p, and the DTM components, Pex14p/Pex13p, induce the formation of the transient pore at the peroxisomal membrane. Moreover, the complex between Pex5p-Pex14p-Pex13p was further tested for channel properties (Meinecke et al. 2010). Here, the complex was incorporated into liposome-membranes and characterized with electrophysiological studies, that proved pore formation up to 9 nm even in the absence of cargo.

Additionally, structural studies (Watanabe et al. 2016) (Lill et al.), have provided a surplus of data regarding the structural characteristics of the PTS_1-importomer components, that explicate synergy between the involved peroxins and topology on the peroxisomal membrane.

However, the exact mechanism of the pore formation is still controversial. Until now, the contribution of Pex17p to the DTM and consecutively its role in pore formation remains unknown. Adding to that, stages of pore-formation are not well characterized and the peroxins participating at each stage remain obscure.

Therefore, the major undertaking is to elucidate how the different peroxins assemble and contribute to the importomer.

For this reason, we performed here comparative EM studies between different peroxin-complex-assemblies involved in docking and pore formation events.

5.1 His-tag purification of PEX14

Solubilization of the integral membrane protein is mandatory for the purification success. Since the yeast homologue was purified in the presence of 0.1% DDM (Lill et al.), the detergent type used for the purpose of PEX14 purification and solubilization was determined.

The purification was done via Ni-NTA affinity beads as described in section (**4.2.1**). The resulting purified peroxin, runs in two bands at the estimated molecular weight of 68 kDa and 120 kDa accordingly (**Figure (25.b)**). The existence of the upper is discussed to be an impuritymdue to the expression in insect cells (**Figure (26.a)**).

An additional finding of this experiment is that PEX14 is a fragile transmembrane protein. If PEX14 is subjected to a concentration step with Amicon-concentrators the DDM concentration increases as well in the solution, resulting in dissociation or aggregation of the peroxin. Additionally, if PEX14 is stored within the lysis buffer containing 1% DDM (**Table (7)**), it forms characteristic large aggregates (**Figure (44)**).

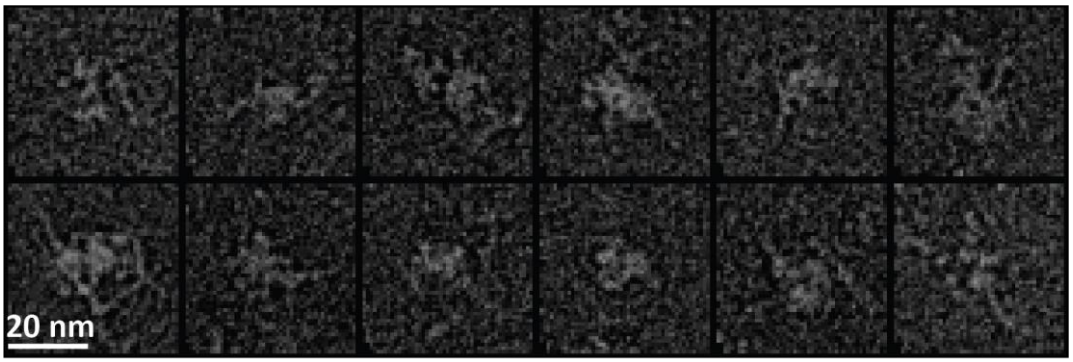

Figure (44): Negative stain particles of aggregated PEX14.

PEX14 particles observed with negative stain microscopy. In high concentrations of detergent (DDM) PEX14 was aggregating. Particles look like PEX14 filaments aggregating on top of a detergent micelle.

The quality of the PEX14 sample can be optimized by reconstitution of PEX14 into lipid nanodiscs. For this reason, cMSP has been used, as it has proven optimal for the successful reconstitution of the yeast PEx14p/Pex17p complex in previous experiments (Lill et all). This study shows that human PEX14 displays a similar architecture compared to the yeast Pex14pPex17p complex. However, yeast Pex14p alone, in absence of Pex17p, appears shorter and heterogenous. The size of human PEX14 (between 18-24 nm) matches rather the size of the yeast Pex14/Pex17p complex and not yeast Pex14 alone. This suggests a role of Pex17p on the stabilization of Pex14p in yeast, which is however not required in higher eukaryotes, where Pex17p is indeed absent. Here, we established the reconstitution protocol for the human complex and provide an initial structural characterization. Most importantly, this study sets the stage for further cryo-EM single particle analysis experiments towards a high resolution structure of this peroxin. This will allow a direct comparison and will reveal the structural differences between human and yeast PEX14.

5.2 Reconstitution in cMSP1D1Δ4-6 lipid nanodiscs

5.2.1 Pex17p importance in the Pex14p/17p yeast docking complex

In order to elucidate the importance and significance of Pex17p in the DTM, comparative studies between Pex14p/Pex17p and Pex14p alone were performed (section **(4.1)**).

In order to successfully carry out this comparison, Pex14p/Pex17p and Pex14p were both reconstituted successfully into lipid nanodiscs as described in **Table (11)** and **Table (12)** respectively.

According to the SEC chromatograms, presence of Pex17p did not contribute to a considerate shift to a higher molecular weight, which might be due to the low molecular weight of Pex17p (24 kDa) and the general elongated shape of Pex14p.

One apparent deviation is the peak eluting at 2.15 ml (**Figure (45.b)**). Since it appears only in the case of the reconstitution process regarding the Pex14p/Pex17p complex, it is suggested that it corresponds to a Pex17p-ND reconstitution. This hypothesis is also supported by SDS-PAGE analysis (**Figure (18.b)**). Regarding the fraction of 2.15 ml, a protein band corresponding to Pex17p is running at 29 kDa and below at 12 kDa the protein band of the cMSP1D1Δ4-6 is located. However, the concentration (1.5 mAU) was inadequate for further negative stain microscopy analysis and we can also not exclude by this experiment, that this fraction might correspond to monomeric Pex14p.

According to **Figure (23)** Pex14p is able to form a homotrimeric rod-shaped structure, similar to the Pex14p/17p complex. However, these elongated rods display increased heterogeneity and flexibility. This experiment was the first indication that the presence Pex17p might be connected with the stability of the docking complex.

In both cases, Pex14p and Pex14p/Pex17p appeared to be rod-shaped, resembling a thin filament protruding from the lipid ND.

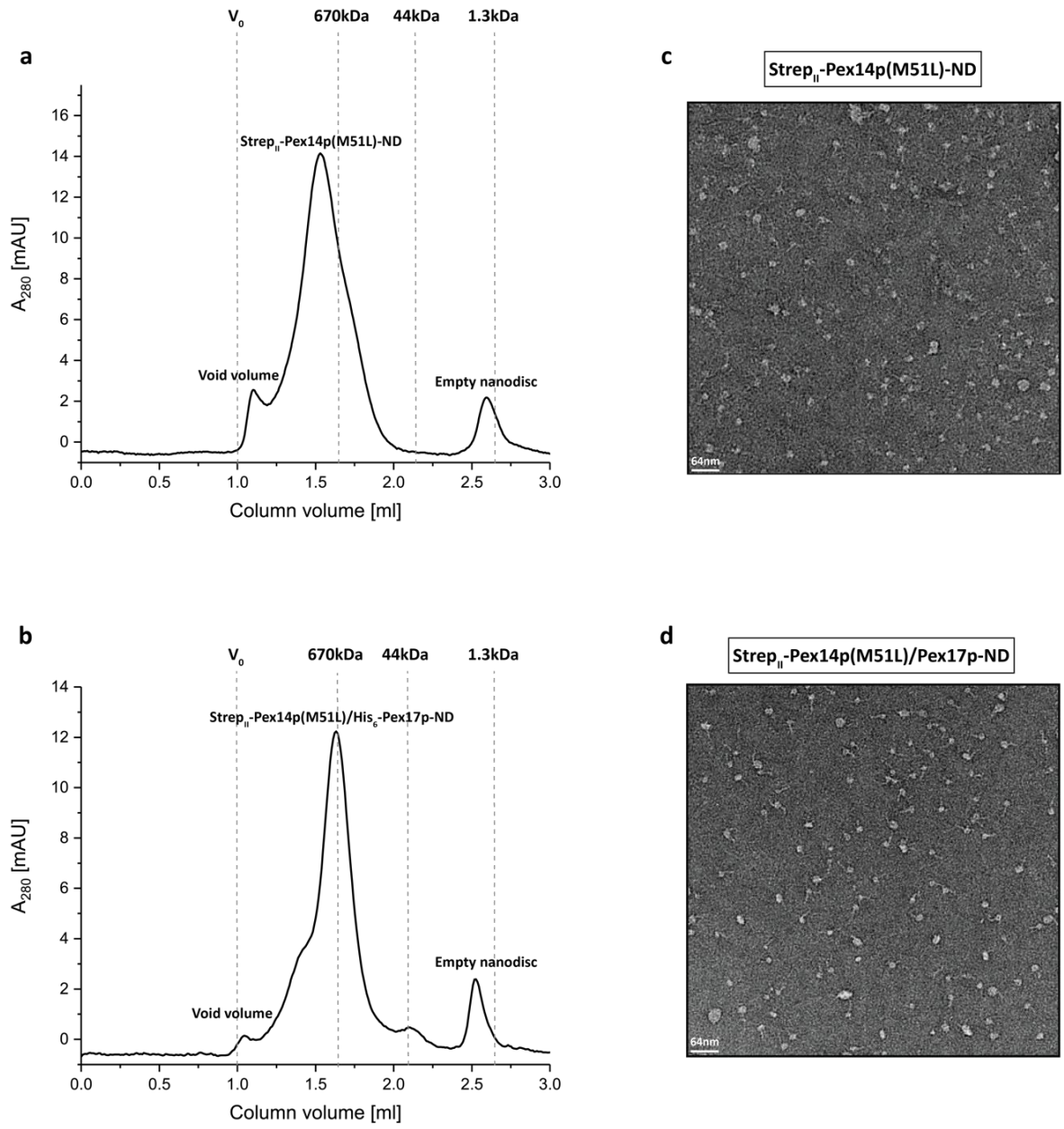

Figure (45): Size-exclusion chromatography, negative stain EM micrographs and 2D classes of Strep$_{II}$-Pex14p(M51L)/His-Pex17p complex and Strep$_{II}$-Pex14p(M51L).

a, b) Gel filtration chromatograms of the peroxin assemblies. In the Pex14p/Pex17p-ND assembly, the peak eluting at 2.15 ml is suggesting Pex17p separation from the complex and further reconstitution to the lipid ND.

c, d) Negatice stain micrographs of the Pex14p and Pex14p/Pex17p particles reconstituted in lipid ND (1:30 ratio). With a first look the reconstituted protein molecules seem quite similar.

Dashed lines represent the BioRad protein standard (#1511901).

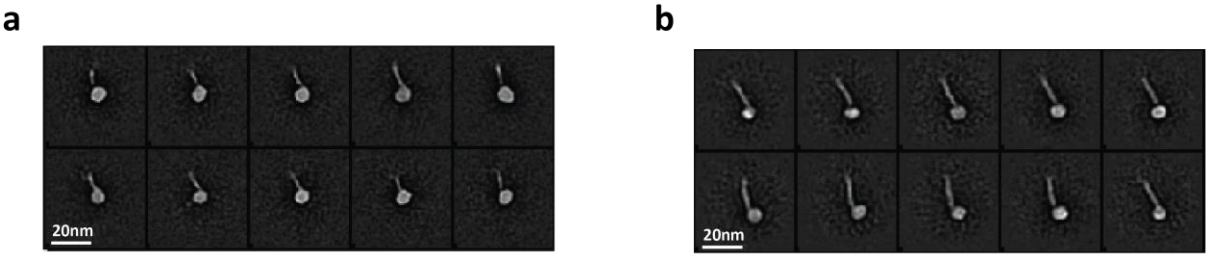

Figure (46): Selected 2D classes representing the particle clustering of the two groups.

Comparison of the Pex14p to Pex14p/Pex17p 2D class averages after reconstitution to cMSP1D1Δ4-6

a) 2D-Class averages of $Strep_{II}$-Pex14p(M51L).

d) 2D-Class averages of $Strep_{II}$-Pex14p(M51L)/His_6-Pex17p.

Pex14p filaments in the absence of Pex17p (**Figure (46)**) appear to be however more heterogeneous regarding their overall length, which varies from 10 nm up to 23 nm. Also, the rods appear thinner compared to the rods of the Pex14p/Pex17p complex.

These inconsistencies are not present in the case of the Pex14p/Pex17p complex, with the individual particles varying in contrast only 4nm in length. The individual particles appear more compact and less flexible.

Concluding, electron microscopy comparison between the two peroxin populations, resulted in the acquisition of two sets of 2D-Class averages, that presented dissimilarities regarding the structural conformation of the protein filaments. Based on the outcome, it can be assumed that Pex17p's role to the DDM complex is to provide stability to the Pex14p homotrimers.

5.2.2 PEX14 reconstitution to lipid nanodiscs

In order to characterize the human PEX14 homologue, the purified complex was reconstituted into lipid NDs, as described in **Table (13)**.

Observing the chromatogram (**Figure (28)**), it is insinuated that PEX14 was successfully reconstituted in cMSP1D1Δ4-6, similarly to the yeast samples. However, an additional peak was eluting at 2.2 ml that does not correspond (size-wise) to the PEX14 protein (68 kDa). In addition to that, a second unidentified protein band was detected during SDS-PAGE analysis. These impurities indicate the necessity to further improve the purification protocol. In addition, it might be however of general interest, to identify the respective peptide by Mass Spectrometry.

We were able to obtain an initial 3D reconstruction, which however appears flattened, most probably due to a preferred orientation of the PEX14 particles on the EM grid. We were also able to vitrify the complex and screen first conditions for cryo-EM studies. The resulting cryo-EM images were however barely visible due to bad contrast between the protein molecules and the background, making further processing impossible. It should be emphasized that due to the

elongated shape and low molecular weight of the particle, high resolution cryo-EM is expected challenging and will require extensive screening to obtain the most optimal ice thickness and quality, for the successful visualization of the particles. However, our data provide a strong foundation in this direction, towards the structural elucidation of this important component of the human importomer.

5.2.3 Importomer reconstitution to cMSP1D1Δ4-6 lipid ND

The last reconstitution experiment performed in the framework of this master thesis, was the reconstitution of the yeast docking complex Pex14p/Pex17p into circular lipid nanodiscs as a platform to analyze the effects of receptor binding to the structure of the docking complex. Thus, providing a direct comparison between the docking complex alone and docking/receptor complex.

Adding to that, the receptor was also tested for binding only to Pex14p reconstituted into ND in order to distinguish deviations regarding receptor binding based on the presence of Pex17p. The initial studies of SDS-PAGE analysis, suggest that the receptor (Pex5p) is binding even in the absence of PTS_1-cargo to the docking complex regardless of the presence of Pex17p (**Figures (41.b) (42.b)**). However, further verification by additional biophysical approaches is necessary to validate binding.

5.3 Complex formation of Pex14p/Pex17p and Pex5p in liposomes

Finally, in section **(4.3)**, the complex formation of Pex5p with Pex14p/Pex17p decorated liposomes (**Figure (40)**) is described. According to (Ma et al. 2009) and also the electrophysiological studies of (Meinecke et al. 2010) regarding pore formation, both have already proven that a pore is able to form in a membrane, in the presence of the peroxins comprising the importomer (Pex5p, Pex14p and Pex17p) under certain conditions.

Formation of the Pex14p/Pex17p decorated liposomes and further addition of Pex5p in combination with a known PTS_1-cargo protein (like Pcs60p (Hagen et al. 2015)) was previously shown to accomplish successful import of the cargo. Here, in this thesis, a Pex14p/Pex17p/Pex5p complex was assembled successfully, upon addition of the receptor to docking complexes reconstituted in liposomes. However, visualization of Pex14p/Pex17p-proteoliposomes upon addition of Pex5p, did not reveal any characteristic structural changes at the liposomes' surface. Moreover, we cannot confirm successful pore formation under these

conditions; however, it will be interesting to repeat these studies and add a cargo-receptor complex to the proteoliposomes of the docking complex, instead of receptor alone.
In addition to that, as described before, negative stain electron microscopy can lead to flattening of structures and fragmentation of the bilayer. Therefore, it will be necessary to visualize the proteoliposomes in a close to native environment using cryo-EM.

6. Summary and outlook

In this study, we purified and reconstituted yeast Pex14p/Pex17p, Pex14p and human PEX14 in lipid nanodiscs and prepared optimal samples for subsequent cryo-EM comparative analyses of the respective peroxins. These will be crucial to reveal distinct differences between the human and yeast homologues and the contribution of Pex17p to the yeast docking complex. A preliminary comparative analysis using negative stain EM, suggests that Pex17p contributes significantly to the stability of the PEx14p/Pex17p complex. Furthermore, first cryo-EM screenings of human PEX14-ND were performed, which however require further optimization to achieve optimal ice thickness and improve the contrast of the particles.

Analysis of the yeast docking complex after addition of the receptor Pex5p, suggests successful complex formation, even in the absence of a PTS_1 cargo protein. Further analyses are however required in order to elucidate the structure and overall topology of this complex. Proteoliposomes displaying the docking complex at their surface were successfully assembled for future in vitro pore formation studies, towards visualization of the peroxisomal import pore using cryo-EM.

7. References

"Advances in Atomic, Molecular, and Optical Physics." 2013. *Advances In Atomic, Molecular, and Optical Physics*. https://doi.org/10.1016/b978-0-12-408090-4.00007-4.

Anderluh, Gregor, and Jeremy H. Lakey. 2008. "Disparate Proteins Use Similar Architectures to Damage Membranes." *Trends in Biochemical Sciences* 33 (10): 482–90.

Azevedo, Jorge E., and Wolfgang Schliebs. 2006. "Pex14p, More than Just a Docking Protein." *Biochimica et Biophysica Acta* 1763 (12): 1574–84.

Bai, Xiao-Chen, Greg McMullan, and Sjors H. W. Scheres. 2015. "How Cryo-EM Is Revolutionizing Structural Biology." *Trends in Biochemical Sciences* 40 (1): 49–57.

Baker, Alison, Thomas Lanyon-Hogg, and Stuart L. Warriner. 2016. "Correction: Peroxisome Protein Import: A Complex Journey." *Biochemical Society Transactions*. https://doi.org/10.1042/bst0441183b.

Barros-Barbosa, Aurora, Maria J. Ferreira, Tony A. Rodrigues, Ana G. Pedrosa, Cláudia P. Grou, Manuel P. Pinto, Marc Fransen, Tânia Francisco, and Jorge E. Azevedo. 2019. "Membrane Topologies of PEX13 and PEX14 Provide New Insights on the Mechanism of Protein Import into Peroxisomes." *The FEBS Journal* 286 (1): 205–22.

Bartesaghi, Alberto, Alan Merk, Soojay Banerjee, Doreen Matthies, Xiongwu Wu, Jacqueline L. S. Milne, and Sriram Subramaniam. 2015. "2.2 Å Resolution Cryo-EM Structure of β-Galactosidase in Complex with a Cell-Permeant Inhibitor." *Science* 348 (6239): 1147–51.

———. 2010. "Membrane Protein Assembly into Nanodiscs." *FEBS Letters*. https://doi.org/10.1016/j.febslet.2009.10.024.

Benjin, Xu, and Liu Ling. 2020. "Developments, Applications, and Prospects of Cryo-electron Microscopy." *Protein Science*. https://doi.org/10.1002/pro.3805.

Bilbao-Castro, J. R., J. M. Carazo, I. García, and J. J. Fernández. 2006. "Parallelization of Reconstruction Algorithms in Three-Dimensional Electron Microscopy." *Applied Mathematical Modelling*. https://doi.org/10.1016/j.apm.2005.05.019.

Birschmann, Ingvild, Katja Rosenkranz, Ralf Erdmann, and Wolf-H Kunau. 2005. "Structural and Functional Analysis of the Interaction of the AAA-Peroxins Pex1p and Pex6p." *The FEBS Journal* 272 (1): 47–58.

Birschmann, Ingvild, An K. Stroobants, Marlene van den Berg, Antje Schäfer, Katja Rosenkranz, Wolf-H Kunau, and Henk F. Tabak. 2003. "Pex15p of Saccharomyces Cerevisiae Provides a Molecular Basis for Recruitment of the AAA Peroxin Pex6p to Peroxisomal Membranes." *Molecular Biology of the Cell* 14 (6): 2226–36.

Bogner, A., P-H Jouneau, G. Thollet, D. Basset, and C. Gauthier. 2007. "A History of Scanning Electron Microscopy Developments: Towards 'Wet-STEM' Imaging." *Micron* 38 (4): 390–401.

Bosch, H. van den, R. B. H. Schutgens, R. J. A. Wanders, and J. M. Tager. 1992. "Biochemistry of Peroxisomes." *Annual Review of Biochemistry*. https://doi.org/10.1146/annurev.bi.61.070192.001105.

Boteva, Raina, Anne Koek, Nina V. Visser, Antonie J. W. G. Visser, Elmar Krieger, Theodora Zlateva, Marten Veenhuis, and Ida van der Klei. 2003. "Fluorescence Analysis of the Hansenula Polymorpha Peroxisomal Targeting Signal-1 Receptor, Pex5p." *European Journal of Biochemistry / FEBS* 270 (21): 4332–38.

Brilot, Axel F., James Z. Chen, Anchi Cheng, Junhua Pan, Stephen C. Harrison, Clinton S. Potter, Bridget Carragher, Richard Henderson, and Nikolaus Grigorieff. 2012. "Beam-Induced

Motion of Vitrified Specimen on Holey Carbon Film." *Journal of Structural Biology* 177 (3): 630–37.

Broglie, Louis De, and Louis De Broglie. 1925. "Recherches Sur La Théorie Des Quanta." *Annales de Physique*. https://doi.org/10.1051/anphys/192510030022.

Carvalho, Andreia F., João Costa-Rodrigues, Isabel Correia, João Costa Pessoa, Tiago Q. Faria, Cristina L. Martins, Marc Fransen, Clara Sá-Miranda, and Jorge E. Azevedo. 2006. "The N-Terminal Half of the Peroxisomal Cycling Receptor Pex5p Is a Natively Unfolded Domain." *Journal of Molecular Biology* 356 (4): 864–75.

Cheng, Yifan. 2015. "Single-Particle Cryo-EM at Crystallographic Resolution." *Cell* 161 (3): 450–57.

Cheng, Yifan, Nikolaus Grigorieff, Pawel A. Penczek, and Thomas Walz. 2015. "A Primer to Single-Particle Cryo-Electron Microscopy." *Cell* 161 (3): 438–49.

Corpas, Francisco J., and Juan B. Barroso. 2018. "Peroxisomal Plant Metabolism - an Update on Nitric Oxide, Ca and the NADPH Recycling Network." *Journal of Cell Science* 131 (2). https://doi.org/10.1242/jcs.202978.

Cosentino, Katia, Uris Ros, and Ana J. García-Sáez. 2016. "Assembling the Puzzle: Oligomerization of α-Pore Forming Proteins in Membranes." *Biochimica et Biophysica Acta* 1858 (3): 457–66.

Cross, Timothy A., Dylan T. Murray, and Anthony Watts. 2013. "Helical Membrane Protein Conformations and Their Environment." *European Biophysics Journal: EBJ* 42 (10): 731–55.

D'Andrea, Luca D., and Lynne Regan. 2003. "TPR Proteins: The Versatile Helix." *Trends in Biochemical Sciences* 28 (12): 655–62.

De Carlo, Sacha, and J. Robin Harris. 2011. "Negative Staining and Cryo-Negative Staining of Macromolecules and Viruses for TEM." *Micron* 42 (2): 117–31.

De Duve, C., and P. Baudhuin. 1966. "Peroxisomes (microbodies and Related Particles)." *Physiological Reviews* 46 (2): 323–57.

Denisov, Ilia G., and Stephen G. Sligar. 2016. "Nanodiscs for Structural and Functional Studies of Membrane Proteins." *Nature Structural & Molecular Biology*. https://doi.org/10.1038/nsmb.3195.

Dias, Ana F., Tony A. Rodrigues, Ana G. Pedrosa, Aurora Barros-Barbosa, Tânia Francisco, and Jorge E. Azevedo. 2017. "The Peroxisomal Matrix Protein Translocon Is a Large Cavity-Forming Protein Assembly into Which PEX5 Protein Enters to Release Its Cargo." *The Journal of Biological Chemistry* 292 (37): 15287–300.

Doerr, Allison. 2016. "Single-Particle Cryo-Electron Microscopy." *Nature Methods* 13 (1): 23.

Doerr, Allison, Joshua Finkelstein, Irene Jarchum, Catherine Goodman, and Bronwen Dekker. 2015. "Editorial." *Nature Methods*. https://doi.org/10.1038/nmeth.3558.

Dubochet, J. 1987. "Cryo-Electron Microscopy of Viruses in Native State." *Micron and Microscopica Acta*. https://doi.org/10.1016/0739-6260(87)90035-9.

Efremov, Rouslan G., Christos Gatsogiannis, and Stefan Raunser. 2017. "Lipid Nanodiscs as a Tool for High-Resolution Structure Determination of Membrane Proteins by Single-Particle Cryo-EM." *Methods in Enzymology* 594 (July): 1–30.

Egelman, Edward H. 2016. "The Current Revolution in Cryo-EM." *Biophysical Journal* 110 (5): 1008–12.

Eisenstein, Michael. 2016. "Erratum: Corrigendum: The Field That Came in from the Cold." *Nature Methods*. https://doi.org/10.1038/nmeth0416-379.

El Magraoui, Fouzi, Rebecca Brinkmeier, Thomas Mastalski, Alexander Hupperich, Christofer Strehl, Daniel Schwerter, Wolfgang Girzalsky, et al. 2019. "The Deubiquitination of the PTS1-Import Receptor Pex5p Is Required for Peroxisomal Matrix Protein Import." *Biochimica et Biophysica Acta, Molecular Cell Research* 1866 (2): 199–213.

Emmanouilidis, Leonidas, Mohanraj Gopalswamy, Daniel M. Passon, Matthias Wilmanns, and Michael Sattler. 2016. "Structural Biology of the Import Pathways of Peroxisomal Matrix Proteins." *Biochimica et Biophysica Acta* 1863 (5): 804–13.

Erdmann, Ralf, and Wolfgang Schliebs. 2005. "Peroxisomal Matrix Protein Import: The Transient Pore Model." *Nature Reviews. Molecular Cell Biology* 6 (9): 738–42.

Faber, Klaas Nico, Ralf van Dijk, Ineke Keizer-Gunnink, Anne Koek, Ida J. van der Klei, and Marten Veenhuis. 2002. "Import of Assembled PTS1 Proteins into Peroxisomes of the Yeast Hansenula Polymorpha: Yes and No!" *Biochimica et Biophysica Acta* 1591 (1-3): 157–62.

Faruqi, A. R., and G. McMullan. 2018a. "Direct Imaging Detectors for Electron Microscopy." *Nuclear Instruments and Methods in Physics Research Section A: Accelerators, Spectrometers, Detectors and Associated Equipment*. https://doi.org/10.1016/j.nima.2017.07.037.

Fradin, Cécile, Dmitri Satsoura, and David W. Andrews. 2009. "Punching Holes in Membranes: How Oligomeric Pore-Forming Proteins and Lipids Cooperate to Form Aqueous Channels in Membranes." *Biomembrane Frontiers*. https://doi.org/10.1007/978-1-60761-314-5_9.

Frank, Joachim. 2018. "Single-Particle Reconstruction of Biological Molecules-Story in a Sample (Nobel Lecture)." *Angewandte Chemie International Edition*. https://doi.org/10.1002/anie.201802770.

Fransen, Marc, Marcus Nordgren, Bo Wang, and Oksana Apanasets. 2012. "Role of Peroxisomes in ROS/RNS-Metabolism: Implications for Human Disease." *Biochimica et Biophysica Acta* 1822 (9): 1363–73.

Friedrich, Heiner, Petra E. de Jongh, Arie J. Verkleij, and Krijn P. de Jong. 2009. "Electron Tomography for Heterogeneous Catalysts and Related Nanostructured Materials." *Chemical Reviews* 109 (5): 1613–29.

Fujiki, Yukio, Chika Nashiro, Non Miyata, Shigehiko Tamura, and Kanji Okumoto. 2012. "New Insights into Dynamic and Functional Assembly of the AAA Peroxins, Pex1p and Pex6p, and Their Membrane Receptor Pex26p in Shuttling of PTS1-Receptor Pex5p during Peroxisome Biogenesis." *Biochimica et Biophysica Acta* 1823 (1): 145–49.

Gabaldón, Toni. 2010. "Peroxisome Diversity and Evolution." *Philosophical Transactions of the Royal Society B: Biological Sciences*. https://doi.org/10.1098/rstb.2009.0240.

Garreau, G. A., and Walter Rudin. 1987. "Real and Complex Analysis." *The Statistician*. https://doi.org/10.2307/2348852.

Gatto, G. J., Jr, B. V. Geisbrecht, S. J. Gould, and J. M. Berg. 2000. "Peroxisomal Targeting Signal-1 Recognition by the TPR Domains of Human PEX5." *Nature Structural Biology* 7 (12): 1091–95.

Glaeser, Robert M. 2016. "How Good Can Cryo-EM Become?" *Nature Methods* 13 (1): 28–32.

Goto, Shino, Shoji Mano, Chihiro Nakamori, and Mikio Nishimura. 2011. "Arabidopsis ABERRANT PEROXISOME MORPHOLOGY9 Is a Peroxin That Recruits the PEX1-PEX6 Complex to Peroxisomes." *The Plant Cell* 23 (4): 1573–87.

Gouaux, E. 1997. "Channel-Forming Toxins: Tales of Transformation." *Current Opinion in Structural Biology* 7 (4): 566–73.

Gould, S. J., G. A. Keller, N. Hosken, J. Wilkinson, and S. Subramani. 1989. "A Conserved Tripeptide Sorts Proteins to Peroxisomes." *The Journal of Cell Biology* 108 (5): 1657–64.

Gouveia, Alexandra M., Carla P. Guimarães, Márcia E. Oliveira, Carlos Reguenga, Clara Sá-Miranda, and Jorge E. Azevedo. 2003. "Characterization of the Peroxisomal Cycling Receptor, Pex5p, Using a Cell-Freein VitroImport System." *Journal of Biological Chemistry*. https://doi.org/10.1074/jbc.m209498200.

Gouveia, A. M., C. Reguenga, M. E. Oliveira, C. Sa-Miranda, and J. E. Azevedo. 2000. "Characterization of Peroxisomal Pex5p from Rat Liver. Pex5p in the Pex5p-Pex14p

Membrane Complex Is a Transmembrane Protein." *The Journal of Biological Chemistry* 275 (42): 32444–51.

Hagen, Stefanie, Friedel Drepper, Sven Fischer, Krisztian Fodor, Daniel Passon, Harald W. Platta, Michael Zenn, et al. 2015. "Structural Insights into Cargo Recognition by the Yeast PTS1 Receptor." *The Journal of Biological Chemistry* 290 (44): 26610–26.

Hänsch, Robert, and Ralf R. Mendel. 2005. "Sulfite Oxidation in Plant Peroxisomes." *Photosynthesis Research* 86 (3): 337–43.

Harano, T., S. Nose, R. Uezu, N. Shimizu, and Y. Fujiki. 2001. "Hsp70 Regulates the Interaction between the Peroxisome Targeting Signal Type 1 (PTS1)-Receptor Pex5p and PTS1." *Biochemical Journal* 357 (Pt 1): 157–65.

Harris, J. Robin. 2007. "Negative Staining of Thinly Spread Biological Samples." *Methods in Molecular Biology* 369: 107–42.

Hoop, M. J. de, M. J. de Hoop, and G. Ab. 1992. "Import of Proteins into Peroxisomes and Other Microbodies." *Biochemical Journal*. https://doi.org/10.1042/bj2860657.

Houdellier, F., L. de Knoop, C. Gatel, A. Masseboeuf, S. Mamishin, Y. Taniguchi, M. Delmas, M. Monthioux, M. J. Hÿtch, and E. Snoeck. 2015. "Development of TEM and SEM High Brightness Electron Guns Using Cold-Field Emission from a Carbon Nanotip." *Ultramicroscopy* 151 (April): 107–15.

Iacovache, Ioan, Mirko Bischofberger, and F. Gisou van der Goot. 2010. "Structure and Assembly of Pore-Forming Proteins." *Current Opinion in Structural Biology*. https://doi.org/10.1016/j.sbi.2010.01.013.

Islinger, Markus, Ka Wan Li, Jürgen Seitz, Alfred Völkl, and Georg H. Lüers. 2009. "Hitchhiking of Cu/Zn Superoxide Dismutase to Peroxisomes--Evidence for a Natural Piggyback Import Mechanism in Mammals." *Traffic* 10 (11): 1711–21.

Jiang, Linhua, Zunfeng Liu, Dilyana Georgieva, Maxim E. Kuil, and Jan Pieter Abrahams. 2010. "A Novel Approximation Method of CTF Amplitude Correction for 3D Single Particle Reconstruction." *Ultramicroscopy* 110 (4): 350–58.

Kalel, Vishal C., and Ralf Erdmann. 2018. "Unraveling of the Structure and Function of Peroxisomal Protein Import Machineries." *Sub-Cellular Biochemistry* 89: 299–321.

Kaur, Navneet, Sigrun Reumann, and Jianping Hu. 2009. "Peroxisome Biogenesis and Function." *The Arabidopsis Book*. https://doi.org/10.1199/tab.0123.

Kerssen, Daniela, Eva Hambruch, Wibke Klaas, Harald W. Platta, Ben de Kruijff, Ralf Erdmann, Wolf-H Kunau, and Wolfgang Schliebs. 2006. "Membrane Association of the Cycling Peroxisome Import Receptor Pex5p." *The Journal of Biological Chemistry* 281 (37): 27003–15.

Kiel, Jan A. K. W., Kerstin Emmrich, Helmut E. Meyer, and Wolf-H Kunau. 2005. "Ubiquitination of the Peroxisomal Targeting Signal Type 1 Receptor, Pex5p, Suggests the Presence of a Quality Control Mechanism during Peroxisomal Matrix Protein Import." *The Journal of Biological Chemistry* 280 (3): 1921–30.

Klein, André T. J., Marlene van den Berg, Gina Bottger, Henk F. Tabak, and Ben Distel. 2002. "Saccharomyces cerevisiaeAcyl-CoA Oxidase Follows a Novel, Non-PTS1, Import Pathway into Peroxisomes That Is Dependent on Pex5p." *Journal of Biological Chemistry*. https://doi.org/10.1074/jbc.m203254200.

Knol, J., K. Sjollema, and B. Poolman. 1998. "Detergent-Mediated Reconstitution of Membrane Proteins." *Biochemistry* 37 (46): 16410–15.

Knoll, M., and E. Ruska. 1932. "Das Elektronenmikroskop." *Zeitschrift F*[illegible]*r Physik*. https://doi.org/10.1007/bf01330526.

Kühlbrandt, Werner. 2014. "Cryo-EM Enters a New Era." *eLife*.

Lametschwandtner, G., C. Brocard, M. Fransen, P. Van Veldhoven, J. Berger, and A. Hartig. 1998. "The Difference in Recognition of Terminal Tripeptides as Peroxisomal Targeting

Signal 1 between Yeast and Human Is due to Different Affinities of Their Receptor Pex5p to the Cognate Signal and to Residues Adjacent to It." *The Journal of Biological Chemistry* 273 (50): 33635–43.

Lesieur, C., B. Vécsey-Semjén, L. Abrami, M. Fivaz, and F. Gisou van der Goot. 1997. "Membrane Insertion: The Strategies of Toxins (review)." *Molecular Membrane Biology* 14 (2): 45–64.

Lill, Pascal, Tobias Hansen, Daniel Wendscheck, Bjoern Udo Klink, Tomasz Jeziorek, Jonas Miehling, Julian Bender, et al. n.d. "Towards the Molecular Architecture of the Peroxisomal Receptor Docking Complex." https://doi.org/10.1101/854497.

Lodhi, Irfan J., and Clay F. Semenkovich. 2014. "Peroxisomes: A Nexus for Lipid Metabolism and Cellular Signaling." *Cell Metabolism* 19 (3): 380–92.

Ma, Changle, Danielle Hagstrom, Soumi Guha Polley, and Suresh Subramani. 2013. "Redox-Regulated Cargo Binding and Release by the Peroxisomal Targeting Signal Receptor, Pex5." *The Journal of Biological Chemistry* 288 (38): 27220–31.

Ma, Changle, Uwe Schumann, Naganand Rayapuram, and Suresh Subramani. 2009. "The Peroxisomal Matrix Import of Pex8p Requires Only PTS Receptors and Pex14p." *Molecular Biology of the Cell* 20 (16): 3680–89.

Meinecke, Michael, Philipp Bartsch, and Richard Wagner. 2016. "Peroxisomal Protein Import Pores." *Biochimica et Biophysica Acta* 1863 (5): 821–27.

Meinecke, Michael, Christian Cizmowski, Wolfgang Schliebs, Vivien Krüger, Sabrina Beck, Richard Wagner, and Ralf Erdmann. 2010. "The Peroxisomal Importomer Constitutes a Large and Highly Dynamic Pore." *Nature Cell Biology* 12 (3): 273–77.

Merk, Alan, Alberto Bartesaghi, Soojay Banerjee, Veronica Falconieri, Prashant Rao, Mindy I. Davis, Rajan Pragani, et al. 2016. "Breaking Cryo-EM Resolution Barriers to Facilitate Drug Discovery." *Cell* 165 (7): 1698–1707.

Miehling, Jonas, David Goricanec, and Franz Hagn. 2018. "A Split-Intein-Based Method for the Efficient Production of Circularized Nanodiscs for Structural Studies of Membrane Proteins." *Chembiochem: A European Journal of Chemical Biology* 19 (18): 1927–33.

Miyata, Non, and Yukio Fujiki. 2005. "Shuttling Mechanism of Peroxisome Targeting Signal Type 1 Receptor Pex5: ATP-Independent Import and ATP-Dependent Export." *Molecular and Cellular Biology* 25 (24): 10822–32.

Moriya, Toshio, Michael Saur, Markus Stabrin, Felipe Merino, Horatiu Voicu, Zhong Huang, Pawel A. Penczek, Stefan Raunser, and Christos Gatsogiannis. 2017. "High-Resolution Single Particle Analysis from Electron Cryo-Microscopy Images Using SPHIRE." *Journal of Visualized Experiments: JoVE*, no. 123 (May). https://doi.org/10.3791/55448.

Murata, Kazuyoshi, and Matthias Wolf. 2018. "Cryo-Electron Microscopy for Structural Analysis of Dynamic Biological Macromolecules." *Biochimica et Biophysica Acta, General Subjects* 1862 (2): 324–34.

Neufeld, Christian, Fabian V. Filipp, Bernd Simon, Alexander Neuhaus, Nicole Schüller, Christine David, Hamed Kooshapur, et al. 2009. "Structural Basis for Competitive Interactions of Pex14 with the Import Receptors Pex5 and Pex19." *The EMBO Journal* 28 (6): 745–54.

Neuhaus, Alexander, Hamed Kooshapur, Janina Wolf, N. Helge Meyer, Tobias Madl, Jürgen Saidowsky, Eva Hambruch, et al. 2014. "A Novel Pex14 Protein-Interacting Site of Human Pex5 Is Critical for Matrix Protein Import into Peroxisomes." *The Journal of Biological Chemistry* 289 (1): 437–48.

Niederhoff, Karsten, Nadja M. Meindl-Beinker, Daniela Kerssen, Uta Perband, Antje Schäfer, Wolfgang Schliebs, and Wolf-H Kunau. 2005. "Yeast Pex14p Possesses Two Functionally Distinct Pex5p and One Pex7p Binding Sites." *The Journal of Biological Chemistry* 280 (42): 35571–78.

Nogales, Eva, and Sjors H. W. Scheres. 2015. “Cryo-EM: A Unique Tool for the Visualization of Macromolecular Complexity.” *Molecular Cell* 58 (4): 677–89.

“Nuclear Analytical Techniques in Medicine.” 1988. *Techniques and Instrumentation in Analytical Chemistry*. https://doi.org/10.1016/s0167-9244(08)x7012-x.

Ohi, Melanie, Ying Li, Yifan Cheng, and Thomas Walz. 2004. “Negative Staining and Image Classification - Powerful Tools in Modern Electron Microscopy.” *Biological Procedures Online* 6 (March): 23–34.

Orlova, E. V., and H. R. Saibil. 2011. “Structural Analysis of Macromolecular Assemblies by Electron Microscopy.” *Chemical Reviews*. https://doi.org/10.1021/cr100353t.

Parker, Michael W., and Susanne C. Feil. 2005. “Pore-Forming Protein Toxins: From Structure to Function.” *Progress in Biophysics and Molecular Biology* 88 (1): 91–142.

Passmore, L. A., and C. J. Russo. 2016. “Specimen Preparation for High-Resolution Cryo-EM.” *Methods in Enzymology* 579 (June): 51–86.

Patel, Khushali J., Yun-Ting Kao, Roxanna J. Llinas, and Bonnie Bartel. 2019. “A PEX5 Missense Allele Preferentially Disrupts PTS1 Cargo Import into Arabidopsis Peroxisomes.” *Plant Direct*. https://doi.org/10.1002/pld3.128.

Pedrosa, Ana G., Tânia Francisco, Diana Bicho, Ana F. Dias, Aurora Barros-Barbosa, Vera Hagmann, Gabriele Dodt, Tony A. Rodrigues, and Jorge E. Azevedo. 2018. “Peroxisomal Monoubiquitinated PEX5 Interacts with the AAA ATPases PEX1 and PEX6 and Is Unfolded during Its Dislocation into the Cytosol.” *The Journal of Biological Chemistry* 293 (29): 11553–63.

Penczek, Pawel A., Jia Fang, Xueming Li, Yifan Cheng, Justus Loerke, and Christian M. T. Spahn. 2014. “CTER-Rapid Estimation of CTF Parameters with Error Assessment.” *Ultramicroscopy* 140 (May): 9–19.

Platta, Harald W., Rebecca Brinkmeier, Christina Reidick, Silvia Galiani, Mathias P. Clausen, and Christian Eggeling. 2016. “Regulation of Peroxisomal Matrix Protein Import by Ubiquitination.” *Biochimica et Biophysica Acta* 1863 (5): 838–49.

Platta, Harald W., Fouzi El Magraoui, Daniel Schlee, Silke Grunau, Wolfgang Girzalsky, and Ralf Erdmann. 2007. “Ubiquitination of the Peroxisomal Import Receptor Pex5p Is Required for Its Recycling.” *Journal of Cell Biology*. https://doi.org/10.1083/jcb.200611012.

Platta, Harald W., Wolfgang Girzalsky, and Ralf Erdmann. 2004. “Ubiquitination of the Peroxisomal Import Receptor Pex5p.” *Biochemical Journal* 384 (Pt 1): 37–45.

Platta, Harald W., Silke Grunau, Katja Rosenkranz, Wolfgang Girzalsky, and Ralf Erdmann. 2005. “Functional Role of the AAA Peroxins in Dislocation of the Cycling PTS1 Receptor back to the Cytosol.” *Nature Cell Biology* 7 (8): 817–22.

Porter, Keith R., Albert Claude, and Ernest F. Fullam. 1945. “A STUDY OF TISSUE CULTURE CELLS BY ELECTRON MICROSCOPY.” *The Journal of Experimental Medicine*. https://doi.org/10.1084/jem.81.3.233.

Reimer, L., and M. Wächter. 1978. “Contribution to the Contamination Problem in Transmission Electron Microscopy.” *Ultramicroscopy* 3 (2): 169–74.

Reumann, Sigrun, and Andreas P. M. Weber. 2006. “Plant Peroxisomes Respire in the Light: Some Gaps of the Photorespiratory C2 Cycle Have Become Filled--Others Remain.” *Biochimica et Biophysica Acta* 1763 (12): 1496–1510.

Rhodes, Gale. 2006. “An Overview of Protein Crystallography.” *Crystallography Made Crystal Clear*. https://doi.org/10.1016/b978-012587073-3/50004-0.

———. 2009b. “Reconstitution of Membrane Proteins in Phospholipid Bilayer Nanodiscs.” *Methods in Enzymology*. https://doi.org/10.1016/s0076-6879(09)64011-8.

Rivera-Calzada, Angel, and Marta Carroni. 2019. “Editorial: Technical Advances in Cryo-Electron Microscopy.” *Frontiers in Molecular Biosciences* 6 (August): 72.

Ros, Uris, and Ana J. García-Sáez. 2015. “More Than a Pore: The Interplay of Pore-Forming Proteins and Lipid Membranes.” *The Journal of Membrane Biology* 248 (3): 545–61.

Saidowsky, J., G. Dodt, K. Kirchberg, A. Wegner, W. Nastainczyk, W. H. Kunau, and W. Schliebs. 2001. “The Di-Aromatic Pentapeptide Repeats of the Human Peroxisome Import Receptor PEX5 Are Separate High Affinity Binding Sites for the Peroxisomal Membrane Protein PEX14.” *The Journal of Biological Chemistry* 276 (37): 34524–29.

Scarff, Charlotte A., Martin J. G. Fuller, Rebecca F. Thompson, and Matthew G. Iadanza. 2018. “Variations on Negative Stain Electron Microscopy Methods: Tools for Tackling Challenging Systems.” *Journal of Visualized Experiments: JoVE*, no. 132 (February). https://doi.org/10.3791/57199.

Scheres, Sjors H. W. 2012. “RELION: Implementation of a Bayesian Approach to Cryo-EM Structure Determination.” *Journal of Structural Biology* 180 (3): 519–30.

Schulz, G. E. 1996. “Porins: General to Specific, Native to Engineered Passive Pores.” *Current Opinion in Structural Biology* 6 (4): 485–90.

Schwartzkopff, Benjamin, Harald W. Platta, Sohel Hasan, Wolfgang Girzalsky, and Ralf Erdmann. 2015. “Cysteine-Specific Ubiquitination Protects the Peroxisomal Import Receptor Pex5p against Proteasomal Degradation.” *Bioscience Reports* 35 (3). https://doi.org/10.1042/BSR20150103.

Smith, Martin T. J., and John L. Rubinstein. 2014. “Structural Biology. Beyond Blob-Ology.” *Science* 345 (6197): 617–19.

Stanley, Will A., Fabian V. Filipp, Petri Kursula, Nicole Schüller, Ralf Erdmann, Wolfgang Schliebs, Michael Sattler, and Matthias Wilmanns. 2006. “Recognition of a Functional Peroxisome Type 1 Target by the Dynamic Import Receptor pex5p.” *Molecular Cell* 24 (5): 653–63.

Subramani, Suresh. 2002. “Faculty Opinions Recommendation of Saccharomyces Cerevisiae Acyl-CoA Oxidase Follows a Novel, Non-PTS1, Import Pathway into Peroxisomes That Is Dependent on Pex5p.” *Faculty Opinions – Post-Publication Peer Review of the Biomedical Literature*. https://doi.org/10.3410/f.1005833.70156.

Tang, Guang, Liwei Peng, Philip R. Baldwin, Deepinder S. Mann, Wen Jiang, Ian Rees, and Steven J. Ludtke. 2007. “EMAN2: An Extensible Image Processing Suite for Electron Microscopy.” *Journal of Structural Biology* 157 (1): 38–46.

Tel-or, Elisha, Margaret E. Huflejt, and Lester Packer. 1986. “Hydroperoxide Metabolism in Cyanobacteria.” *Archives of Biochemistry and Biophysics*. https://doi.org/10.1016/0003-9861(86)90485-6.

Terlecky, S. R., W. M. Nuttley, D. McCollum, E. Sock, and S. Subramani. 1995. “The Pichia Pastoris Peroxisomal Protein PAS8p Is the Receptor for the C-Terminal Tripeptide Peroxisomal Targeting Signal.” *The EMBO Journal* 14 (15): 3627–34.

Thon, F. 1971. “Phase Contrast Electron Microscopy.” *Electron Microscopy in Material Science*. https://doi.org/10.1016/b978-0-12-780584-9.50021-0.

Vitturi, A., and F. Zardi. 1987. “Modified Glauber Model for the Description of Elastic Scattering between Heavy Ions.” *Physical Review C: Nuclear Physics* 36 (4): 1404–7.

Wagner, Thorsten, Felipe Merino, Markus Stabrin, Toshio Moriya, Claudia Antoni, Amir Apelbaum, Philine Hagel, et al. 2019. “SPHIRE-crYOLO Is a Fast and Accurate Fully Automated Particle Picker for Cryo-EM.” *Communications Biology* 2 (June): 218.

———. n.d. “SPHIRE-crYOLO: A Fast and Accurate Fully Automated Particle Picker for Cryo-EM.” https://doi.org/10.1101/356584.

Wagner, Thorsten, and Stefan Raunser. 2020. “The Evolution of SPHIRE-crYOLO Particle Picking and Its Application in Automated Cryo-EM Processing Workflows.” *Communications Biology* 3 (1): 61.

Walton, P. A., P. E. Hill, and S. Subramani. 1995. “Import of Stably Folded Proteins into Peroxisomes.” *Molecular Biology of the Cell*. https://doi.org/10.1091/mbc.6.6.675.

Wanders, R. J. A., S. Ferdinandusse, G. A. Jansen, E. G. van Grusven, H. R. Waterham, C. W. T. van Roermund, and P. Vreken. 2001. “Peroxisomal Fatty Acid Alpha- and Beta-Oxidation in Humans: New Insights into Enzymology, Substrate Specificities, Metabolite Transport and Peroxisomal Diseases.” *Biochemical Society Transactions*. https://doi.org/10.1042/bst029a002a.

Wanders, R. J. A., and H. R. Waterham. 2005. “Peroxisomal Disorders I: Biochemistry and Genetics of Peroxisome Biogenesis Disorders.” *Clinical Genetics* 67 (2): 107–33.

Wang, Jiao-Yu, Ling Li, Rong-Yao Chai, Hai-Ping Qiu, Zhen Zhang, Yan-Li Wang, Xiao-Hong Liu, Fu-Cheng Lin, and Guo-Chang Sun. 2019. “Pex13 and Pex14, the Key Components of the Peroxisomal Docking Complex, Are Required for Peroxisome Formation, Host Infection and Pathogenicity-Related Morphogenesis in Magnaporthe Oryzae.” *Virulence* 10 (1): 292–314.

Watanabe, Yuichi, Kosuke Kawaguchi, Naoki Okuyama, Yuri Sugawara, Takayuki Obita, Mineyuki Mizuguchi, Masashi Morita, and Tsuneo Imanaka. 2016. “Characterization of the Interaction between Trypanosoma Brucei Pex5p and Its Receptor Pex14p.” *FEBS Letters* 590 (2): 242–50.

Watanabe, Yuichi, Kosuke Kawaguchi, Syuken Saito, Takayoshi Okabe, Kiyoaki Yonesu, Shinichiro Egashira, Masafumi Kameya, Masashi Morita, Yoshinori Kashiwayama, and Tsuneo Imanaka. 2016. “An HTRF Based High-Throughput Screening for Discovering Chemical Compounds That Inhibit the Interaction between Trypanosoma Brucei Pex5p and Pex14p.” *Biochemistry and Biophysics Reports*. https://doi.org/10.1016/j.bbrep.2016.05.004.

Weber, Irene. 2016. “Faculty of 1000 Evaluation for Breaking Cryo-EM Resolution Barriers to Facilitate Drug Discovery.” *F1000 - Post-Publication Peer Review of the Biomedical Literature*. https://doi.org/10.3410/f.726387219.793522847.

Will, G. K., M. Soukupova, X. Hong, K. S. Erdmann, J. A. Kiel, G. Dodt, W. H. Kunau, and R. Erdmann. 1999. “Identification and Characterization of the Human Orthologue of Yeast Pex14p.” *Molecular and Cellular Biology* 19 (3): 2265–77.

Yang, X., P. E. Purdue, and P. B. Lazarow. 2001. “Eci1p Uses a PTS1 to Enter Peroxisomes: Either Its Own or that of a Partner, Dci1p.” *European Journal of Cell Biology* 80 (2): 126–38.

Yang, Zhengfan, Jia Fang, Johnathan Chittuluru, Francisco J. Asturias, and Pawel A. Penczek. 2012. “Iterative Stable Alignment and Clustering of 2D Transmission Electron Microscope Images.” *Structure* 20 (2): 237–47.

Yano, Taisuke, Masahide Oku, Natsuko Akeyama, Akinori Itoyama, Hiroya Yurimoto, Shusuke Kuge, Yukio Fujiki, and Yasuyoshi Sakai. 2010. “A Novel Fluorescent Sensor Protein for Visualization of Redox States in the Cytoplasm and in Peroxisomes.” *Molecular and Cellular Biology* 30 (15): 3758–66.

Zheng, Shawn Q., Eugene Palovcak, Jean-Paul Armache, Kliment A. Verba, Yifan Cheng, and David A. Agard. 2017. “MotionCor2: Anisotropic Correction of Beam-Induced Motion for Improved Cryo-Electron Microscopy.” *Nature Methods* 14 (4): 331–32.

Zhou, Huan-Xiang, and Timothy A. Cross. 2013. “Influences of Membrane Mimetic Environments on Membrane Protein Structures.” *Annual Review of Biophysics* 42 (March): 361–92.

Zhu, Hongtao, and Ping Zhu. 2015. “No Longer ‘blob-Ology’: Cryo-EM Is Getting into Molecular Details.” *Science China Life Sciences*. https://doi.org/10.1007/s11427-015-4942-0.

Zhu, Jun, Pawel A. Penczek, Rasmus Schröder, and Joachim Frank. 1997. “Three-Dimensional Reconstruction with Contrast Transfer Function Correction from Energy-Filtered Cryoelectron Micrographs: Procedure and Application to the 70SEscherichia coliRibosome.” *Journal of Structural Biology*. https://doi.org/10.1006/jsbi.1997.3845.

Zolman, Bethany K., Michelle Nyberg, and Bonnie Bartel. 2007. “IBR3, a Novel Peroxisomal Acyl-CoA Dehydrogenase-like Protein Required for Indole-3-Butyric Acid Response.” *Plant Molecular Biology* 64 (1-2): 59–72.

Zou, Xiaodong, Sven Hovmöller, and Peter Oleynikov. 2011. “Phase Contrast, Contrast Transfer Function (CTF) and High-resolution Electron Microscopy (HRTEM).” *Electron CrystallographyElectron Microscopy and Electron Diffraction*. https://doi.org/10.1093/acprof:oso/9780199580200.003.0006.